

AN ANALYSIS OF SECOND PHASE PARTICLES
IN ZIRCALOY 2

by

PIERRE LEON JACQUES CHEMELLE

Ingenieur de l' Ecole Centrale
des Arts et Manufactures
(1979)

SUBMITTED IN PARTIAL FULFILLMENT
OF THE REQUIREMENTS FOR THE
DEGREE OF

MASTER OF SCIENCE

at the

© MASSACHUSETTS INSTITUTE OF TECHNOLOGY

September 1980

Massachusetts Institute of Technology

Signature of Author _____

Department of Materials Science and Engineering

August 8, 1980

Certified by _____

John B. Vander Sande
Thesis Supervisor

Regis M.N. Pelloux
Thesis Supervisor

Accepted by _____

Regis M.N. Pelloux
Chairman, Departmental Graduate Committee

ARCHIVES
MASSACHUSETTS INSTITUTE
OF TECHNOLOGY

SEP 26 1980

LIBRARIES

AN ANALYSIS OF SECOND PHASE PARTICLES IN ZIRCALOY 2

by

PIERRE LEON JACQUES CHEMELLE

Submitted to the department of Materials Science and Engineering on 8 August 1980 in partial fulfillment of the requirements for the degree of Master of Science.

ABSTRACT

The different second phase particles present in zircaloy 2 in the annealed and in the cold worked, stress relieved conditions were analyzed by transmission electron microscopy (TEM) and by scanning transmission electron microscopy (STEM) of thin foils. The crystallographic structure of each phase was determined by selected area electron diffraction with the TEM and the chemical composition was obtained by energy dispersive X-Ray microanalysis with the STEM.

In zircaloy 2, two intermetallic phases are present as particles of 0.1 to 1 μm diameter uniformly distributed within an α zirconium matrix which contains tin in solid solution. One of the intermetallic phases has a hexagonal structure similar to ZrCr_2 ($a_0 = 5.1 \text{ \AA}$, $c_0 = 8.3 \text{ \AA}$) and a composition close to $\text{ZrCr}_{1.1}\text{Fe}_{0.9}$. This phase is often present as angular particles with twins or stacking faults on (0001) planes. The second intermetallic phase is a nickel-iron-zirconium compound of composition $\text{Zr}_2\text{Ni}_{0.4}\text{Fe}_{0.6}$ with the tetragonal structure of Zr_2Ni ($a_0 = 6.5 \text{ \AA}$, $c_0 = 5.3 \text{ \AA}$). In annealed zircaloy 2 individual particles were observed as well as heterogeneous clusters of particles. In addition to these phases, inclusions of 1 μm were identified as Zr_3Si . Scanning electron microscopy of chemically polished surfaces showed only the chromium rich phase as the nickel rich phase was dissolved by the chemical etching.

Thesis Supervisors: Regis M.N. Pelloux

Title: Professor of Materials Engineering

John B. Vander Sande

Title: Associate Professor of Materials Science

TABLE OF CONTENTS

<u>Chapter</u>		<u>Page</u>
	TITLE PAGE	1
	ABSTRACT	2
	TABLE OF CONTENTS	3
	LIST OF FIGURES	5
	LIST OF TABLES	8
	ACKNOWLEDGEMENTS	9
I	INTRODUCTION	10
	I.1. Historical background	10
	I.2. Zirconium alloys	10
	I.3. Development of zircalloys	11
II	REVIEW OF THE LITERATURE	13
	II.1. Introduction	13
	II.2. Phase diagrams	13
	II.3. Metallographic techniques	21
	II.4. Second phase analysis	22
III	MATERIALS AND TEST PROCEDURES	24
	III.1. Materials	24
	III.2. Test procedures	26
	III.2a. Thin foil preparation	26
	III.2b. Etching techniques and extraction replicas	28
	III.2c. X-Ray analysis	29

TABLE OF CONTENTS (Cont'd.)

<u>Chapter</u>		<u>Page</u>
IV.	RESULTS	
	IV.1. Optical observation and scanning electron microscopy	32
	IV.2. Transmission electron microscopy	35
	IV.2a. Introduction	35
	IV.2b. General observations	35
	IV.2c. Second phase particles	42
	IV.2d. Inclusions	55
	IV.3. Scanning transmission electron microscopy	56
V.	DISCUSSION	66
VI.	CONCLUSION	73
	APPENDIX A - Crystallography of hexagonal materials	75
	APPENDIX B - Electron diffraction of zircaloy 2	82
	APPENDIX C - Structure of zirconium compounds	93
	APPENDIX D - X-Ray data obtained in the STEM	99
	APPENDIX E - Characteristics of the TEM Philips EM300	106
	REFERENCES	108

LIST OF FIGURES

<u>Figure</u>		<u>Page</u>
1	Phase diagram of the system zirconium-tin	15
2	Phase diagram of the system zirconium-iron	16
3	Phase diagram of the system zirconium-chromium	17
4	Phase diagram of the system zirconium-nickel	18
5	Phase diagram of the system zirconium-hydrogen	19
6	Phase diagram of the system zirconium-oxygen	19
7	Specimen preparation	27
8	Windows set for X-Ray analysis	30
9	Scanning electron micrograph of the chemically etched surface of annealed zircaloy 2	33
10	Typical SEM X-Ray spectrum of a chromium-iron rich particle	34
11	Illustration of the formation of dislocation segments during the hydride growth in the [10.0] direction	36
12	Illustration of the contrast associated with the hydrides	37
13	Transmission electron micrograph of annealed zircaloy 2	39
14	Transmission electron micrograph of cold worked, stress relieved zircaloy 2	40
15	Transmission electron micrograph of the dislocation structure in cold worked, stress relieved zircaloy 2	41
16	Different types of intermetallic particles in zircaloy 2	43
17	Transmission electron micrograph of a nickel-iron rich particle in annealed zircaloy 2	47
18	Transmission electron micrograph of a chromium-iron rich particle in annealed zircaloy 2	48

LIST OF FIGURES (Cont'd.)

<u>Figure</u>		<u>Page</u>
19	Transmission electron micrograph of chromium-iron rich particles in annealed zircaloy 2	49
20	Transmission electron micrograph of a cluster of intermetallic particles in annealed zircaloy 2	50
21	Transmission electron micrograph of intermetallic particles in cold worked, stress relieved zircaloy 2	51
22	Transmission electron micrograph of intermetallic particles close to an inclusion in annealed zircaloy 2	52
23	Transmission electron micrograph of a Zr_3Si inclusion in annealed zircaloy 2	53
24	Transmission electron micrograph of a Zr_3Si inclusion in cold worked, stress relieved zircaloy 2	54
25	Scanning transmission electron microscope (STEM) image of annealed zircaloy 2	57
26	Typical STEM X-Ray spectrum obtained from a nickel-iron rich particle	58
27	Statistical distribution of the nickel-iron rich particles analyzed in situ	59
28	Typical STEM X-Ray spectrum obtained from a chromium-iron rich particle	60
29	Statistical distribution of the chromium-iron rich particles analyzed in situ	61
30	Statistical distribution of the chromium-iron rich particles analyzed on extraction replicas	62
31	Typical STEM X-Ray spectrum of the matrix	63
32	Typical STEM X-Ray spectrum of an inclusion in annealed zircaloy 2	64
33	Electron diffraction pattern of intermetallic particles presenting structure reflections and structure factor influence	69
A1	Important planes and directions in the h.c.p. structure	76

LIST OF FIGURES (Cont'd.)

<u>Figure</u>		<u>Page</u>
A2	Stereographic projection and (x,y) coordinate net	79
A3	Definition of the (x,y) coordinates system	80
B1	Reciprocal lattice of the hexagonal close packed structure	83
B2	Twelve of the most densely populated reciprocal lattice planes for the h.c.p. structure	84
B3	Relation between electron diffraction patterns and (0001) stereographic projection	86
B4	General Kikuchi maps for c.p.h. crystals	87
B5	Kikuchi map for zircaloy 2 Part I	88
B6	Kikuchi map for zircaloy 2 Part II	89
B7	Kikuchi map for zircaloy 2 Part III	90
B8	Composite Kikuchi map for zircaloy 2 part I	91
B9	Composite Kikuchi map for zircaloy 2 part II	92
C1	Some observed electron diffraction patterns corresponding to tetragonal Zr_3Si	98
E1	Characteristic parameters of the TEM Philips EM300	107

LIST OF TABLES

<u>Table</u>		<u>Page</u>
1	Binary phase diagram data	20
2	Chemical composition of zircaloy 2	25
3	Characteristic parameters for X-Ray analysis	31
4	Basic crystallographic data of zirconium compounds	45
A1	Angles between (hkil) and (h'k'i'l') planes in hexagonal Zr.	77
A2	Computed parameters for the construction of the (x,y) net of coordinates	81
B1	Twelve of the most densely populated reciprocal lattice planes for Zr_{α} .	85
C1	Calculated interplanar spacing of the (hkil) planes for hexagonal Zr and $ZrCr_2$	94
C2	Twelve of the most densely populated reciprocal lattice planes for $ZrCr_2$	95
C3	Calculated interplanar spacing of the (hkl) planes for tetragonal Zr_2Ni	96
C4	Calculated interplanar spacing of the (hkl) planes for cubic $ZrCr_2$	97
C5	Calculated interplanar spacing of the (hkl) planes for tetragonal Zr_3Si	97
D1	Computed data for X-Ray analysis	100
	Part I	100
	Part II	101
	Part III	102
	Part IV	103
	Part V	104
	Part VI	105

ACKNOWLEDGEMENTS

I would sincerely like to thank Professor John B. Vander Sande and Professor Regis M.N. Pelloux for their support and technical guidance throughout my research. They were always open to technical discussion as well as personal advice.

I am grateful to a number of people of the Electron Microscopy research group and of the Fatigue research group for creating a friendly atmosphere and engaging in many informative discussions that made this work possible.

I also deeply appreciate the technical assistance and patience of Dr. A.J. Garratt-Reed on the STEM, of Leonard Studenfield on the SEM and of Jim Nakos on the TEM.

Finally I would like to thank Exxon Nuclear Company, Inc. for their partial funding of this research, and IRSID for making my studies at MIT possible.

I. INTRODUCTION

I.1. Historical background

Even though zirconium is more abundant in the earth's crust (0.03%) than lead, copper, nickel or zinc, it has been known only for the last two centuries. Discovered in 1789 by the German chemist Klaproth in a "jargon" of Ceylon, the element zirconium was not isolated in its metallic form until 1824 when Berzelius obtained an impure metal powder by reducing potassium fluoro-zirconate with metallic potassium. Hafnium, which is always associated with zirconium in the ore (about 2%), was not isolated until 1923 (Costes and Hevesy). In 1925 Van Arkel, Deboer and Fast prepared the pure metal by decomposition of the iodide. In 1944 W. J. Kroll developed the technique of reduction of the chloride with metallic magnesium which is still the only method of production.

Zirconium had no specific use until 1952. A very small neutron capture cross section (0.18 barn) (1) compared to steel (3.1 barn) as well as an exceptional corrosion resistance in water and steam under pressure led to the universal use of zirconium alloys as fuel cladding materials for nuclear reactors.

I.2. Zirconium alloys

Many additions have been studied in order to improve the properties of zirconium but very few have led to commercial alloys. The limitations are associated with the following complications:

- a. above a few percent of alloying element, complex brittle structures are often formed

b. alloying increases the neutron capture cross section.

Today the main alloys can be classified as:

Alloys having good corrosion properties in water or steam:

*zircaloy 2 1.5% Sn, 0.15% Fe, 0.1% Cr, 0.05% Ni

*zircaloy 4 1.5% Sn, 0.2% Fe, 0.1% Cr, less than
0.007% Ni

*zirconium 2.5% Nb

Alloys having good corrosion properties in CO₂:

*ATR 0.5% Cu, 0.5% Mo

*ZU1 1.8% Cu

*ZU2 2.5% Cu

For chemical applications (hydrochloric acid, nitric acid, organic acids) unalloyed zirconium is preferred.

The high reactivity of zirconium with oxygen, nitrogen and hydrogen led to its use in flash bulbs and getters, (Zirconium alloyed with aluminum, titanium, carbon or nickel).

For the last two decades research on zirconium alloys has greatly increased and their applications range keeps broadening. The use of zirconium as an alloying element in aluminum, magnesium, copper, titanium or molybdenum alloys, super alloys and even steels (2) is an important part of the zirconium market.

I.3. Development of zircaloys

An early study (3) of the corrosion of Van Arkel zirconium in water clearly demonstrated a variability of the quality of the material. The influence of the impurity content and mainly the deleterious effects of

nitrogen, carbon and aluminum were recognized at that time. The "elimination of the disturbed surface layer" (3) by etching in a nitric acid-hydrofluoric acid solution increases the corrosion resistance once the etchant has been well removed.

The results of corrosion tests of sponge zirconium alloyed with tin showed that an optimum addition dependant on the impurity content of the alloy--chiefly nitrogen--could be achieved. For example, an optimum of 2.5% tin was determined for 700 ppm of nitrogen. During corrosion in water, a black oxide is formed in the first stage, followed by flaking and white corrosion products which are usually characteristic of the rapid second stage. The black oxide is more adherent and flaking is markedly retarded when zirconium is alloyed with tin.

The 2.5% tin alloy, called zircaloy 1, showed variations of properties from ingot to ingot and an accelerated corrosion rate for very long exposures to hot water. It is now obsolete. An alloy with small additions of iron, nickel and chromium was called zircaloy 2. It is today the main alloy used for the cladding of nuclear fuel in Boiling Water Reactors (BWR). Zircaloy 3, with a reduced tin content (0.25 to 0.5%) showed local white corrosion and was never produced commercially. Zircaloy 4, very similar to zircaloy 2, with iron replacing nickel, exhibits a lower hydrogen pick up than zircaloy 2 and is preferred in Pressurized Water Reactors (PWR) where the environment is slightly overpressured with hydrogen.

II. REVIEW OF THE LITERATURE

II.1. Introduction

The amount of research work done on zirconium during the last two decades is considerable. The volume of publications on zircalloys could easily fill up several rooms but a single drawer would contain the work done on the studies of zirconium microstructures and on the identification of the phases present. Most publications describe the processing of zircalloys, report on their mechanical properties, the preferred orientation (texture) and the effects of heat treatments, the influence of hydrides and the corrosion properties in various environments at different temperatures.

II.2. Phase diagrams

Phase diagrams of binary zirconium alloys have been studied since 1950. Data on nearly all possible systems are available (4 - 9). Many uncertainties regarding the identified phases still remain today even in the Zr-Sn, Zr-O, Zr-H or Zr-Fe diagrams.

Zirconium has a hexagonal structure ($a=3.232 \text{ \AA}$, $c=5.147 \text{ \AA}$) (10) at room temperature (phase α) and it undergoes an allotropic transformation at 865°C . The high temperature structure is body centered cubic (bcc) (phase β). The allotropic transformation $\beta \rightarrow \alpha$ is of martensitic or bainitic type depending on the cooling rate. Alloying drastically modifies this situation. The binary diagrams present on the zirconium rich side a two-phase domain ($\alpha+\beta$). Elements such as oxygen and tin can be considered as α stabilizers (raise the $\beta \rightarrow \alpha$ temperature) and elements such as nickel, iron or chromium as β stabilizers.

The binary diagrams Zr-Sn, Zr-Fe, Zr-Cr, Zr-Ni, Zr-H, Zr-O from Kubaschewski, Von Goldbeck (5) are given in figures 1 to 6. The zirconium-tin diagram (Figure 1) shows that in a 1.5% Sn alloy, tin is in solid solution in the α phase above 500°C and precipitated as Zr_4Sn with a β -W structure (11) below 500°C. The zirconium-iron diagram (Figure 2) indicates a very low solubility of iron in the α phase (0.04 at% at 795°C) and the compound Zr_4Fe precipitates below 795°C for a 0.1-0.3 wt% Fe alloy. Iron is soluble in the β phase up to several percent in weight. The phase diagram zirconium-chromium (Figure 3) is characterized by one compound $ZrCr_2$ and two eutectics. The maximum solubility in α Zr is 0.49 at% (10.3 wt%) and in β Zr it is 7.5 at%. Precipitation of $ZrCr_2$ is expected below 835°C.

The zirconium nickel diagram shows many intermetallic compounds. The existence of Zr_5Ni (12) has not been confirmed. The solubility of nickel in zirconium has not been determined accurately; it is believed to be very small (Hansen and Anderko (7)). Below 845°C precipitation of Zr_2Ni has been indicated by various authors (5). As oxygen and hydrogen effects have been observed in the present study, the binary phase diagrams Zr-H and Zr-O are included here (Figures 5 and 6). Characteristic data for the binary systems are compiled in Table 1.

Ternary phase diagrams such as Zr-Cr-Sn and Zr-Fe-Sn have also been investigated (13, 14). Tanner (14) indicates the presence of a ternary phase θ between 7 and 8 wt% iron and about 24.5 wt% tin. Sections of the ternary system Zr-Fe-Sn in the zirconium rich corner are given at 700°C, 800°C, 900°C, 1000°C and 1100°C. At 700°C, the

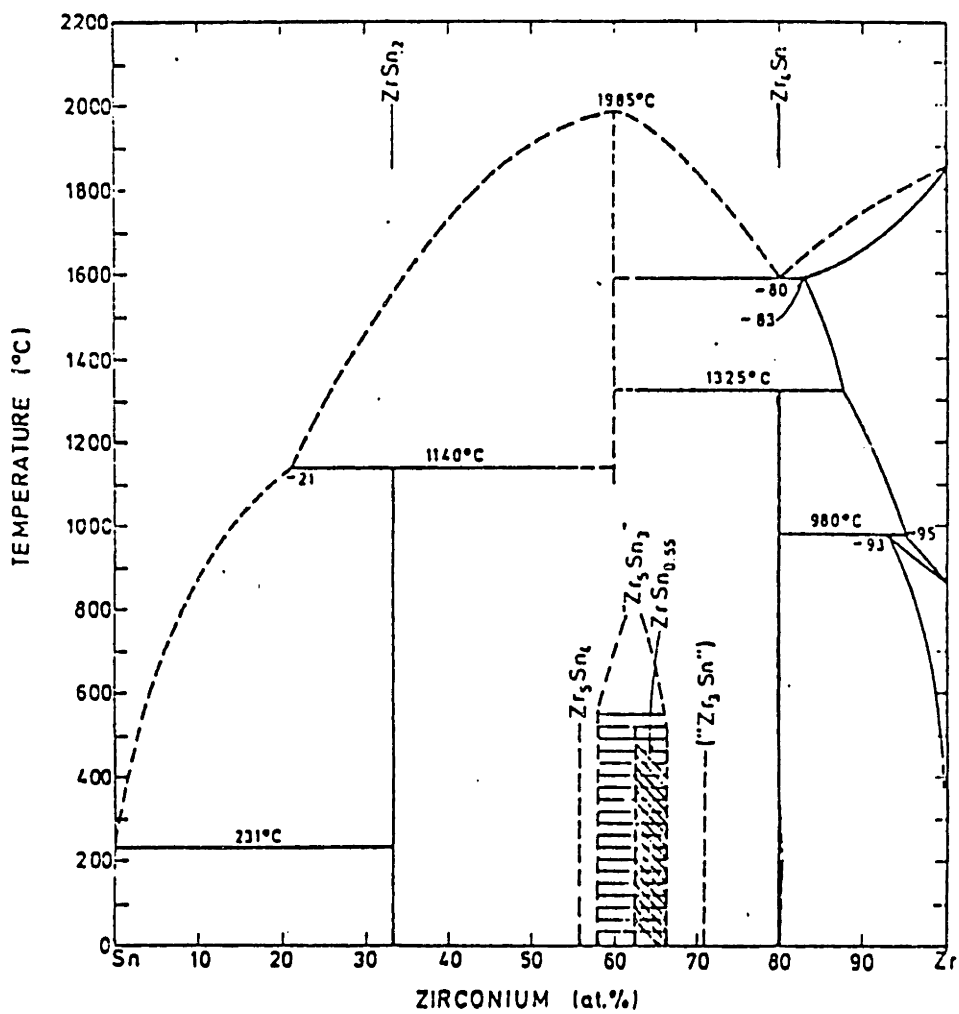


Figure 1: Phase diagram of the system zirconium-tin

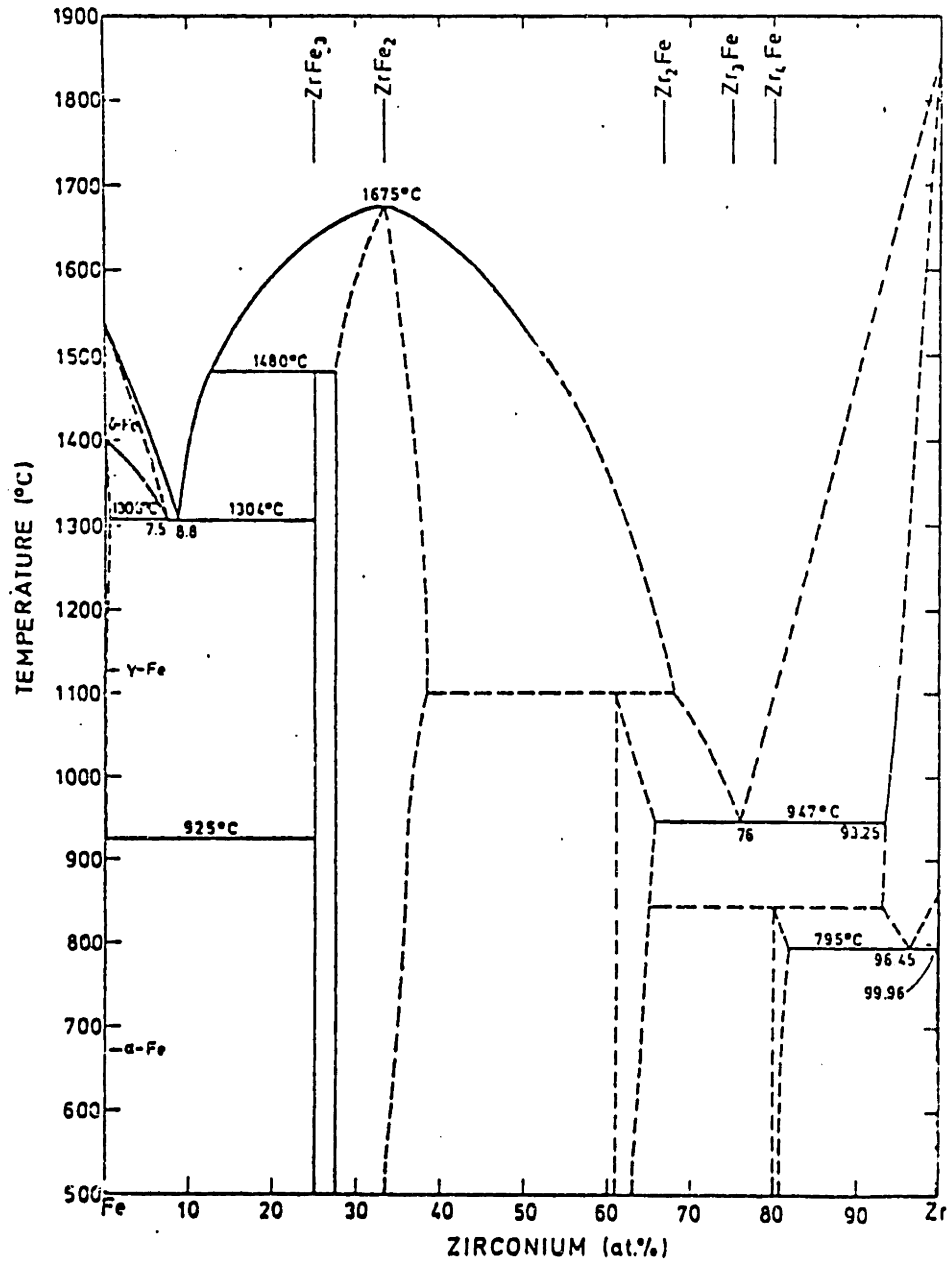


Figure 2: Phase diagram of the system zirconium-iron

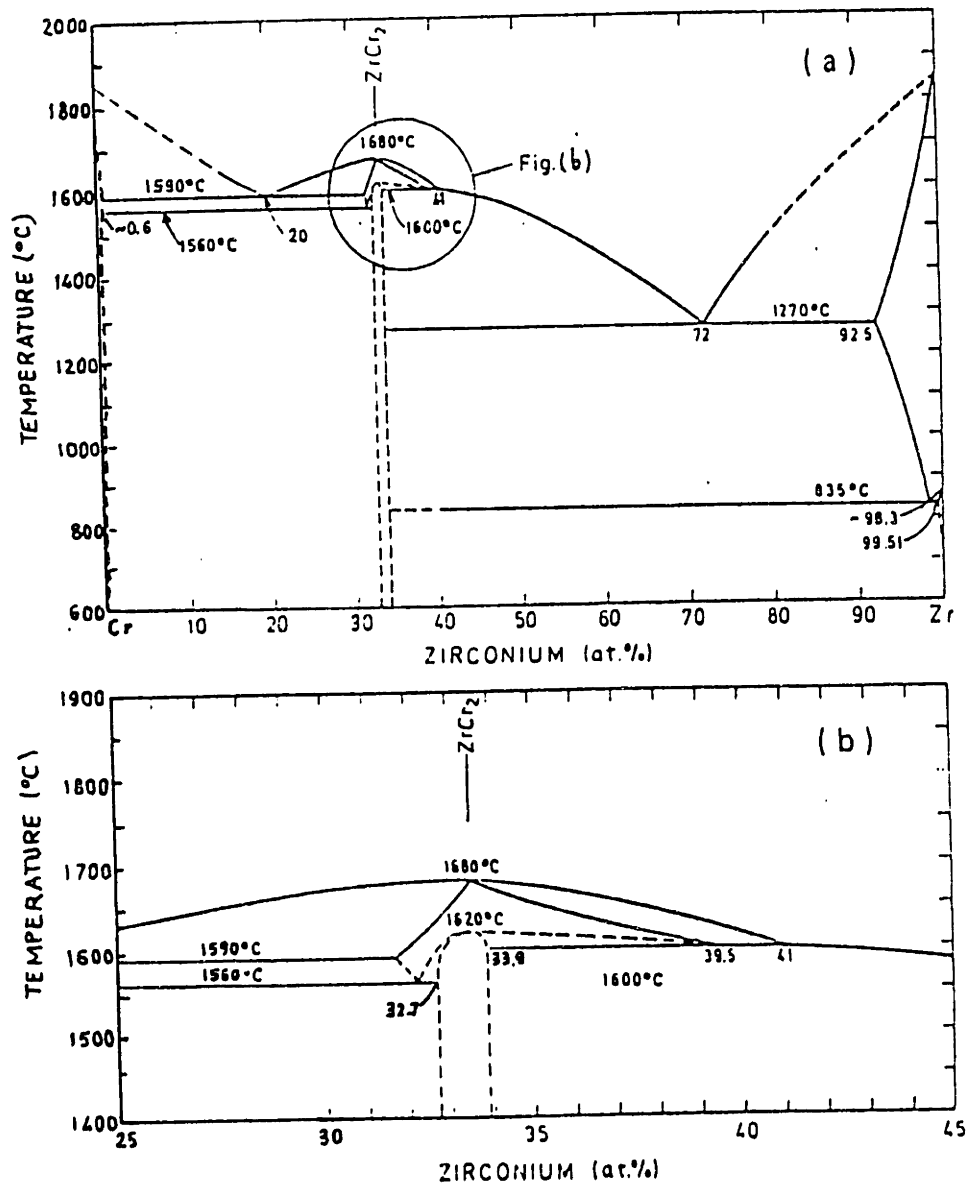


Figure 3: Phase diagram of the system zirconium-chromium

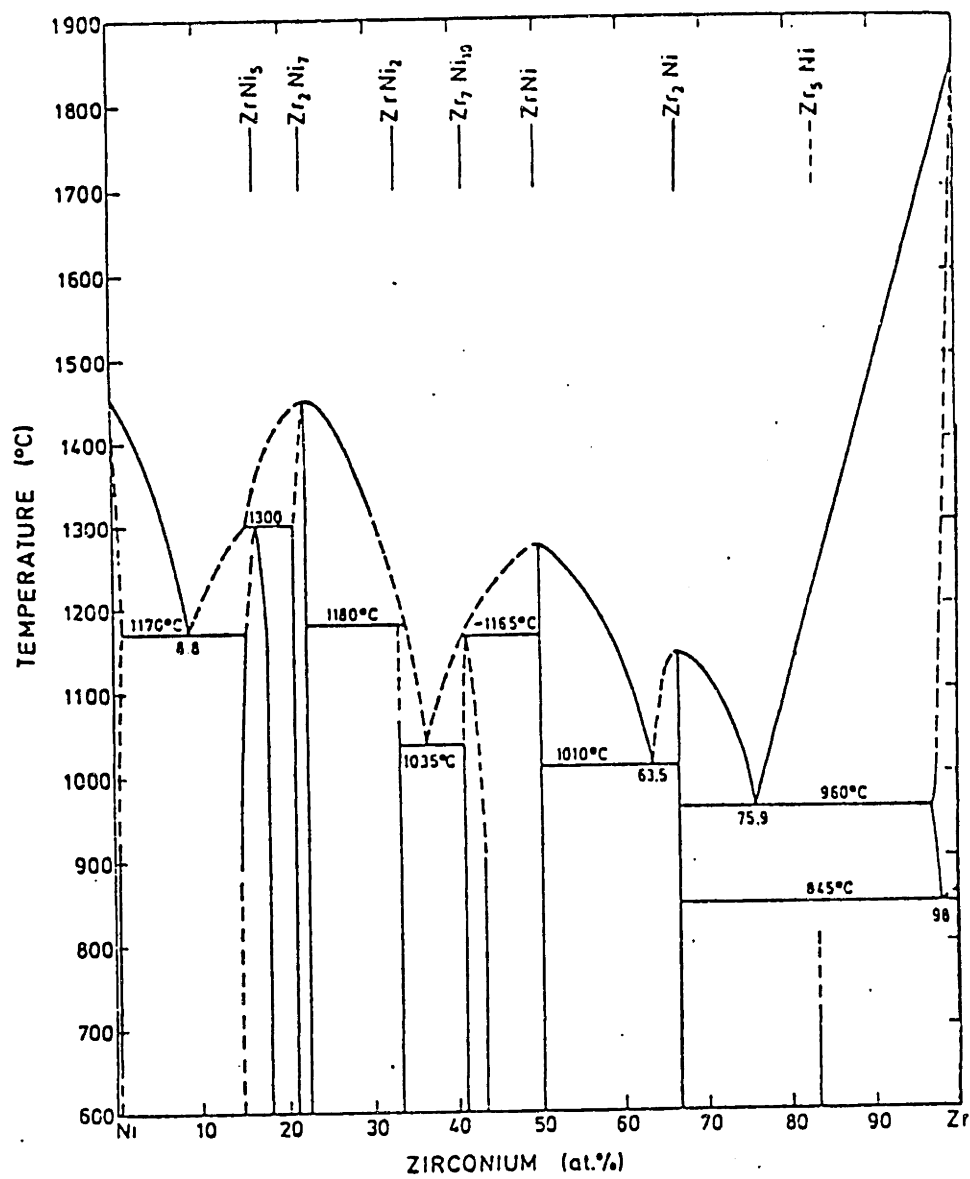


Figure 4: Phase diagram of the system zirconium-nickel

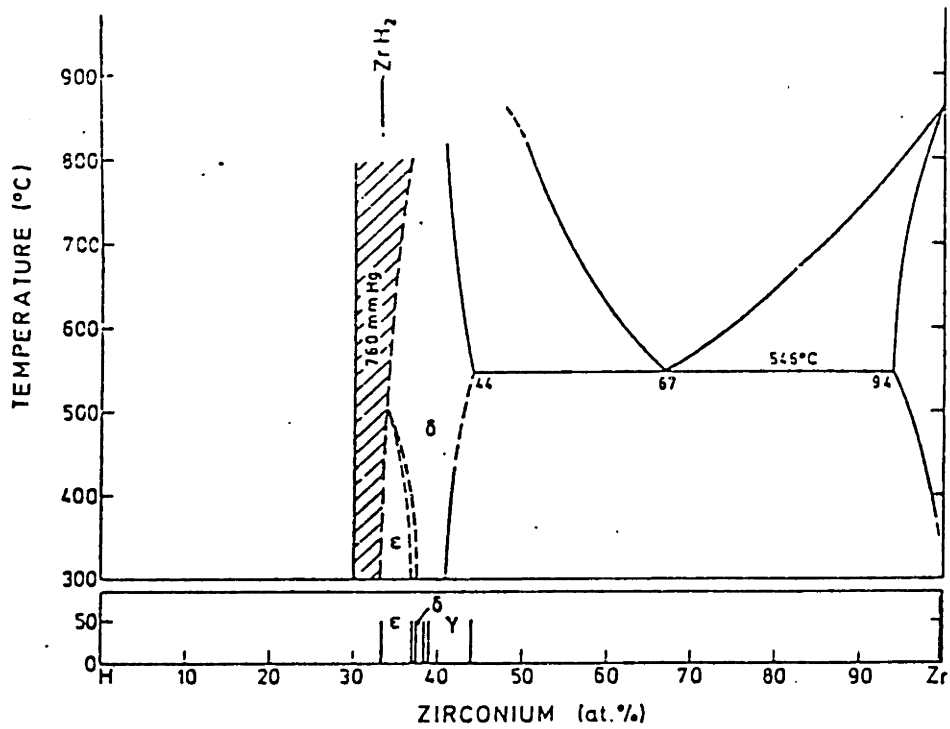


Figure 5: Phase diagram of the system zirconium-hydrogen

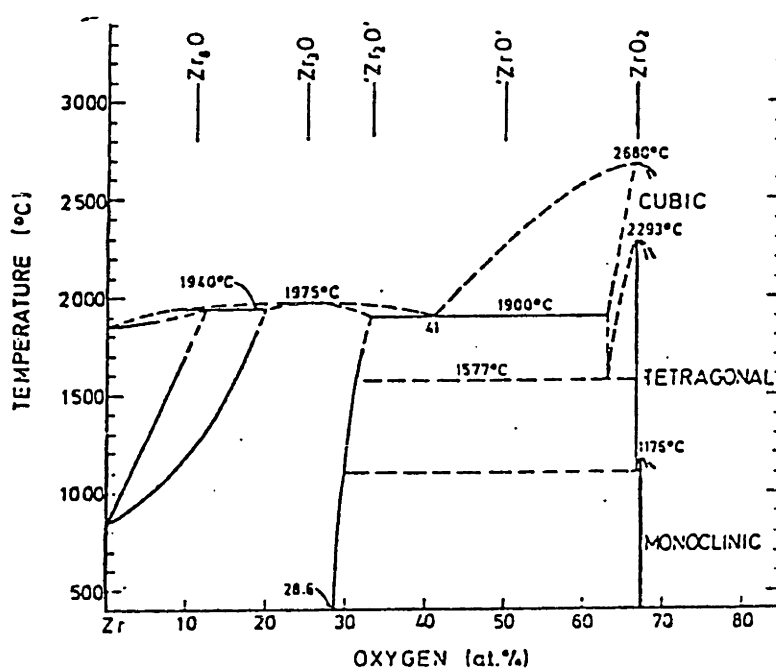


Figure 6: Phase diagram of the system zirconium-oxygen

Table 1 : Binary phase diagram data (6).

Alloying element	Maximum Solubility in β Zr wt%	Eutectic or Peritectic Composition wt%	Temperature $^{\circ}\text{C}$	Compound or phase in equilibrium
tin	21.0	23.5	1590	Zr_3Sn_2
iron	5.5	16.0	931	ZrFe_2
chromium	4.5	18.0	1300	ZrCr_2
nickel	1.9	17.0	961	Zr_2Ni
oxygen	2.0	?	1940	$\text{Zr}_\alpha\text{-O (3.75\%)}$
	Maximum solubility in α Zr wt%			
tin	9.0	5.0	980	Zr_4Sn
iron	0.02	2.5	780	ZrFe_2
chromium	very small	1.0	835	ZrCr_2
nickel	very small	1.3	808	Zr_2Ni
oxygen	3.75		1940	Zr_β

θ phase could be present even for very low iron (0.01 wt%) and tin (0.05 wt%) contents. Zr_4Fe was not observed even in the binary Zr-Fe system.

II.3. Metallographic techniques

Different techniques have been used to prepare thin foils of zircaloy for transmission electron microscopy. There are two problems: (a) the formation of hydrides and (b) the preferential etching of inter-metallic particles.

J.B. Vander Sande and Bement have used successfully a chemical rough thinning followed by a final ion milling for zircaloy 4 (15). D.O. Northwood and R.W. Gilbert (16) describe a suitable preparation technique for low hydride production. Instead of using a window technique, as Bedford (17), a jet technique is employed. The thinning is done in two steps: prethinning by chemical polishing in 45% HNO_3 , 45% H_2O , 5% HF; final thinning by electropolishing in a 4/1 ethyl alcohol: perchloric acid at 240°K under 20V, washing in ethyl alcohol. P. Rao, J.L. Walker and E.F. Koch (18) used a two step electropolishing technique:

first step: 50 ml perchloric acid
 175 ml acetic acid
 100 ml ethylene glycol at 0°C

second step: 190 ml perchloric acid
 760 ml acetic acid at -54°C

Bailey (19) used a single step electropolishing technique. The electrolyte was a 10% perchloric acid 90% glacial acetic acid vigorously stirred and kept cool. The specimen were polished under 20V and washed in distilled water.

II.4. Second phase analysis

The presence of second phase particles in zircaloy has been known for a long time but their chemical composition as well as their crystallographic structure is still uncertain.

Ostberg has determined the TTT curves for zircaloy 2 (20) and has studied the variation of microstructure with heat treatment (21). The transformation study revealed two "noses" on the TTT curve, one at high temperature (about 870°C) for α formation, and one at lower temperature (about 650°C) for precipitation of X, a compound which was later found by Ostberg (22) to contain 5-6 wt% Fe, 0 to 2 wt% Cr, 4 to 9 wt% Ni and 4-5 wt% Sn. P. Rao (18) studied the intermetallic particles in zircaloy 2 and zircaloy 4. The crystallographic structure was determined by selected area electron diffraction and computer simulation. The chemical composition was examined by microprobe analysis on aged specimens. In zircaloy 2, two types of particles are present. One is a chromium-iron-zirconium compound of structure close to $ZrCr_2$ (hexagonal structure $a_o = 5.079 \text{ \AA}$ $c_o = 8.279 \text{ \AA}$). The other type of particle is a nickel-iron-zirconium compound of structure close to Zr_2Ni (tetragonal structure $a_o = 6.499 \text{ \AA}$ $c_o = 5.270 \text{ \AA}$). In zircaloy 4, the only particles present were those of the $ZrCr_2$ type which is in agreement with the results of Vander Sande (15) who gives a $Zr_xFe_5Cr_2$ chemical composition based on STEM data. Vitikainen (23) found a $ZrCr_2$ type of particles in a zirconium 0.5 wt% niobium, 0.5 wt% chromium alloy called Scanuk 4 but with a f.c.c. structure ($a_o = 7.195 \text{ \AA}$). The two varieties of $ZrCr_2$ have been described by Rostoker (24). According to Rostoker and Pearson (25) the f.c.c. variety is of type $MgCu_2$ with $a_o = 7.195 \text{ \AA}$ and stable at high temperature

while the hexagonal variety is of MgZn_2 type and stable at low temperature. In Zircaloy 2 Vitikainen (23) found two types of particles (precipitates of type A and B). The particles of type A were round (average diameter 0.3-0.6 μm) and of body centered tetragonal structure ($a_0 = b_0 = 6.5 \text{ \AA}$, $c_0 = 5.5 \text{ \AA}$). Some diffraction spots were missing in particular electron diffraction patterns. The X-Ray analysis with an energy dispersive system showed little nickel and iron. Many particles were partially etched. The particles of type B were smaller (0.1-0.3 μm) and more elongated. The structure as well as the composition was not determined. Vesaci (26) reported the alternate packing of hexagonal ZrCr_2 and face centered cubic ZrCr_2 within the precipitates in zircaloy 4.

III. MATERIALS AND TEST PROCEDURES

III.1. Materials

The zircaloy 2 used for this study was supplied by Teledyne Wah Chang, Albany, Oregon. Cold work stress, relieved tube as received and plates further annealed by Exxon were examined. The chemical composition of the tubing (external diameter 0.565 inch, wall thickness 0.05 inch) is given in Table 2. The level of impurities in zircaloy is kept very low. Many elements have a very low solubility in α zirconium and can precipitate, for example: phosphorus, silicon, carbon. Elements such as nitrogen, titanium, aluminum, silicon and carbon impair the corrosion properties. Elements as boron, uranium, hafnium and cadmium increase the cross capture section for thermal neutron, e.g., the cross capture section of cadmium is 2400 barns. The main impurities in zircaloy 2 are oxygen (1200 ppm), carbon (170 ppm), silicon (40-80 ppm), hafnium 150 ppm) nitrogen (40 ppm) and aluminum (40 ppm). The tube was in a cold worked, stress relieved condition (stress relieved for about 2 hours at 500°C). The plate was alternatively cold worked and annealed as follows:

cold rolled to 0.150 inch

vacuum annealed at 1350°F (730°C) for 2 hours

cold rolled to 0.105 inch

vacuum annealed at 1300°F (705°C) for 2 to 4 hours.

Table 2: Chemical composition of zircaloy 2

alloying element wt%	Specification	tubing	plate	
			Top	Bottom
Sn	1.20 - 1.70	1.50	1.52	1.49
Fe	0.07 - 0.20	0.139	0.14	0.15
Cr	0.05 - 0.15	0.105	0.11	0.10
Ni	0.03 - 0.08	0.053	0.05	0.05
O	0.09 - 0.14	0.131	0.123	0.121
Impurities ppm				
Al	< 75	35	46	41
B	< 0.5	0.2	< 0.25	< 0.25
C	< 270	180	170	160
Ca	< 30			
Cl	< 0.5	< 0.2	< 0.25	< 0.25
Cl	< 20	< 5		
Co	< 20	< 10	< 10	< 10
Cu	< 50	15	13	13
F	< 20			
H	< 25	12	7	11
Hf	< 100	49	63	62
Mg	< 20	< 10		
Mn	< 50	< 25	< 25	< 25
Mo	< 50	< 25		
N	< 80	47	39	38
Na	< 20			
Nb	< 100	< 50		
P	< 20			
Pb	< 130	< 50		
Si	< 120	44	87	84
Ta	< 200	< 100		
Ti	< 50	< 25	< 25	< 25
U _{total}	< 35	< 0.5	1.8	1.4
V	< 50	< 25	< 25	< 25
W	< 50	< 25	< 25	< 25
Zn	< 100			
Fe + Cr + Ni wt%	0.18 - 0.38	0.297	0.30	0.30

III.2. Test procedures

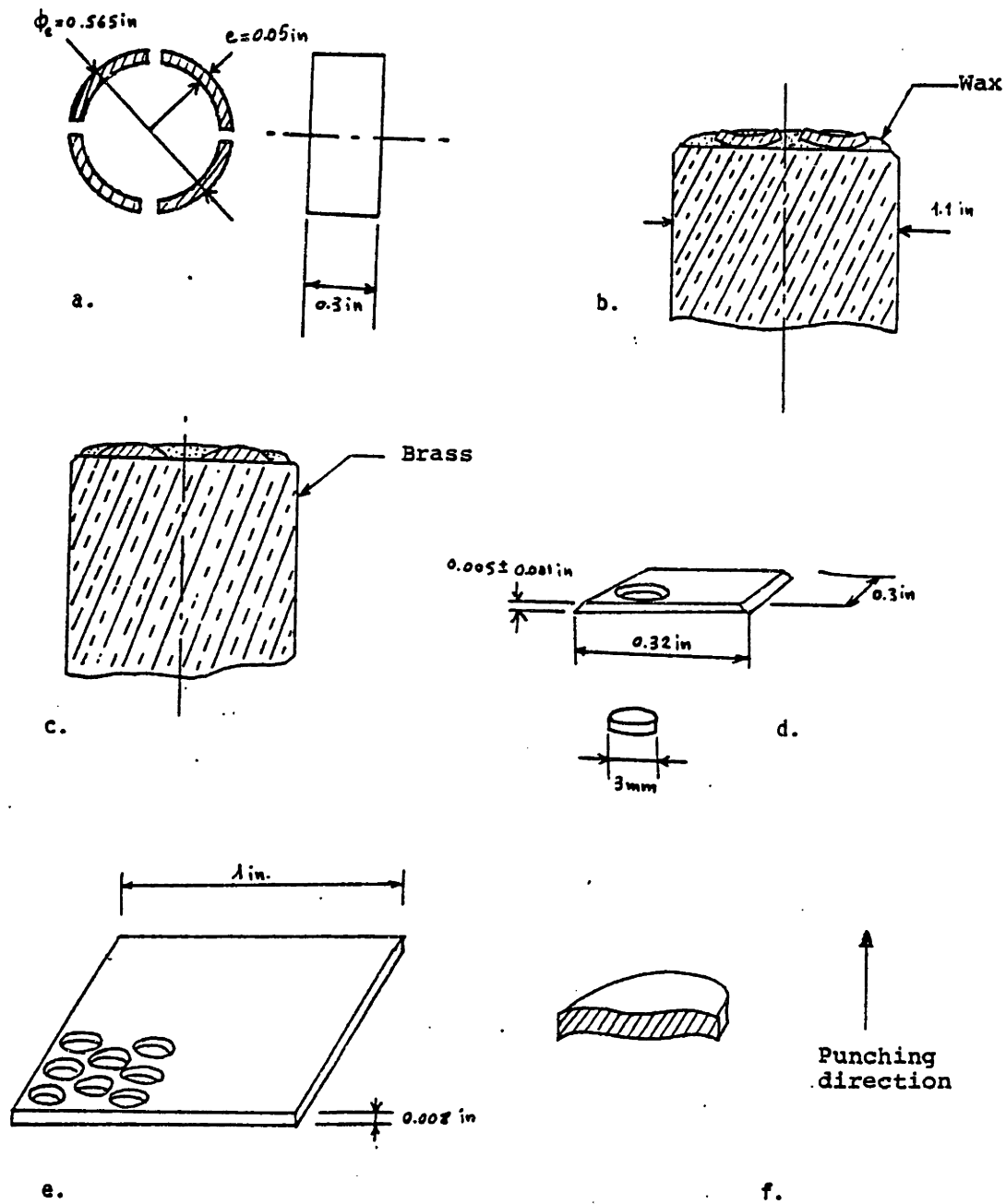
III.2a. Thin foil preparation

Mechanical grinding: Pieces of tube (Figure 7a) were cut to 0.3 inch by 0.3 inch and glued on a brass cylinder with wax. The wax "Rigidax W1 green" melts at 250°F (120°C) and is soluble in trichlorethylene (Figure 7b and c). They were ground with wet SiC paper No.120 -240-360 and 600 on both sides down to 5-6 mils (0.13 mm). The same procedure was followed for 1" x 1" pieces of sheet but the final thickness was 7-8 mils.

Punching: (Figure 7d-e). Three millimeters discs were punched out mechanically. Some of the thickest discs mainly from the sheet presented a small dimple (Figure 7f) due to plastic deformation.

Electropolishing: The jet technique was used with a Fishione apparatus. The electrolyte was 10-20% perchloric acid with 90-80% methanol (in volume) mixed at -30°C. The temperature was maintained below -30°C and down to -65°C by circulation of methanol cooled by a mixture of acetone and dry ice. A potential of 20 to 25 volts was applied for 3 to 10 minutes before the hole was detected. The polishing conditions were very sensitive to experimental parameters such as voltage, jet speed and current transients. The optimum polishing potential was 20 V for the annealed material and 22 V for the stress relieved material. If the potential is too high (26 V and above) or the temperature not low enough (-20°C) pitting occurs and the second phase particles disappear more quickly than the matrix. At very low temperatures (-60°C) a large number of hydrides were formed and -40°C seems to be a good compromise. Since passivation of the metal can occur as demonstrated by a sudden decrease of the intensity of the current (usually ranging

Figure 7: Specimen preparation



between 15 and 30 mA), the jet strength was set fairly high (position 4 or 5 on the Fishione) and may be a cause of some bending of the foil. An alternative is to raise, momentarily (a few seconds), the voltage and jet speed (7-8 position). The voltage was switched on before the specimen holder was lowered into the polishing bath and switched off when the polished specimen was in the rinse bath. Different solutions were used to rinse the specimen (e.g., distilled water, water with ammonia, methanol). The polished specimens exhibited very different hydride concentrations and it has not been established what exact conditions are required to eliminate the hydrides even if this has been achieved in some specimens. The best foils were obtained with a solution of only 10% perchloric acid. The temperature was about -35°C and the foil was rinsed very quickly after polishing, in water first and then in methanol. A third rinse in distilled water insured a low contamination by the beam during STEM X-Ray analysis.

III.2b. Etching techniques and Extraction replicas

For optical metallography and scanning electron microscopy, pieces of plate were ground with SiC wet paper No.120 and 600 and polished with alumina. The surface was then etched electrochemically under 20V at 0°C with a 10% perchloric acid 90% acetic acid.

Extraction replicas were made in one step. The mechanically polished surface was slightly etched at 0°C by a mixture of 5% hydrofluoric acid, 40% nitric acid, and 55% distilled water.

A film of Carbon (200-500 Å thick) was then deposited under vacuum. The matrix was dissolved using the same solution and the film removed

from the solution as fast as possible. Pieces of film were stretched flat with the usual alcohol-water technique and placed on copper grids. Some slightly etched plate samples were kept for SEM investigation.

III.2c. X-Ray analysis

In the SEM and in the STEM the X-Ray analysis was performed with energy dispersive systems. The spectra were recorded on magnetic discs. For data analysis and computation, windows of 270 eV width were set on the main peaks and at different energy levels for background analysis.

Figure 8 shows the repartition of the windows. Characteristic parameters were chosen to define the spectrums (Table 3). Subsequent computations were done manually and are tabulated in Appendix D.

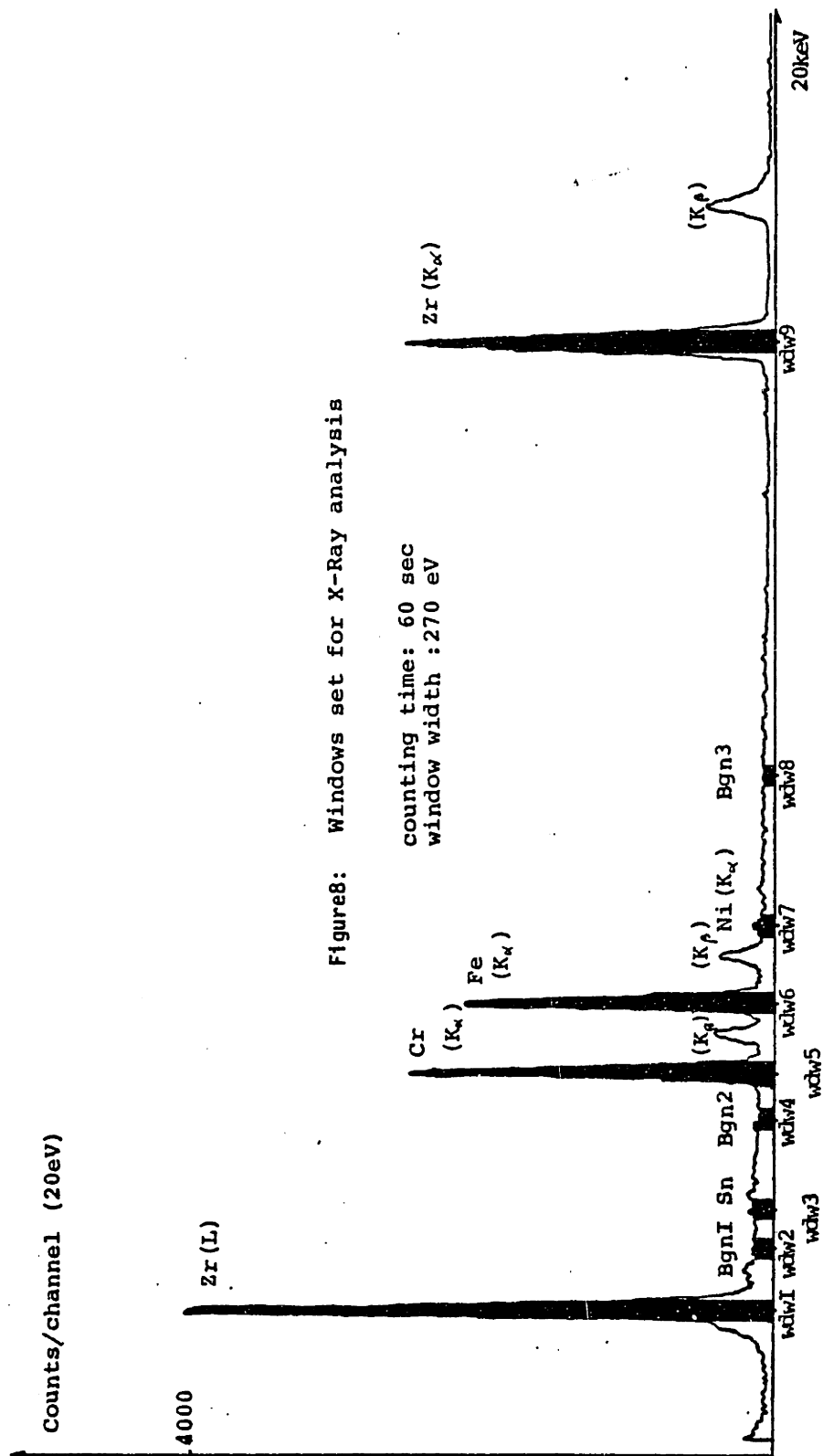


Figure8: Windows set for X-Ray analysis

Table 3 : Characteristic parameters for X-Ray analysis.

window	Region (keV)			description
	from	to	center	
wdw1	1.92	2.18	2.04	L-Ray of Zr
wdw2	2.78	3.04	2.9	Background 1
wdw3	3.34	3.60	3.47	Sn (L-Ray)
wdw4	4.62	4.88	4.75	Background 2
wdw5	5.26	5.52	5.39	Cr (K _α Ray)
wdw6	6.26	6.52	6.39	Fe (K _α Ray)
wdw7	7.34	7.60	7.46	Ni (K _α Ray)
wdw8	9.50	9.76	9.63	Background 3
wdw9	15.58	15.84	15.70	Zr (K _α Ray)

$$\text{BGN} = \frac{\text{wdw4} + \text{wdw8}}{2}$$

$$\text{Cr} = \frac{\text{wdw5} - \text{BGN}}{\text{wdw5} + \text{wdw6} + \text{wdw7} - 3 \cdot \text{BGN}}$$

$$\text{Fe} = \frac{\text{wdw6} - \text{BGN}}{\text{wdw5} + \text{wdw6} + \text{wdw7} - 3 \cdot \text{BGN}}$$

$$\text{Ni} = \frac{\text{wdw7} - \text{BGN}}{\text{wdw5} + \text{wdw6} + \text{wdw7} - 3 \cdot \text{BGN}}$$

$$\text{Fe/Bgn} = \frac{\text{wdw6}}{\text{BGN}} \quad \text{L/K} = \frac{\text{wdwI}}{\text{wdw9}}$$

$$\text{Zr} = \frac{\text{wdw9}}{\text{wdw5} + \text{wdw6} + \text{wdw7} + \text{wdw9} - 3 \cdot \text{BGN}}$$

$$\text{Sn/Bgn} = \frac{\text{wdw3}}{\text{wdw2}}$$

IV. RESULTS

IV.1. Optical observation and scanning electron microscopy

The same specimens were observed with a light microscope and with a SEM. The optical observation showed the grain size as well as phases and pits within the grains. The distinction between phases and pits could not be made by optical microscopy.

In the SEM, with a magnification greater than 1000X, particles could be observed. The energy dispersive X-Ray analyses provided their qualitative chemical analysis.

TEM 3 mm discs of cold worked and of annealed zircaloy 2 as well as pieces of electropolished plate were studied with the SEM (model AMR 1000). The surface was irregular and revealed the grain structure. Polishing pits some of which contained "particles", were observed within the grains. The energy dispersive X-Ray analysis revealed, within the pits, regions rich in chromium and iron and less frequently regions rich in nickel and iron. The chemically etched surface of the plate shows the grain size (Figure 9a). Dimples as well as particles can be observed with a magnification of 1000 X (Figure 9a). At higher magnification (Figure 9b), small particles stand out on the matrix surface. The X-Ray analysis, done in the SEM, showed that nearly all the particles present on the surface are chromium and iron rich and only very few contained nickel.

The X-Ray data obtained could not be treated quantitatively and the iron or chromium signal level was always low because the particles were small (0.2-0.3 μm) compared to the analyzed volume (1 μm^3). A typical spectrum of a particle analyzed with the SEM is presented in

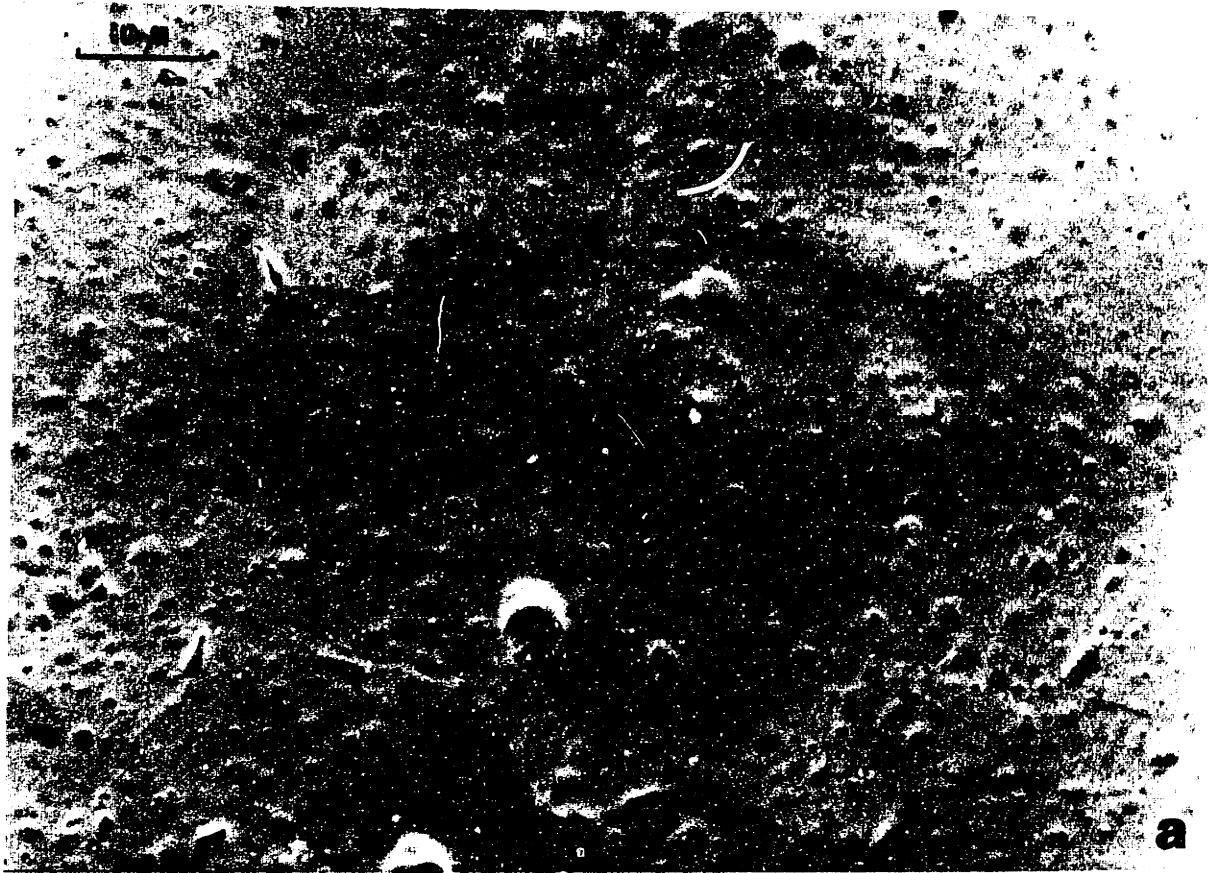


Figure 9 : Scanning electron micrograph of the chemically etched surface of annealed zircaloy 2.
a) Low magnification view.
b) Chromium rich particles.

10 μ

1 μ

Figure 1: Scanning electron micrograph of the surface of annealed aluminum. (a) low magnification view. (b) three μm view particle.

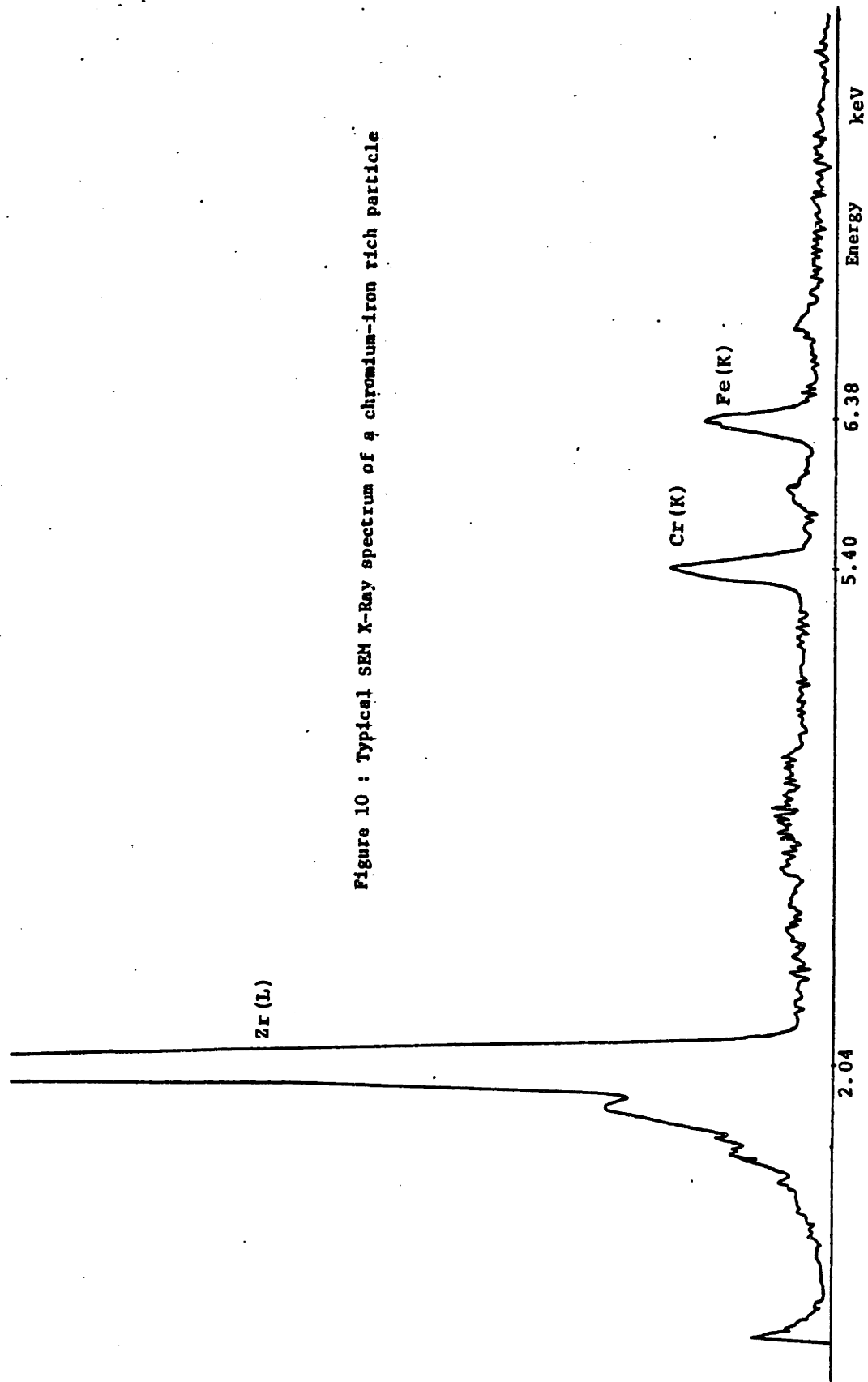


Figure 10 : Typical SEM X-Ray spectrum of a chromium-iron rich particle

Figure 10. All the particles visible in Figure 9b gave a spectrum of this type (chromium and iron).

IV.2. Transmission electron microscopy (TEM)

IV.2a. Introduction

The TEM work was performed on a Jeol model JEM7 microscope for low magnification (20000X) observation and on a Philips model EM300 for structure analysis by electron diffraction. Useful parameters of the instrument were determined by standard methods and are compiled in Appendix E.

IV.2b. General observation

Artifacts: Several artifacts due to foil preparation such as hydrides, slip traces, deformation twins and surface oxide layers were often observed. Bailey (19) studied the hydrides in zirconium thin foils. At low hydrogen concentrations (100-1000 ppm), the hydrides are of the γ tetragonal type. Small round hydrides (0.1μ) as well as larger platelets (larger than $1 \mu\text{m}$) are described. The latter are oriented in the matrix with a $(10\bar{1}0)$ habit plane. During their growth, the hydrides can punch out dislocation loops or lines (Figure 11). This $(10\bar{1}0)$ habit plane is not in contradiction with the $(10\bar{1}7)$ identification made by Westlake (27) for zircaloy 2 and zircaloy 4. The material and the hydrogenation technique used were different.

We observed in zircaloy 2 two types of hydrides. Small round shaped hydrides ($0.1-0.2\mu\text{m}$) were present on the surface of the foil. Their distribution was uniform within the grains. Often, Moiré patterns and alternate bending of dislocation lines near the surface of the foil were

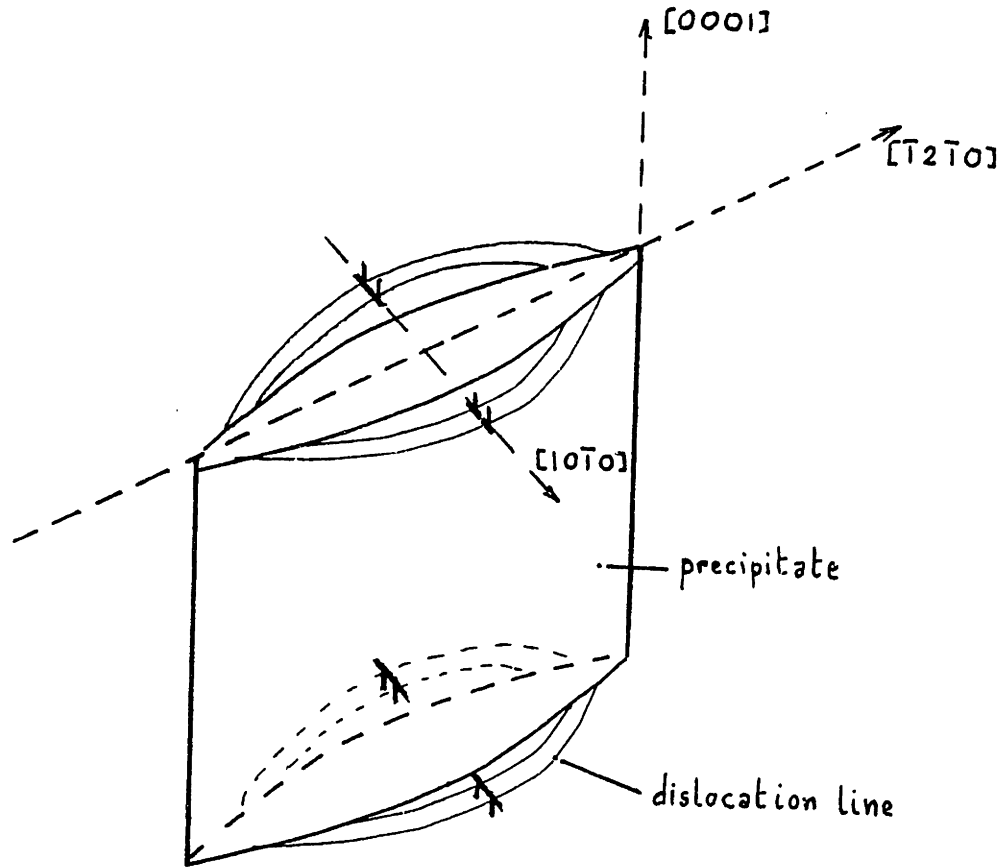


Figure 11 : Illustration of the formation of dislocation segments during the hydride growth in the $[10.0]$ direction.

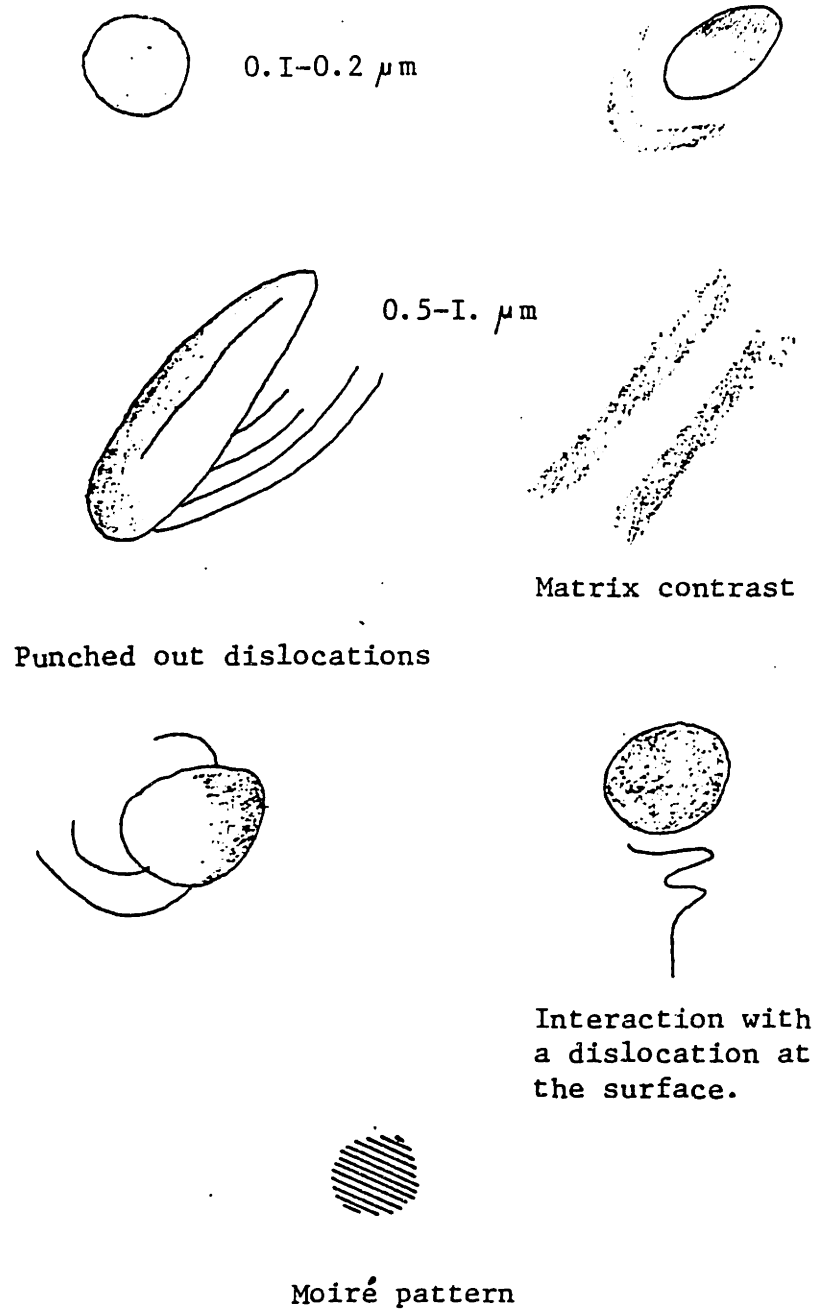


Figure 12: Illustration of the contrast associated with the hydrides.

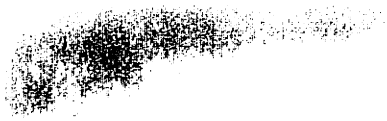
associated with these hydrides. Fewer but larger needle like hydrides (0.5-1 μm) oriented in three directions were found within the grains.

Large hydrides were often associated with dislocation loops and dislocation lines. The contrast of the hydrides, illustrated in Figure 12, is very dependant on the orientation of the foil. Slip traces due to foil bending and corresponding to prismatic slip were often observed for particular foil orientations. Some specimens exhibited many thin deformation twins (1 μm width) that were probably formed during specimen punching or foil mishandling. On all the specimens, oxidation was responsible for a graininess in the image (100-300 \AA of structure). As a result, the observation of features in the 100-300 \AA range would be very difficult in bright field. In diffraction, elongated additional spots or rings were due to the oxide. The oxide layer, which was oriented differently from grain to grain is probably ZrO_2 . Some evidence of the ordered Zr_3O solid solution was found in very thin parts of the specimen. The structure and the X-Ray diffraction analysis of Zr_3O has been described by J. De Buigne (28).

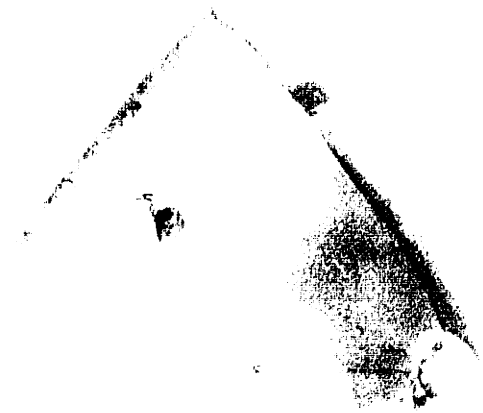
Structure of zircaloy 2: The typical structure of the annealed plate of zircaloy 2 is illustrated by Figure 13. The diameter of the observed grain varied from 4 to 20 μm . The grains were of a regular polygonal shape. Electron diffraction revealed a strong texture. Very few patterns corresponded to poles further than 70° from (0001) and the most common orientations were (0001), $(1\bar{2}13)$ and $(1\bar{1}02)$. Individual particles as well as clusters were observed within the grains and on grain boundaries. Slip traces, different types of hydrides with punched out dislocation lines, partially etched particles and oxidation



- Figure 13 : Transmission electron micrograph of annealed zircaloy 2.
h: hydride. p: particle.



10



11

12

13

14

15

16

17

18

19

20

21

22

23



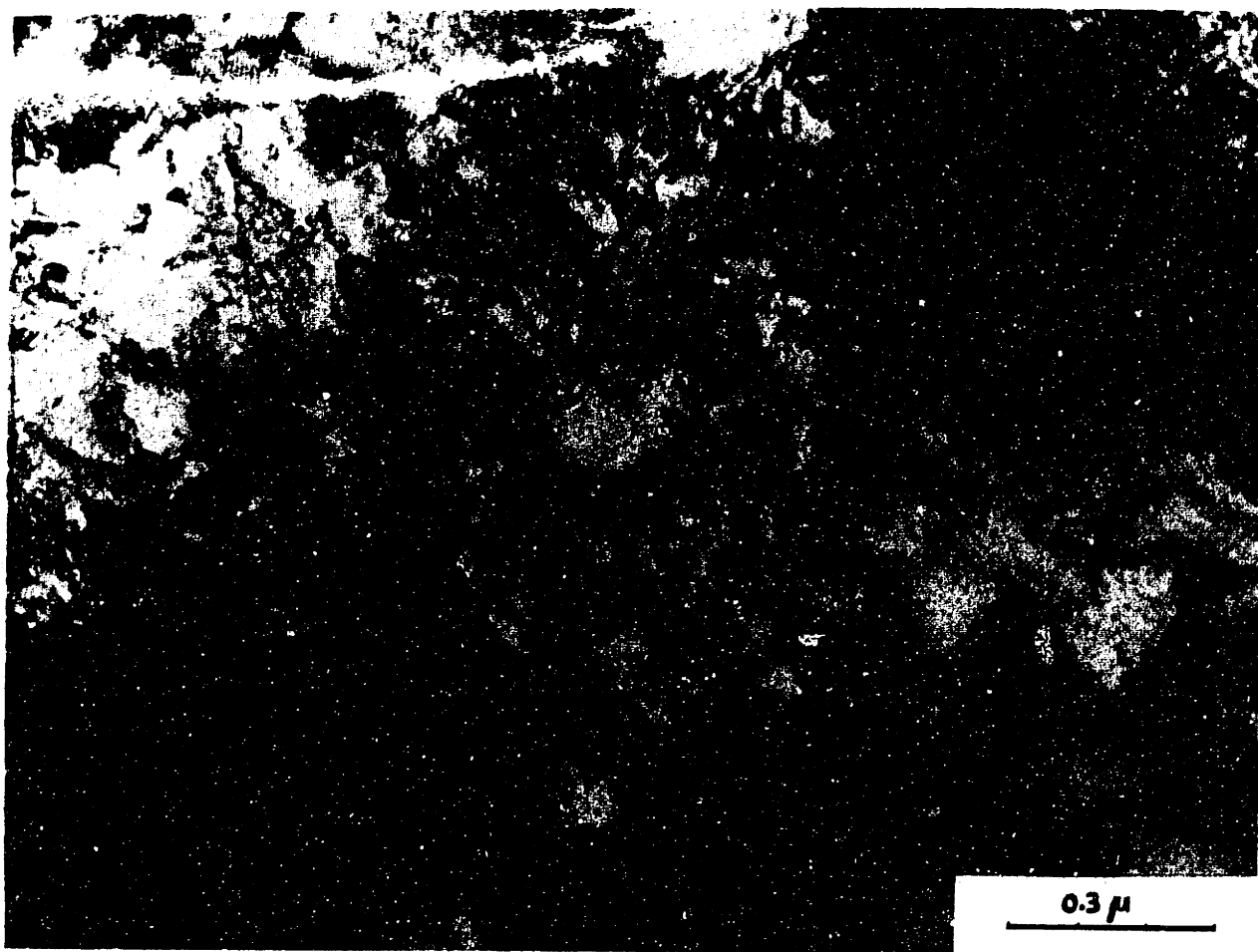
24

25

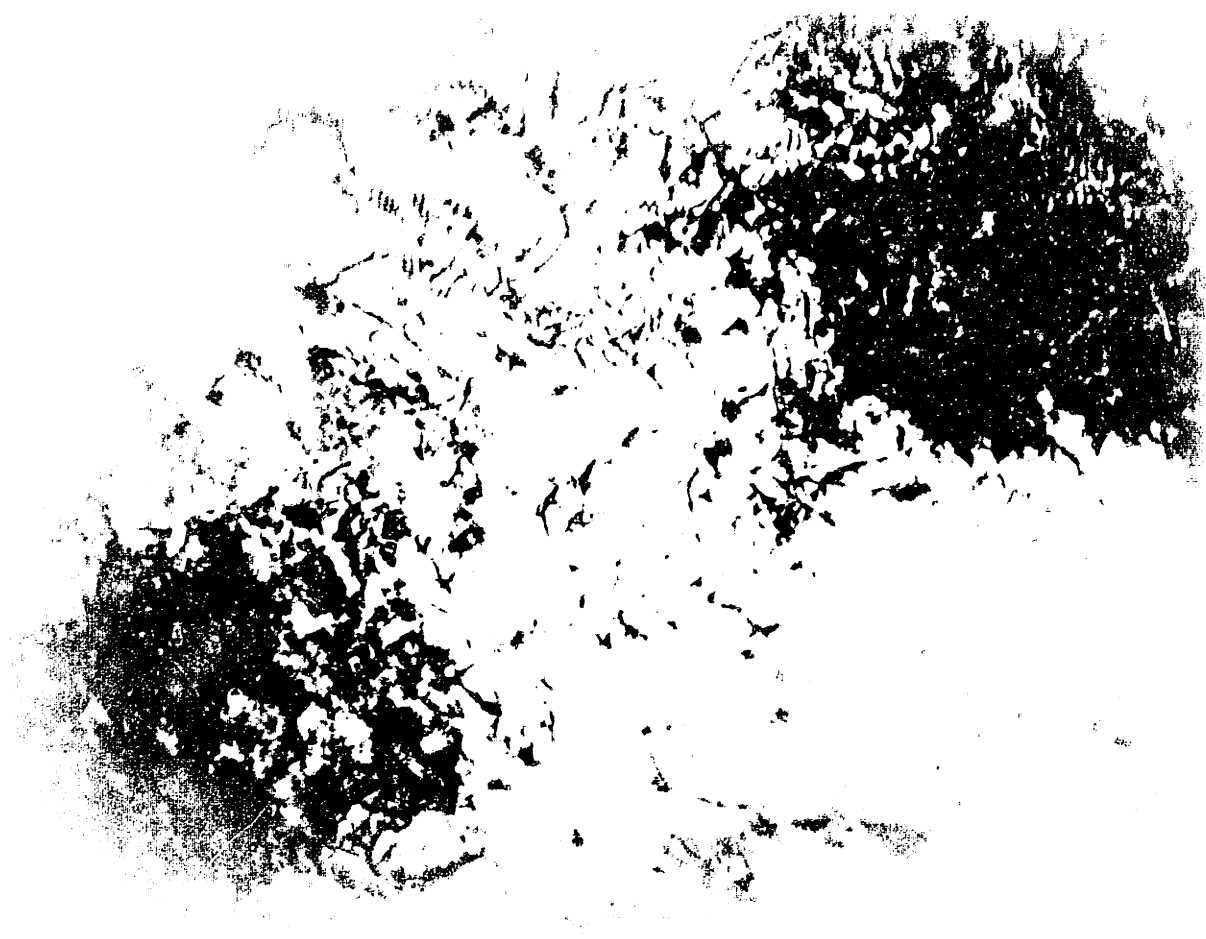




Figure 14 : Transmission electron micrograph of cold worked, stress relieved zircaloy 2.



- Figure 15 : Transmission electron micrograph of the dislocation structure in cold worked, stress relieved zircaloy 2.



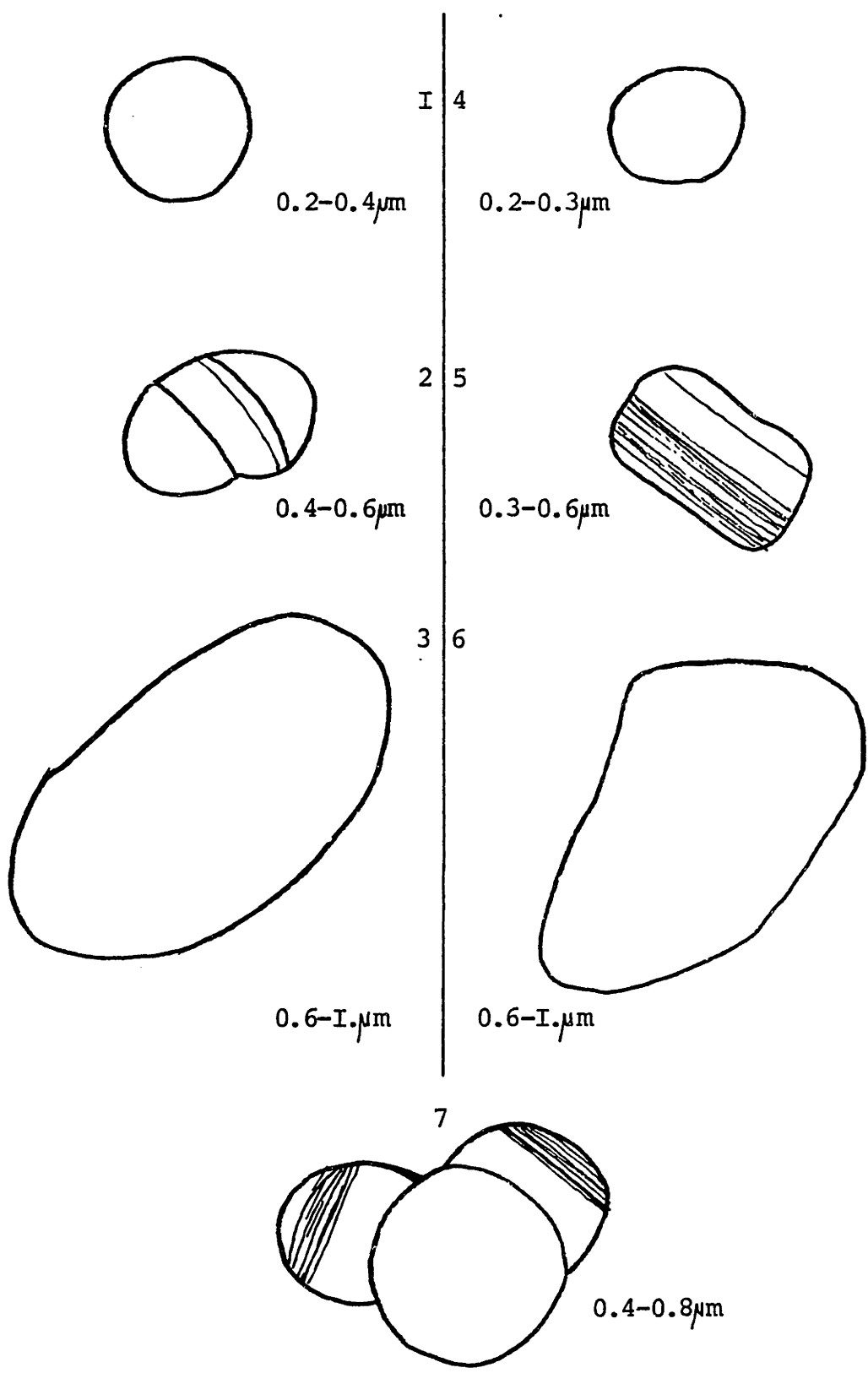
spots can be observed in Figure 13. The foils taken from the cold worked stress relieved tube exhibited a partially recrystallized structure (Figure 14). A few dislocation free grains of different sizes (0.5-5 μm), often in clusters, were observed within a very dislocated background. Very small particles (0.2 μ) were present along with a few particles larger than 1 μm within the grains and not preferentially at grain boundaries. Their observation was difficult within the very dislocated structure. A heterogeneity on a finer scale was observed in the high dislocation density region (Figure 15) where piled up dislocation lines were common. The unrecrystallized grains were elongated in a common direction probably close to the longitudinal axis of the tube.

IV.2c. Second phase particles

Second phase particles were found in the annealed and in the stress relieved material. Based on their appearance, the individual particles can be classified basically as six types (Figure 16). The chemical nature of the particles is the object of part IV.4 of this thesis. Perfectly spherical particles of small size (0.2-0.4 μm) were very common in the annealed material (Type 1). These particles normally diffracted strongly and were not etched preferentially. Some of the particles of type 1 showed bend contours and appeared as single crystals. Fewer, larger ovoid particles (0.4-0.6 μm) exhibited a polycrystalline structure with twins and stacking faults. Particles at grain boundaries were often of this type (type 2). Very few large ovoid particles (type 3, 0.6-1 μm), some slightly angular (type 6, 1 μm), were observed. Most of them were partially etched. Rectangular particles in the 0.2 to 0.6 μm range, exhibiting a thin band structure, probably twins or

Figure 16 :

Different types of intermetallic particles in zircaloy 2
 Ni-Fe-Zr particles type Cr-Fe-Zr particles



stacking faults for particular orientations of the beam, were very common (type 5). The largest type 5 particles were sometimes partially etched. Some small chromium iron zirconium particles of small size (0.2-0.3 μm) (type 4) can be confused with the nickel iron zirconium particles of type 1 unless electron diffraction or chemical analysis has been investigated. Particles containing chromium are usually more angular than particles containing nickel.

In the annealed plate, many clusters were observed and analyzed in the STEM. Their constitution was well defined: a central particle of type 2 with 1 or 2 type 5 particles attached on different sides. Most of the clusters were of 2 or 3 particles (type 7) and larger ones (5-6 particles) could be decomposed into smaller units of type 7.

The distribution of the individual particles and clusters was uniform. Measurement of the mean spacing between particles is very difficult in TEM because the foil is a wedge, the thickness is not always measurable and many particles were partially or completely etched out. Figure 13 is representative of the material. Particles are between 2 and 5 microns apart. The average size of the particles is 0.3 to 0.4 μm . Nickel rich and chromium rich particles were equally common.

The crystal structure of the particles was determined by electron diffraction. Several patterns were obtained for the same particle in many cases. The lattice spacings were determined assuming a hexagonal matrix with lattice parameters $a_0 = 3.232 \text{ \AA}$ and $c_0 = 5.147 \text{ \AA}$ (as pure zirconium). The accuracy of the calculated parameters is no better than 1% even with very careful measurements made directly on the emulsion side of the negative and when the matrix spots used to calculate the camera

Table 4 : Basic crystallographic data of zirconium compounds.

Composition	Structure	Parameters (in Å)	A.S.T.M. Card N°
Zr Cr ₂	Hexagonal	a = 5.079 c = 8.279	6-0613
Zr ₂ Ni	Tetragonal	a = 6.499 c = 5.270	19-857
Zr Fe ₂	Cubic (Cu ₂ Ni type)	a = 7.070	18-666
Zr ₄ Sn	Tetragonal	a = 6.90 c = 11.10	10-185
Zr (α)	Hexagonal	a = 3.232 c = 5.147	5-0665
Hydride γ ¹	Tetragonal	a = 4.617 c = 4.888	*
Zr O ₂	Monoclinic	a = 5.1477 b = 5.2030 c = 5.3156 β = 99° 23'	13-307

* Bailey, J.E., Acta Met. II, (1963) 278

constant were on the same negative.

It has been difficult to index several individual diffraction patterns of particles because of the lack of accuracy of the measurements and because the parameters of the phases are not precisely known.

Our results are in good agreement with the results of PRAO (18). Basic crystallography data for zirconium and zirconium binary compounds are summarized in Table 4. Complementary information is available in the Appendix C of this thesis.

The result of the present study is: (a) Particles of type 1-2-3 have the same tetragonal structure as Zr_2Ni . A particle of type 3, partially etched in the center is presented in Figure 17. A small particle containing chromium is attached on one side. The square (001) electron diffraction pattern included is characteristic of the structure with $d_{110} = 4.60 \text{ \AA}$ corresponding to $a_0 = 6.51 \text{ \AA}$. Other important patterns such as (110), (011), (111) and (012) were observed. (b) Particles of type 4-5-6 have a hexagonal structure and the same crystallographic parameters as $ZrCr_2$ within the accuracy of the measurements. Figure 18 is an example of a particle of type 6, partially etched and showing an internal lamellar structure in dark field (inset d). Figure 19 shows several particles of type 4. The hole on the right side probably corresponds to a particle which has been etched out. Important poles of the hexagonal structure such as (0001), ($1\bar{2}10$), ($10\bar{1}0$), ($1\bar{2}13$) or ($10\bar{1}2$) were observed. The cluster shown in picture 20 is of the type 7 previously described. The central particle is of the type Zr_2Ni and two chromium rich particles of the $ZrCr_2$ type are attached. The type 5 particles were twinned perpendicularly to the

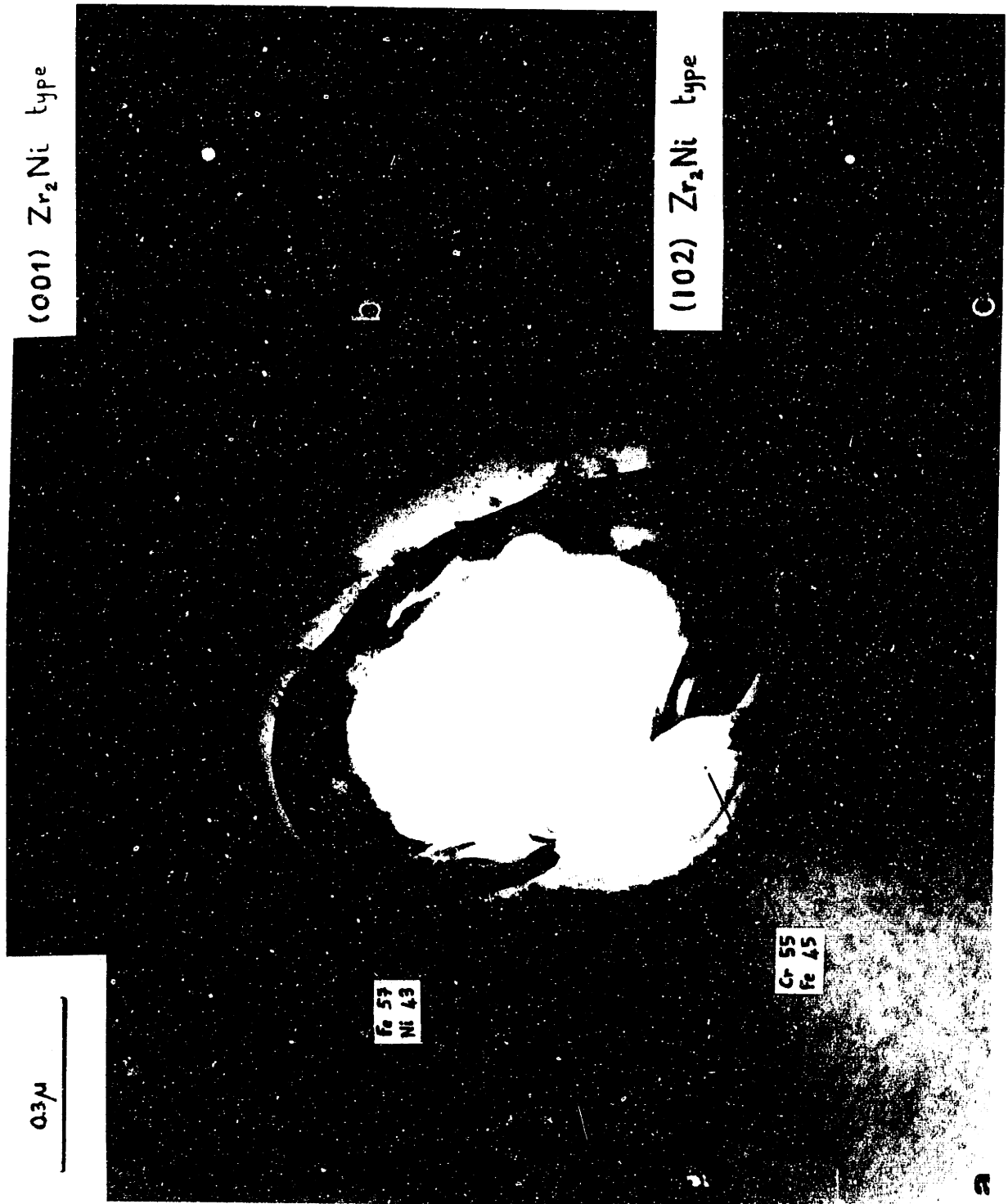
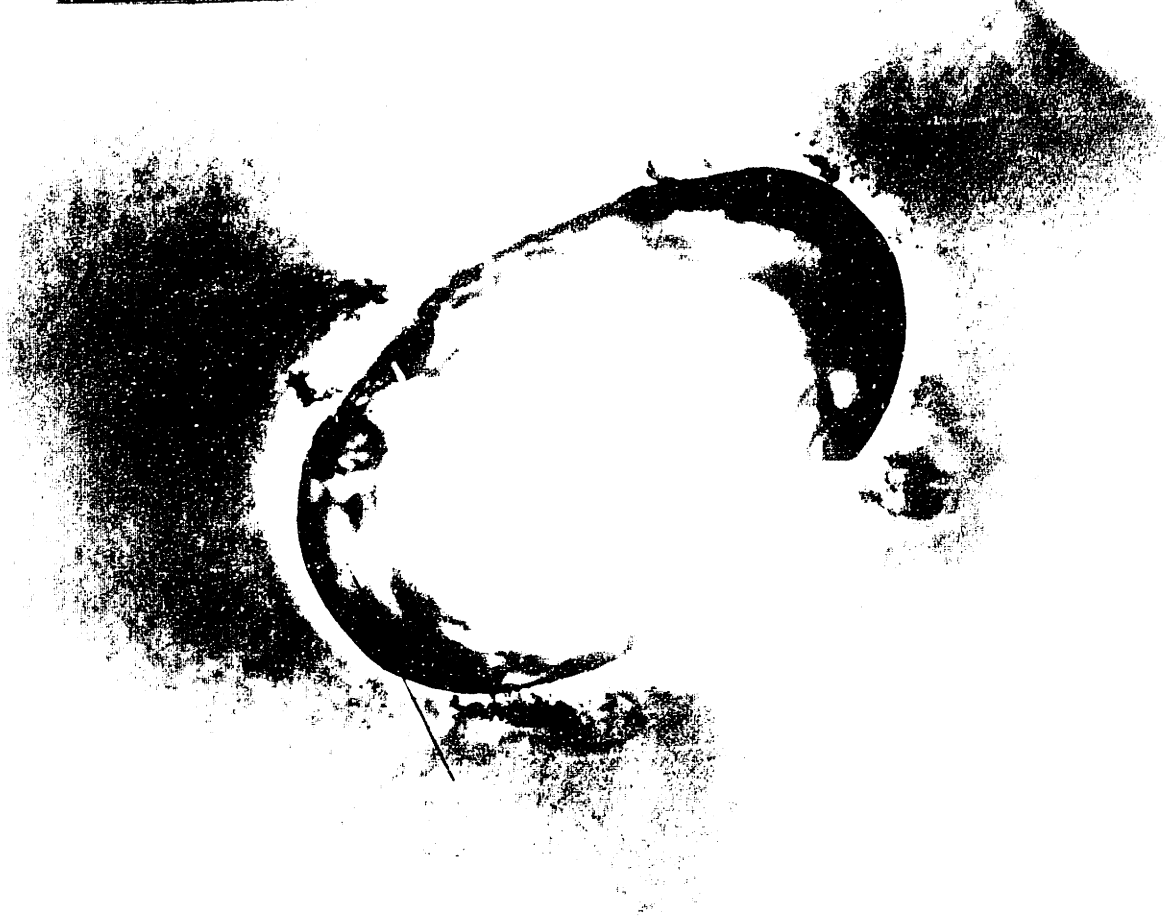
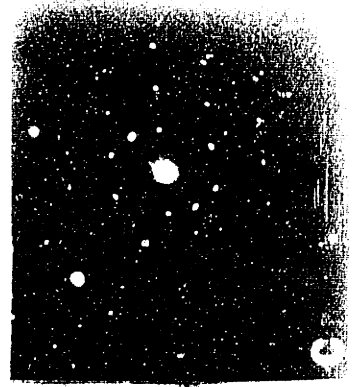
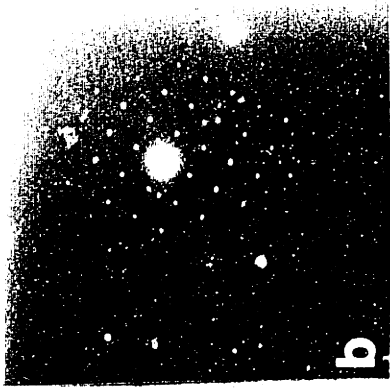


Figure 17 : Transmission electron micrograph of a nickel-iron rich particle in annealed zircaloy 2.
 a) Bright field image.
 b) (001) electron diffraction pattern.
 c) (102) electron diffraction pattern.



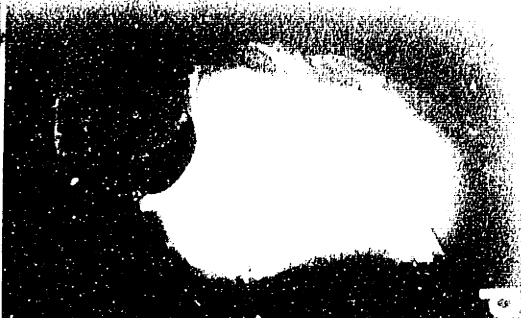
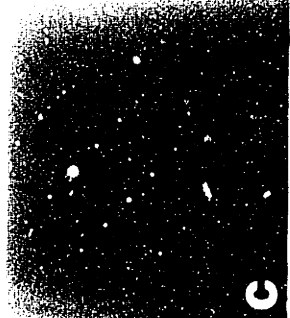
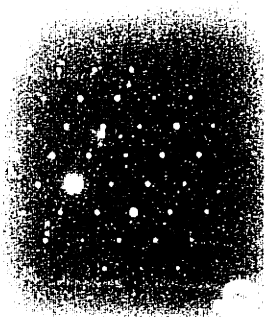




Figure 18 : Transmission electron micrograph of a chromium-iron rich particle in annealed zircaloy 2.
 a) Bright field image.
 b) (1213) electron diffraction pattern.
 c) (5416) electron diffraction pattern.
 d) Dark field image corresponding to a (2021) reflexion.

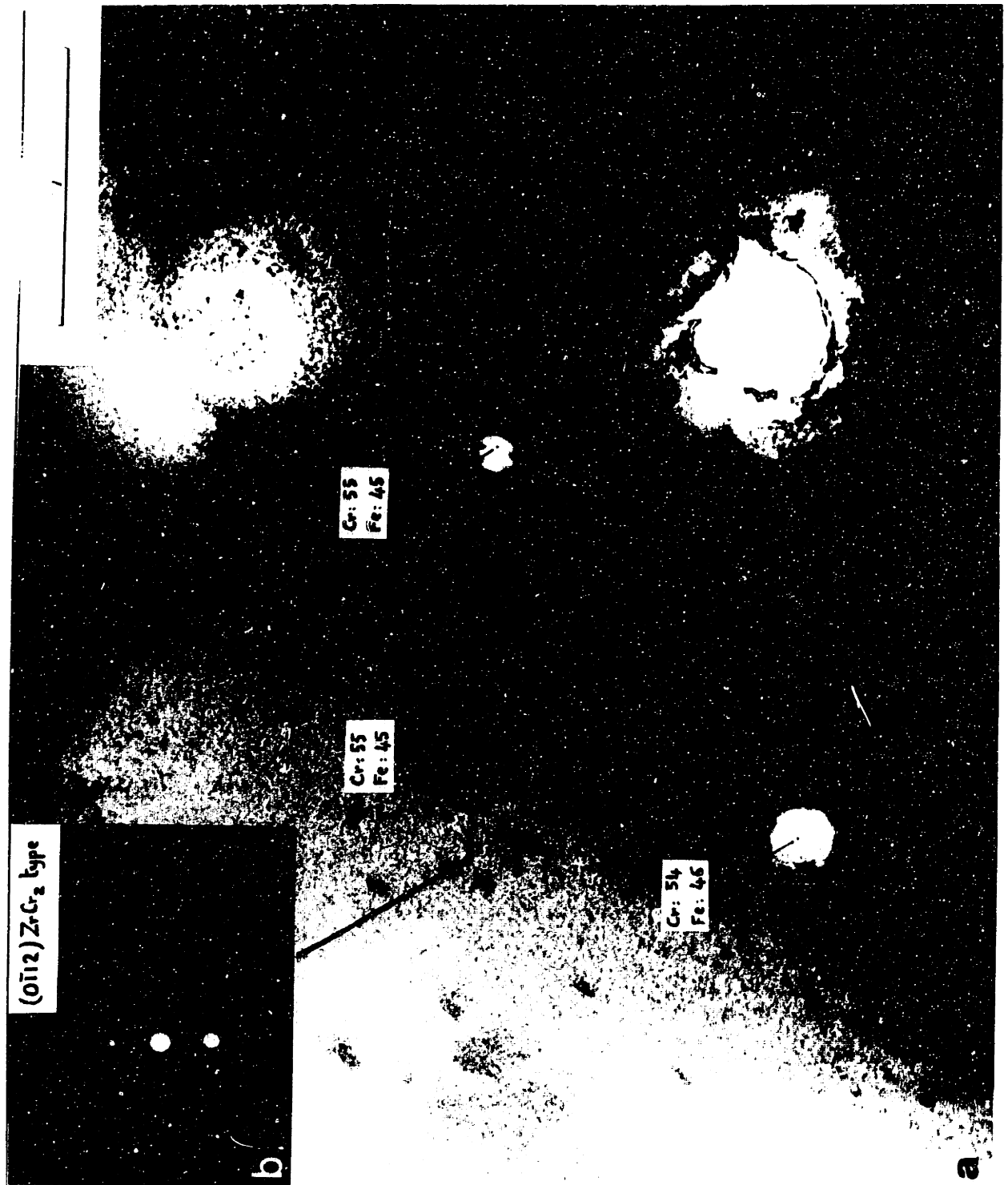


Figure 19 : Transmission electron micrograph of chromium-iron rich particles in annealed zircaloy 2.
 a) Bright field image.
 b) (0112) electron diffraction pattern.

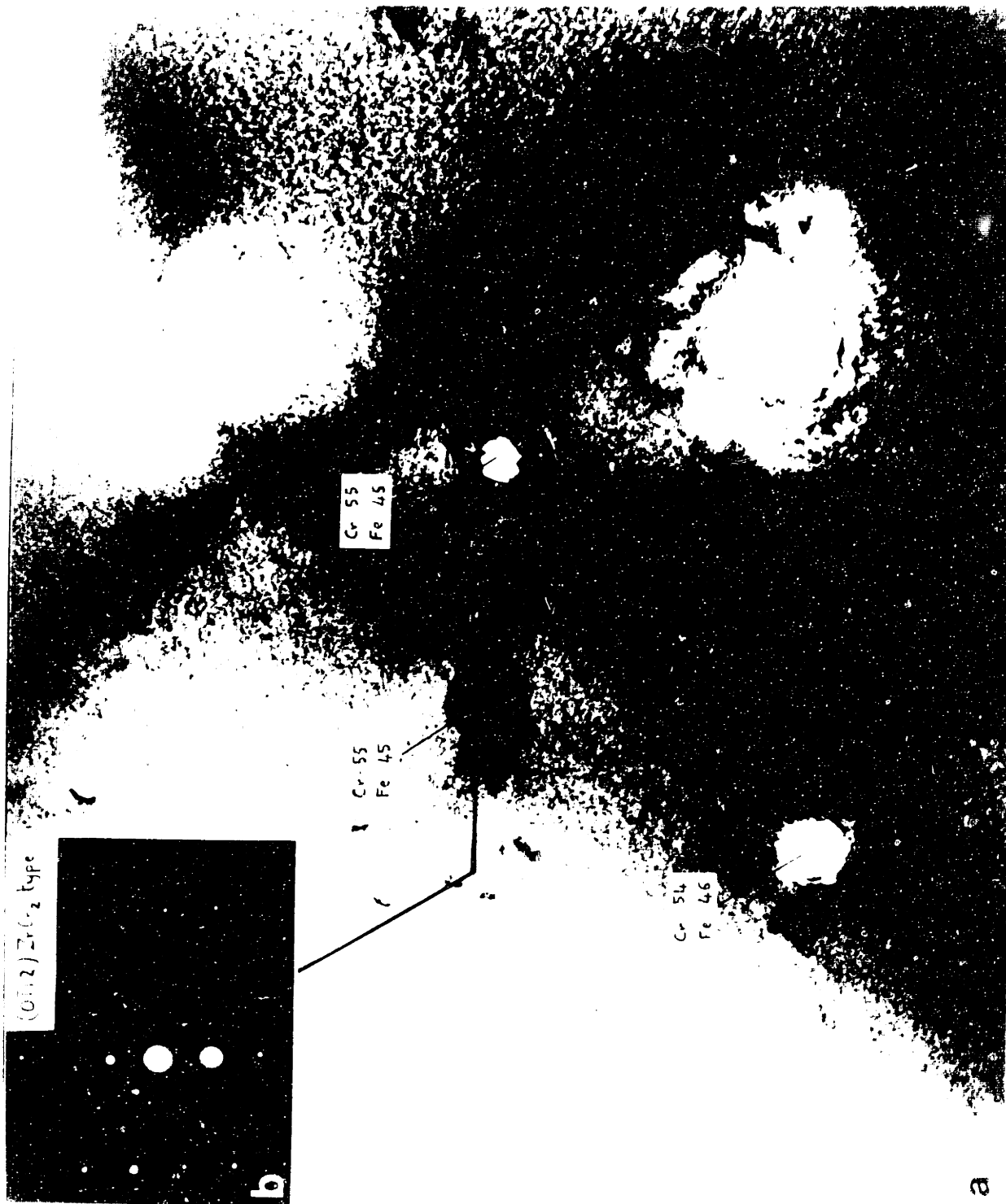


Figure 19: Transmission electron micrograph of randomly distributed rich particles in an Fe-Cr alloy. (a) bright field image; (b) selected area electron diffraction pattern.

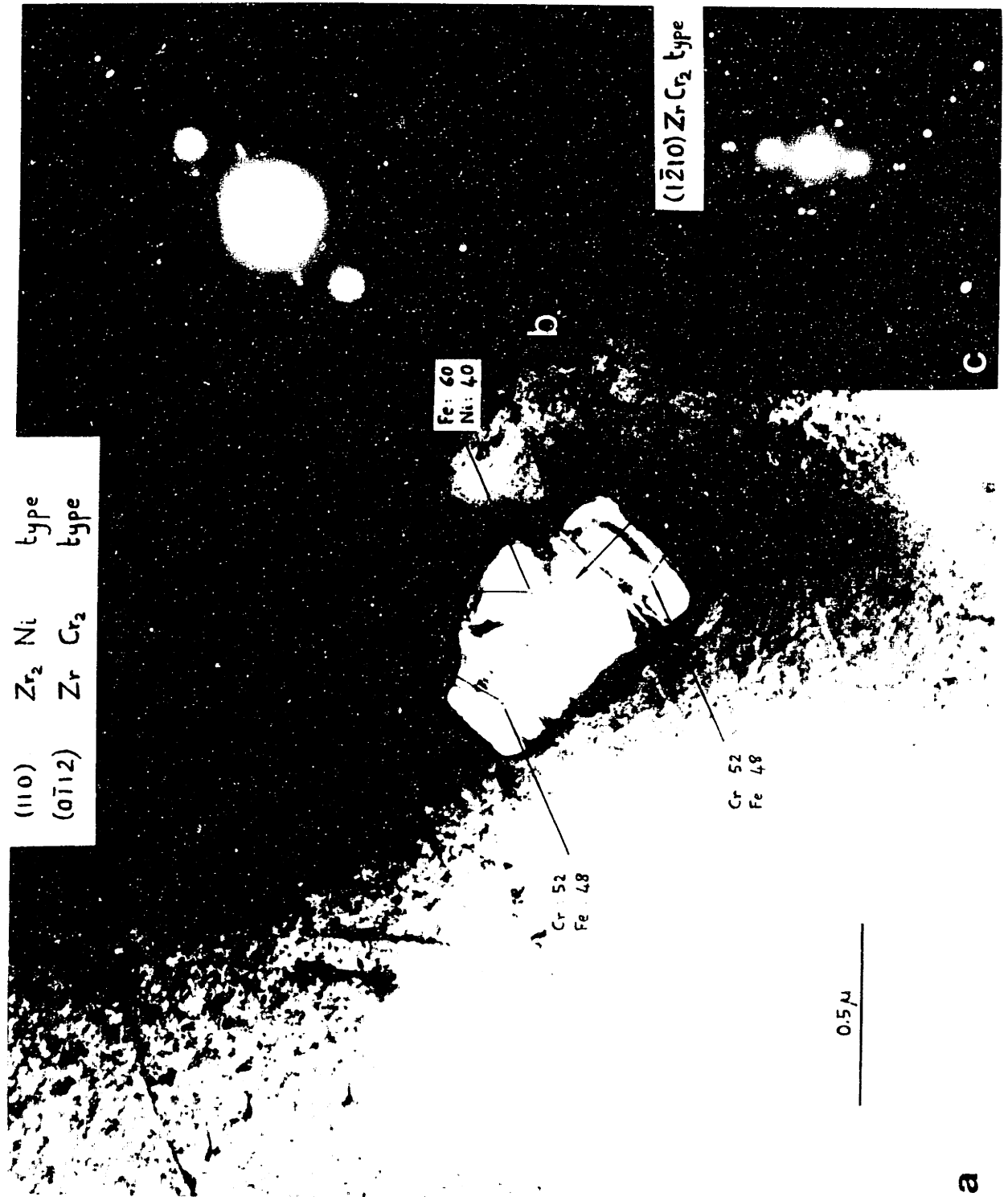


Figure 20 : Transmission electron micrograph of a cluster of intermetallic particles in annealed zircaloy 2.
 a) Bright field image.
 b) (110) and (0112) electron diffraction patterns.
 c) (1210) electron diffraction pattern.

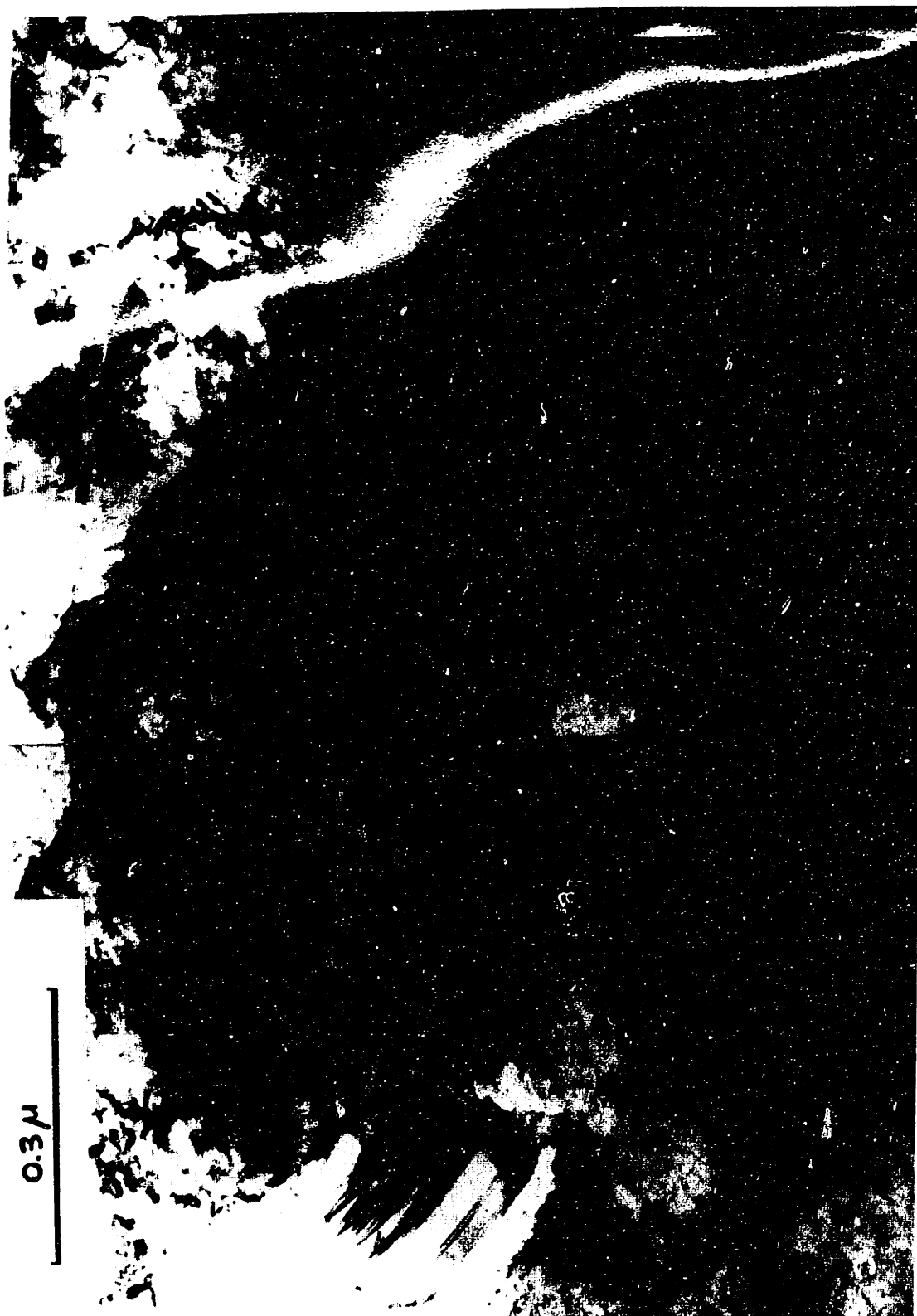


Figure 21 : Transmission electron micrograph of intermetallic particles in cold worked, stress relieved zircaloy 2.

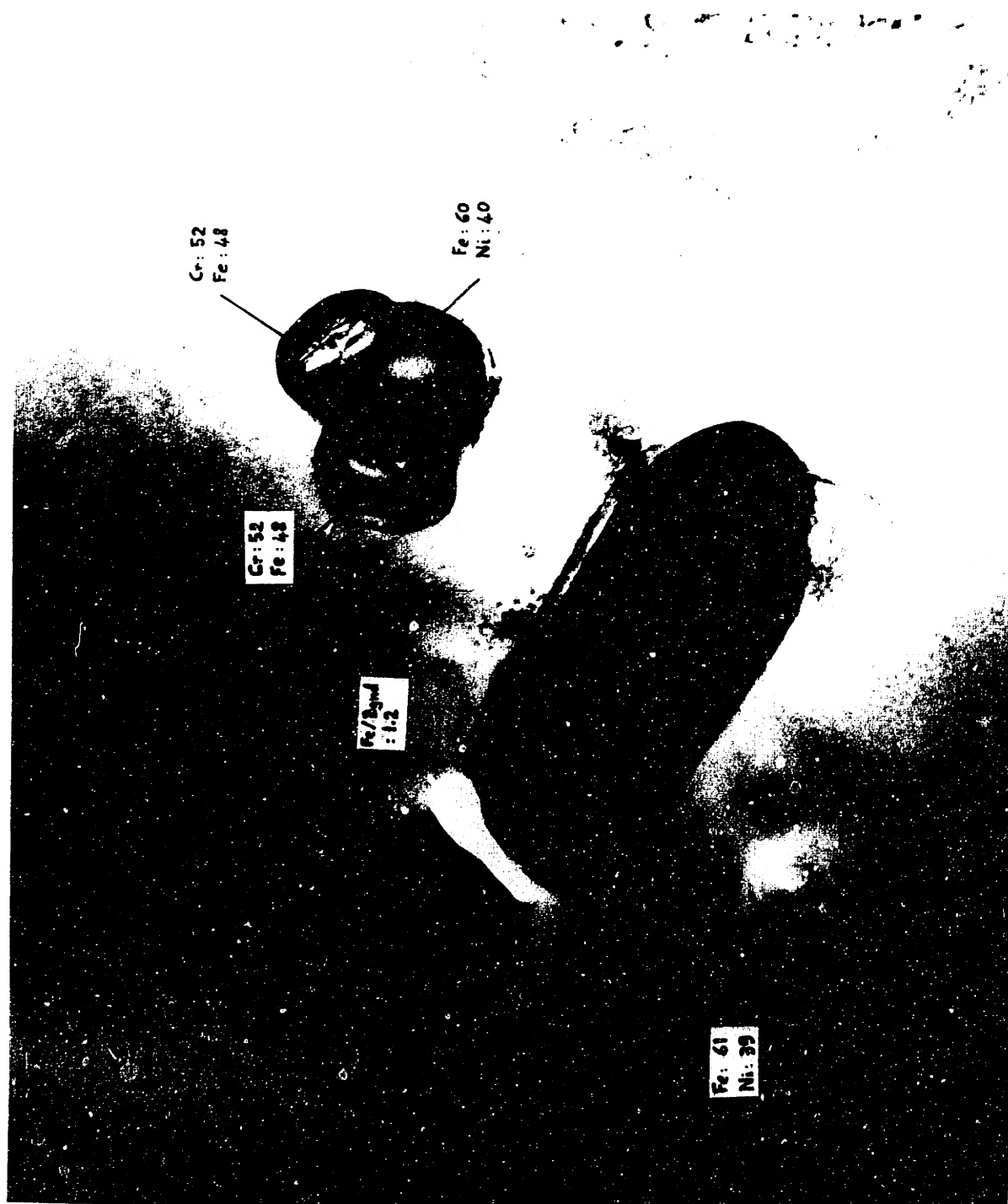


Figure 22 : Transmission electron micrograph of intermetallic particles close to an inclusion in annealed zircaloy 2.

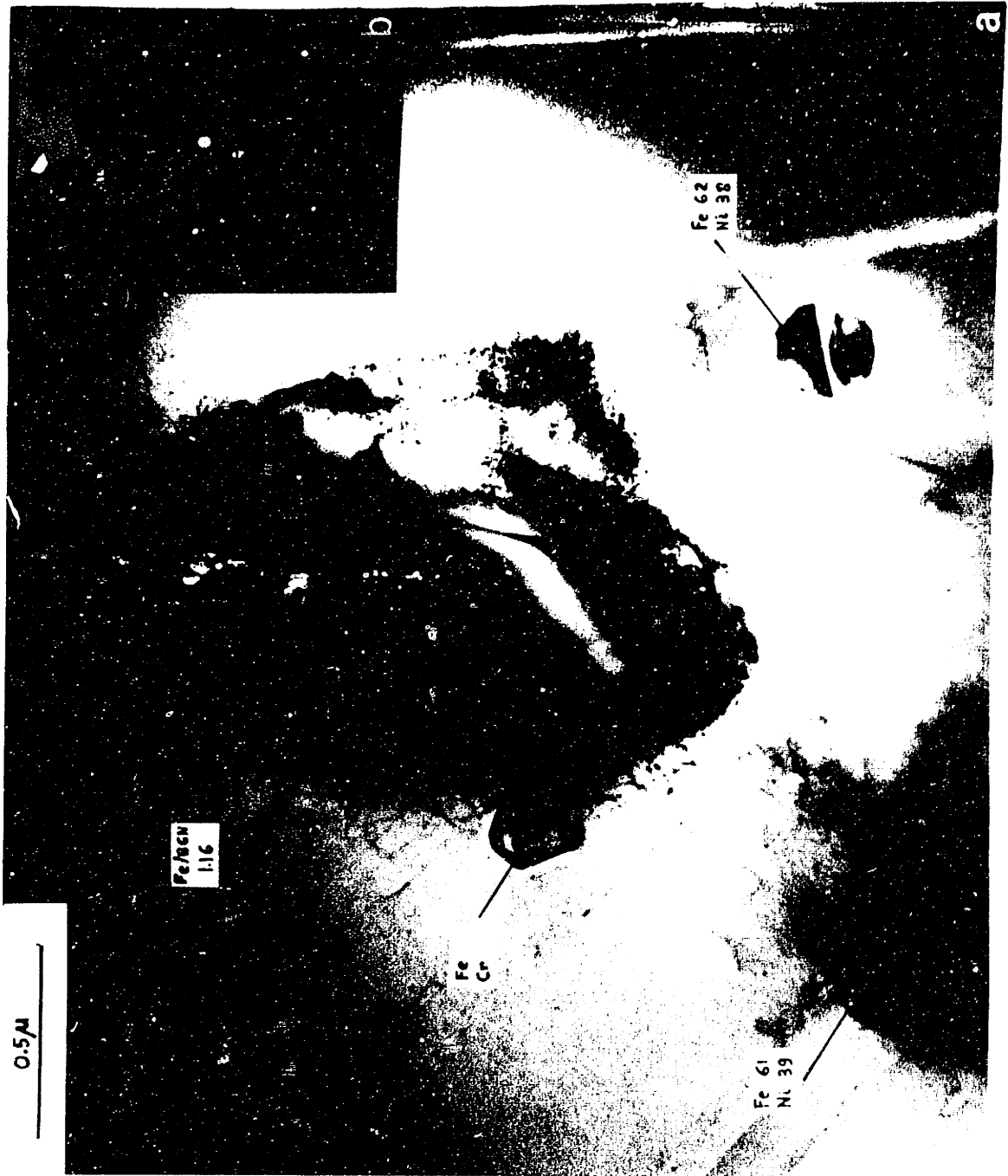


Figure 23 : Transmission electron micrograph of a Zr_3Si inclusion in annealed zircaloy 2.
 a) Bright field image.
 b) (011) electron diffraction pattern.

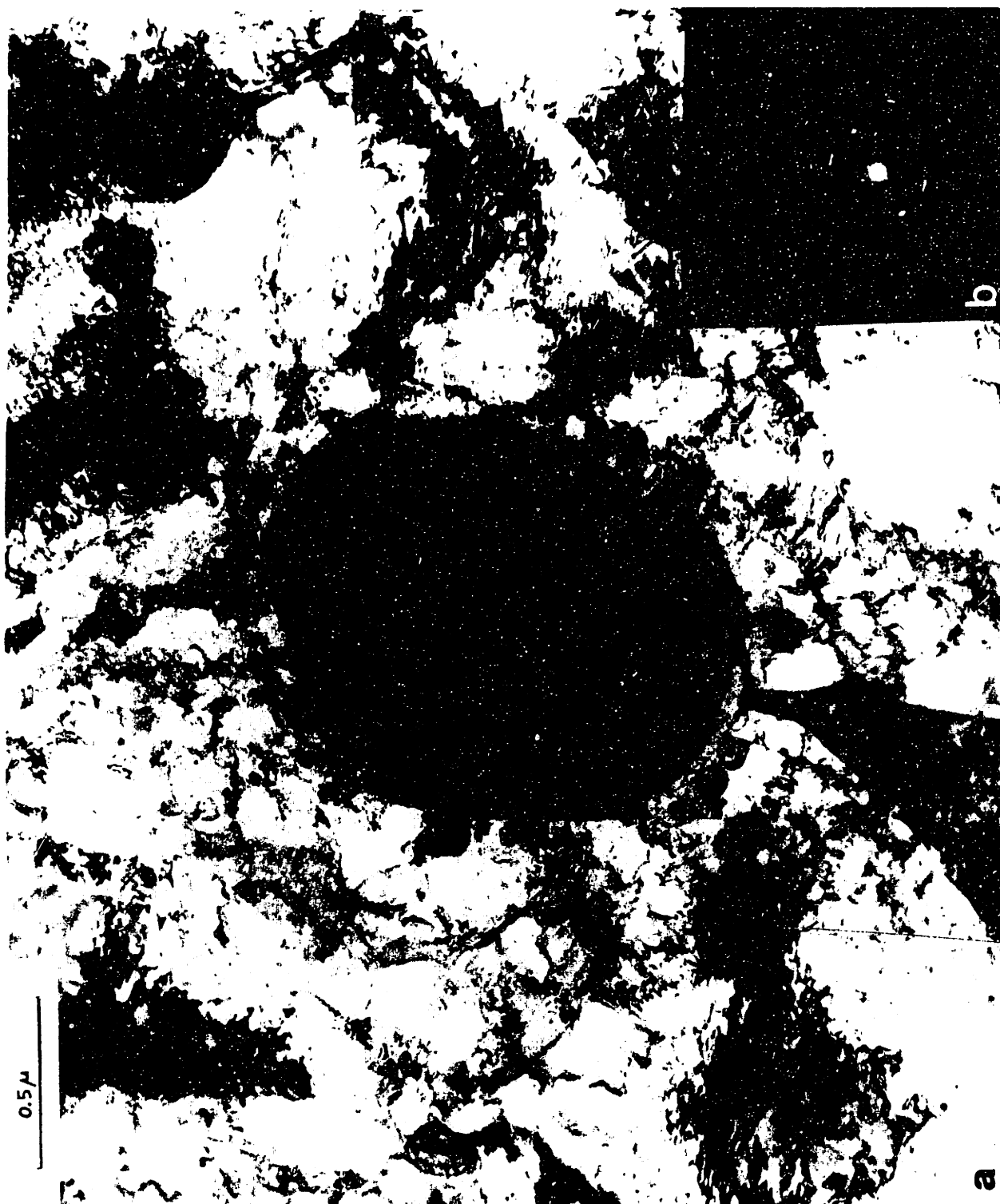


Figure 24 : Transmission electron micrograph of a Zr_3Si inclusion in cold worked, stress relieved zircaloy 2.

a) Bright field image.

b) (013) electron diffraction pattern.



Figure 24 : Transmission electron micrograph of a Zr_3Si inclusion in cold worked, stress-relieved zircaloy 2.
a) Bright field image.
b) (013) electron diffraction pattern.

<0001> direction and, in diffraction, streaks were often observed in this direction. For the cluster of Figure 20a, it was possible to show that the two particles have a strong crystallographic relationship, two sets of planes being parallel. The cold worked stress relieved material contains the same types of particles but their structures have not been determined by electron diffraction. The same type of particle was of smaller average size in the cold worked, stress relieved material than in the annealed material. Figure 21 shows a type 1 and a type 5 particle next to a dislocation network.

IV.2d. Inclusions

Large inclusions (1-2 μm), often elongated, were observed in annealed and in stress relieved zircaloy 2. They were not very common (about one per thin foil in the annealed plate). The inclusions were often too thick to give good electron diffraction patterns, however a tetragonal structure with $a_0 = 11 \text{ \AA}$ and $c_0 = 5.5 \text{ \AA}$ fitted nearly all the patterns. Such a structure has been reported for silicides of the type Zr_3Si by Schubert (29) and was suggested by D. Charquet (30). Two such inclusions are showed in Figures 22 and 23. The cluster of type 7 on Figure 22 presents a slight Moiré pattern corresponding to a hydride. Very few intermetallic particles were observed on the inclusions but they are often present in the neighboring matrix. The observed inclusions were more elongated in the annealed material than in the stress relieved material. Figure 24 shows the slight misorientation between two components of a Zr_3Si type inclusion in the stress relieved material.

IV.3. Scanning transmission electron microscopy

In order to determine the chemical nature of the precipitates in zircaloy 2, a Vacuum Generators HB5 dedicated STEM was used. It provides a very good spatial resolution for X-Ray analysis (electron beam smaller than 20 \AA in diameter).

One can have a good idea of the repartition of the particles by looking at the annular dark field image in the STEM (Figure 25). This imaging mode was also useful when looking at particles in thick regions of the foil. For X-Ray analysis, the beam was centered on the particle of interest. A counting time of 15 to 120 seconds was enough to provide accurate information. The spectra were recorded and characteristic indices were calculated as described in Part III.2c. of this thesis. Chemically, two very distinct types of intermetallic particles were found. (a) Particles of type 1-2 and 3 showed only nickel and iron besides zirconium. Figure 26 shows a typical spectrum from a nickel-iron rich particle. The statistics demonstrate a very precise chemical composition for these particles. A Fe/Ni ratio of 60/40 can be inferred from Figure 27. The scatter of the Zr index should be considered as a matrix effect. However all the data are above 0.5.

(b) Particles of type 4-5-6 showed very similar results. They are composed of chromium, iron and zirconium (no tin or nickel). The Fe/Cr ratio of 45/55 is fairly constant. An example of spectra and statistics are given in Figures 28 and 29. The scatter of the Zr index is very large with a lower limit of 0.22. The extraction on carbon films is described in Part III.2b. of the thesis. The analyses in the STEM showed that the nickel rich particles were not extracted. All the

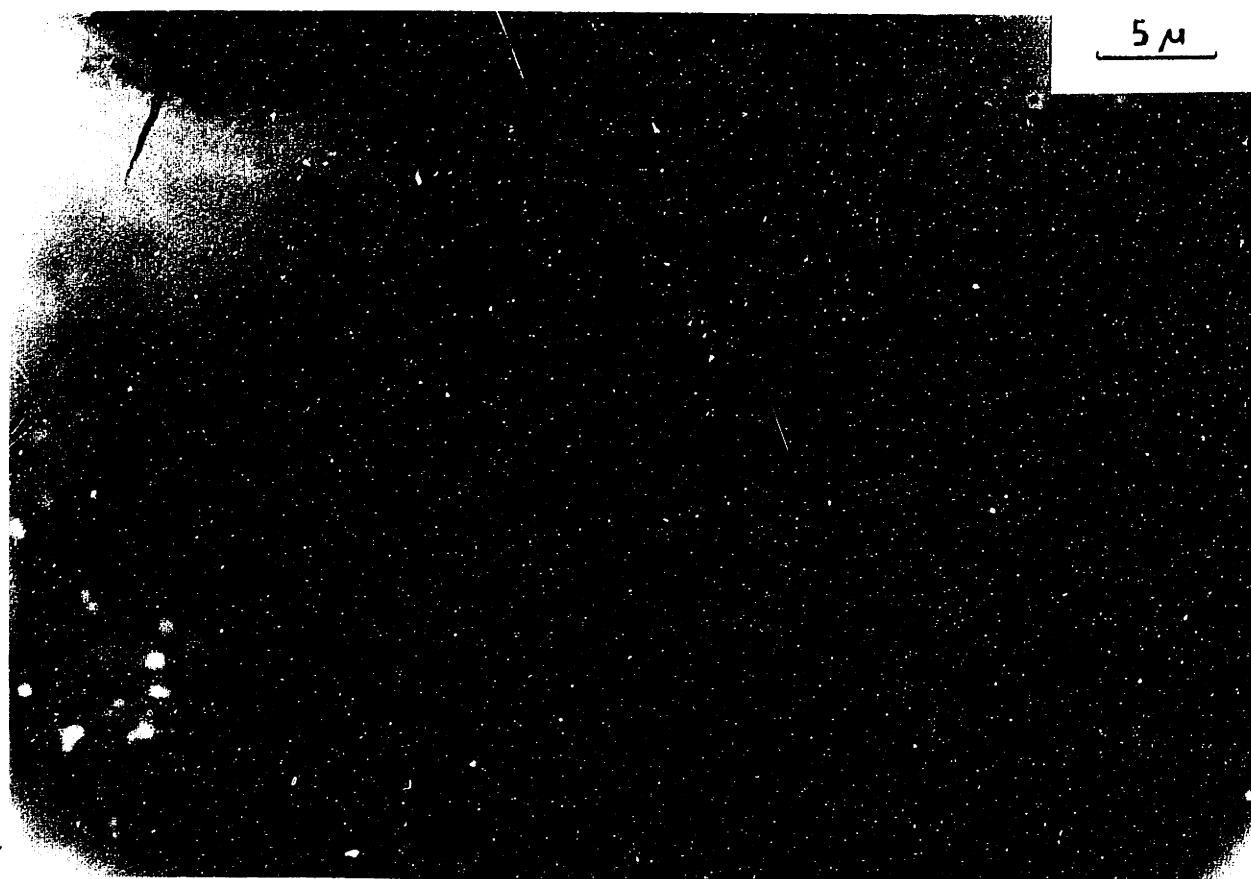
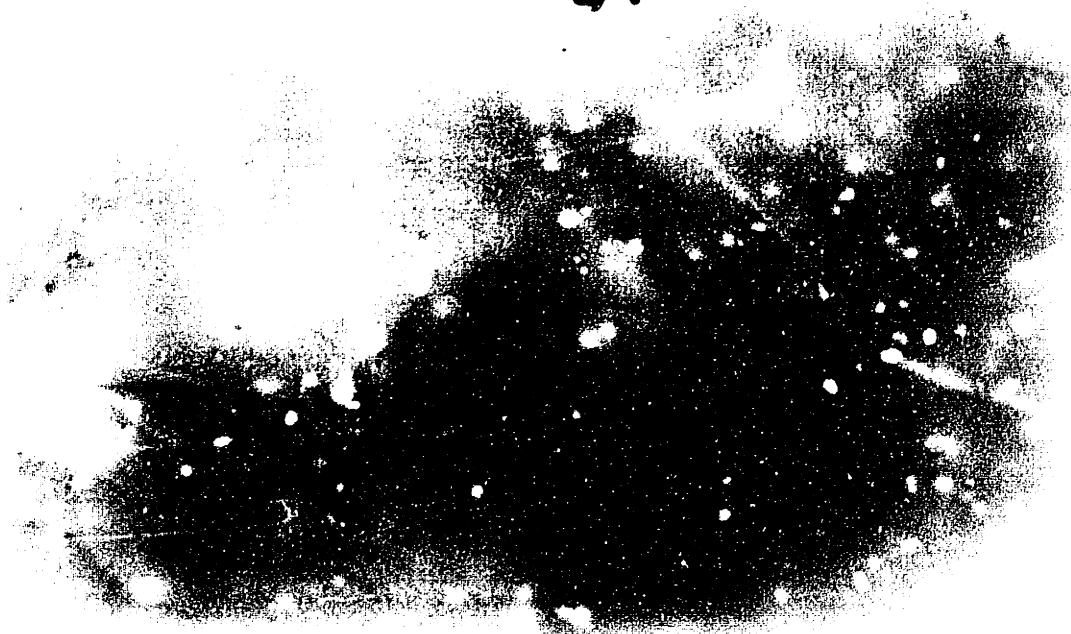


Figure 25 : Scanning transmission electron microscope (S.T.E.M.)
image of annealed zircaloy 2.
Low magnification annular dark field image.



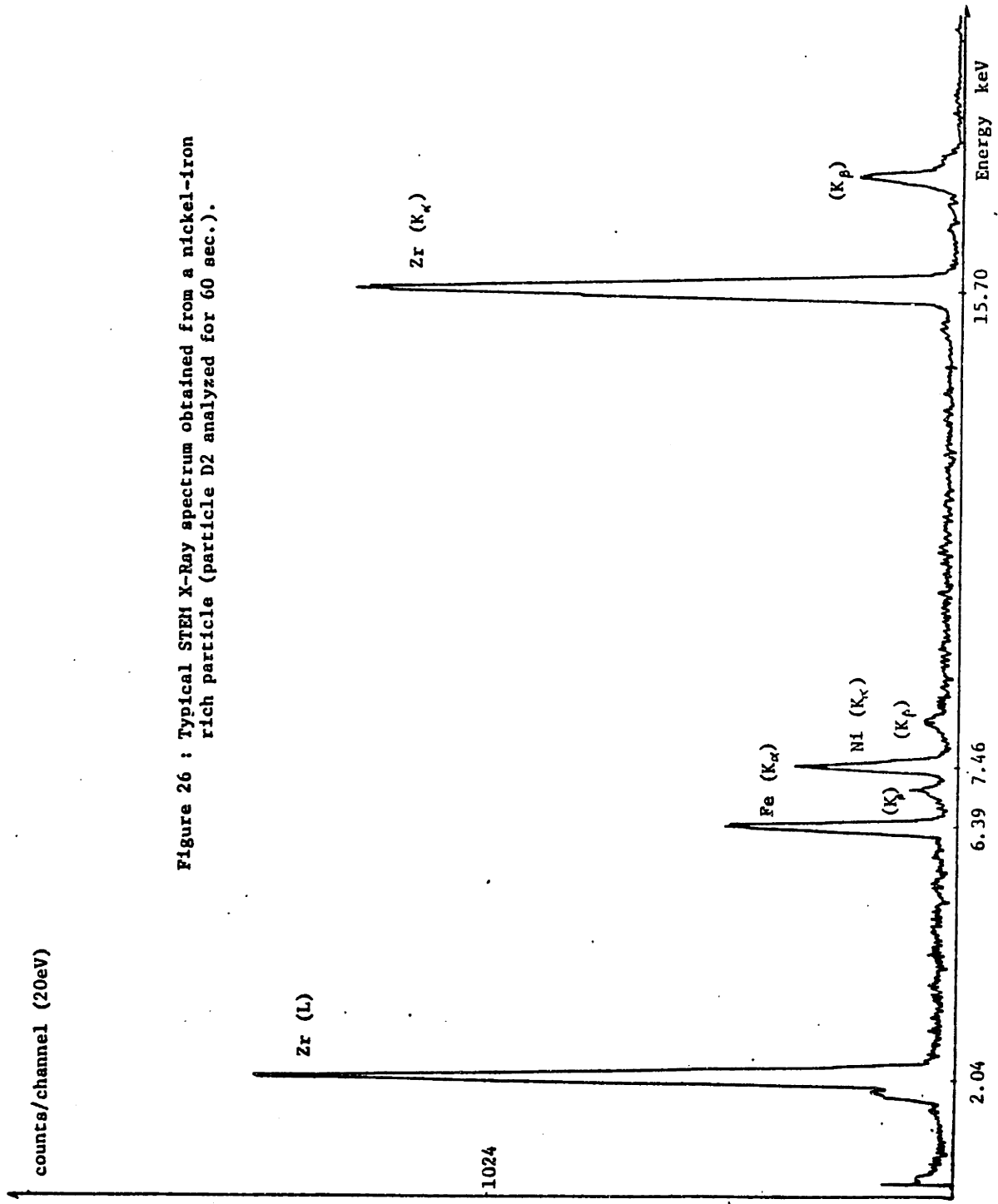


Figure 26 : Typical STEM X-Ray spectrum obtained from a nickel-iron rich particle (particle D2 analyzed for 60 sec.).

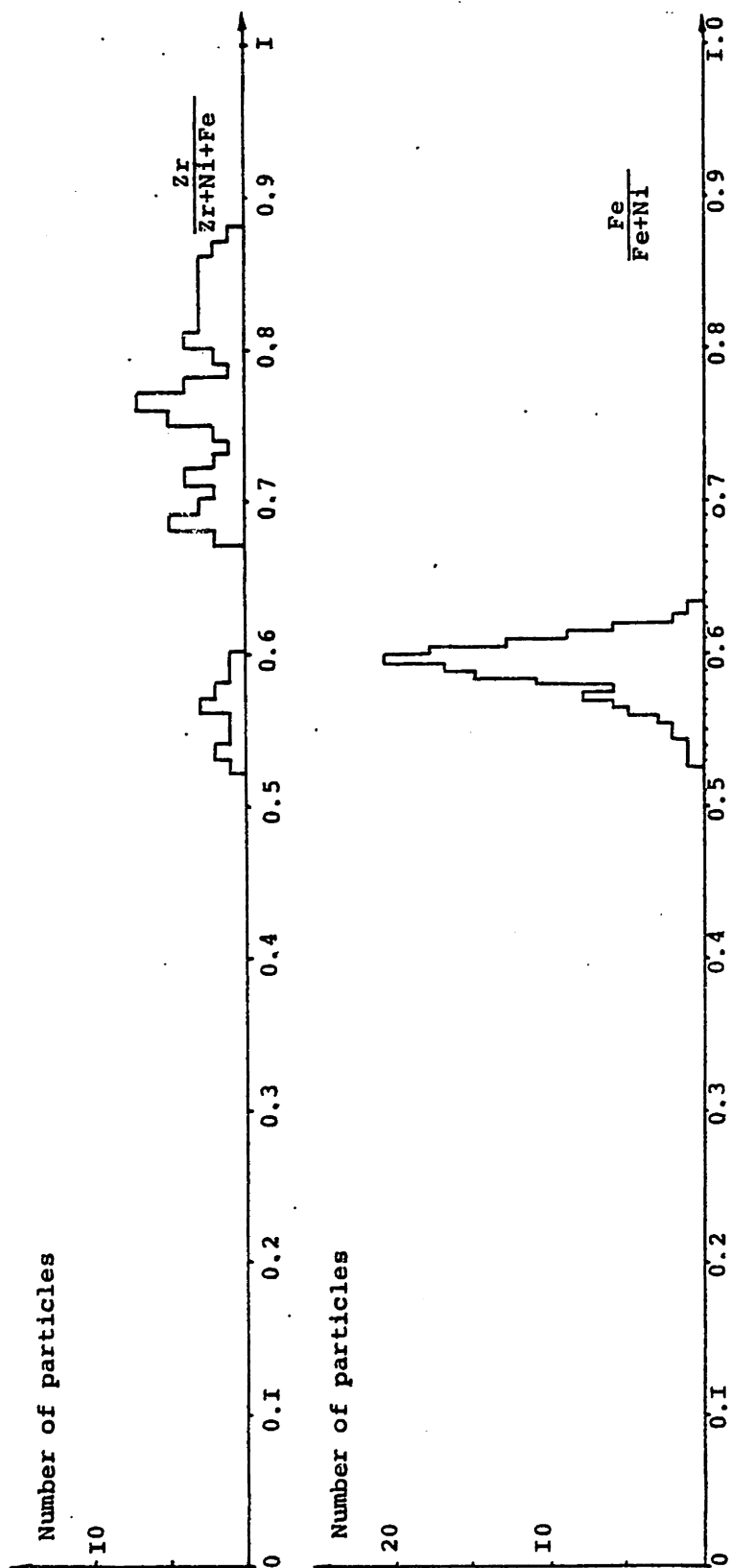


Figure 27 : Statistical distribution of the nickel-iron rich particles analysed in situ.

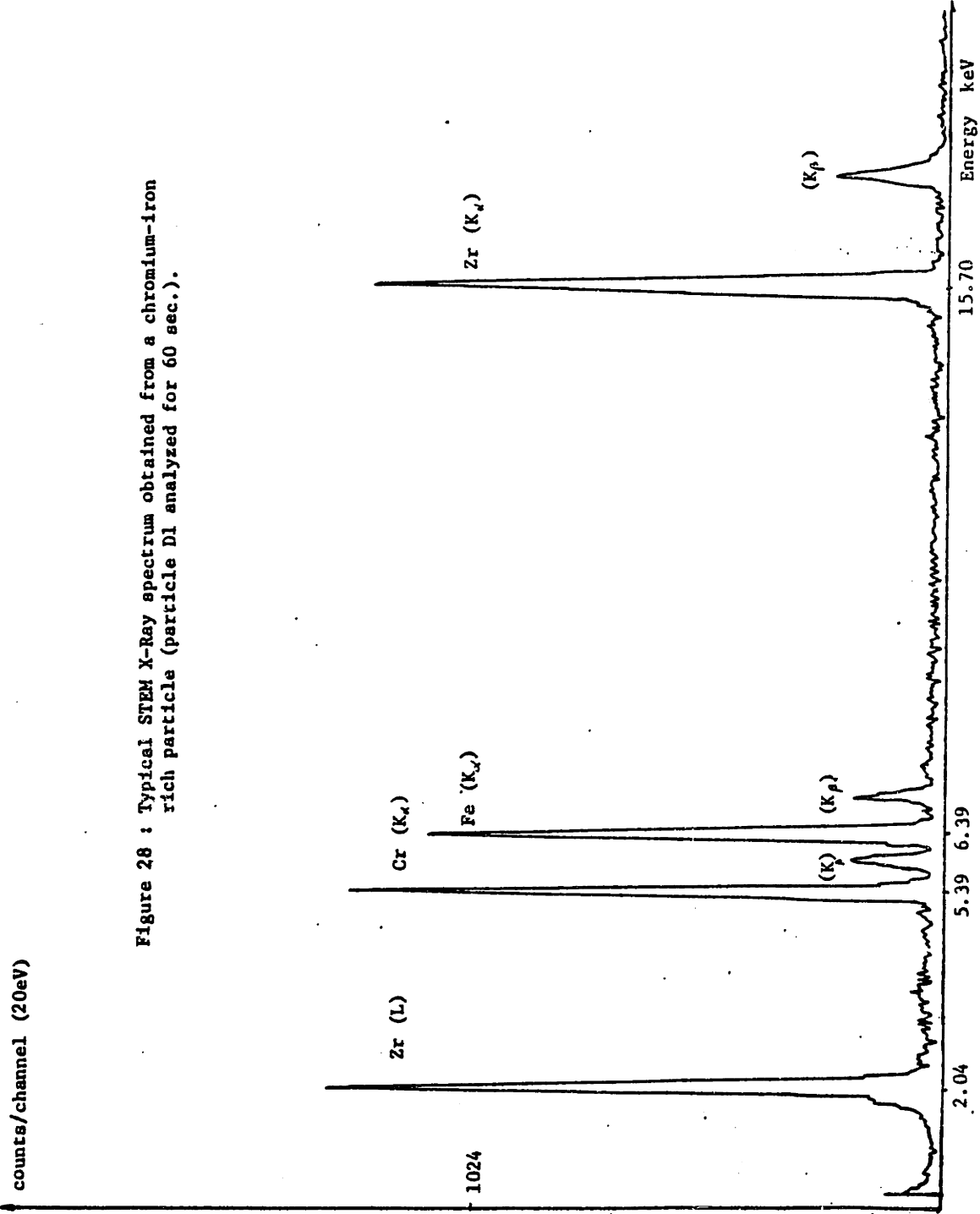


Figure 28 : Typical STEM X-Ray spectrum obtained from a chromium-iron rich particle (particle D1 analyzed for 60 sec.).

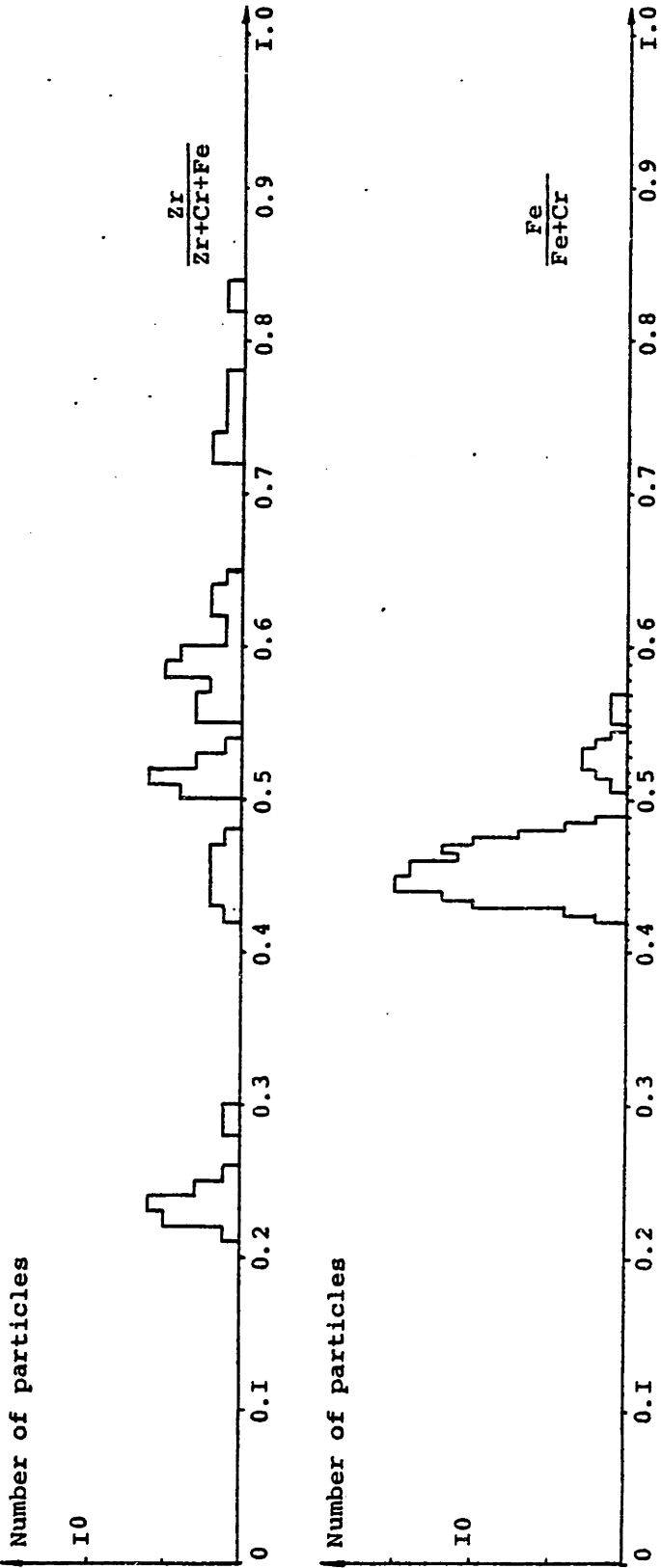


Figure 29 : Statistical distribution of the chromium-iron rich particles analyzed in situ.

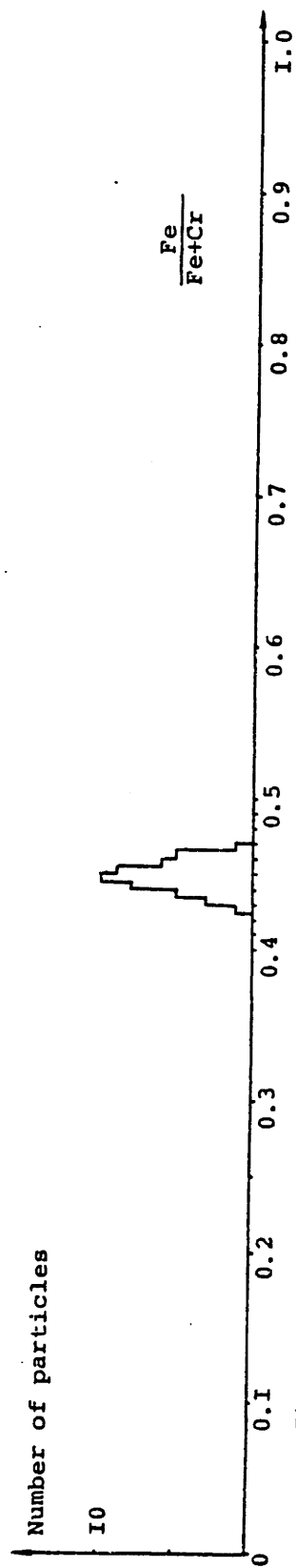
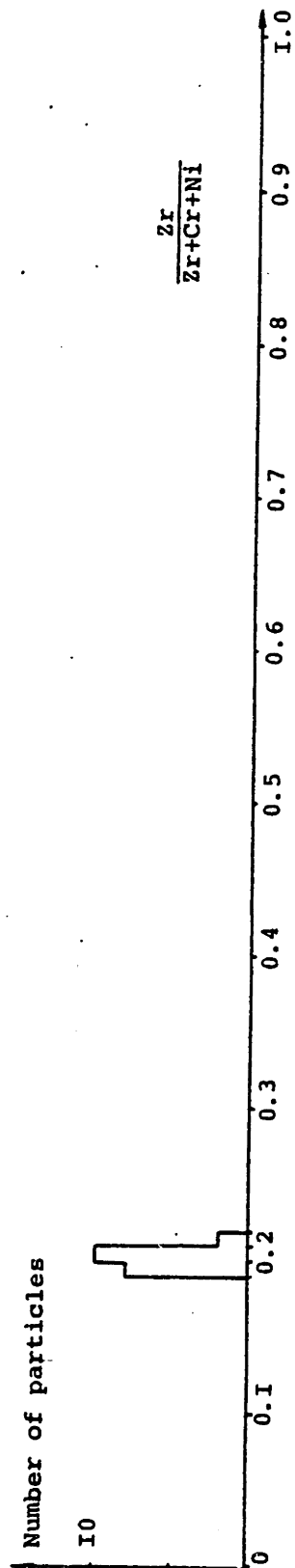


Figure 30 : Statistical distribution of the chromium-iron rich particles analyzed on extraction replicas.

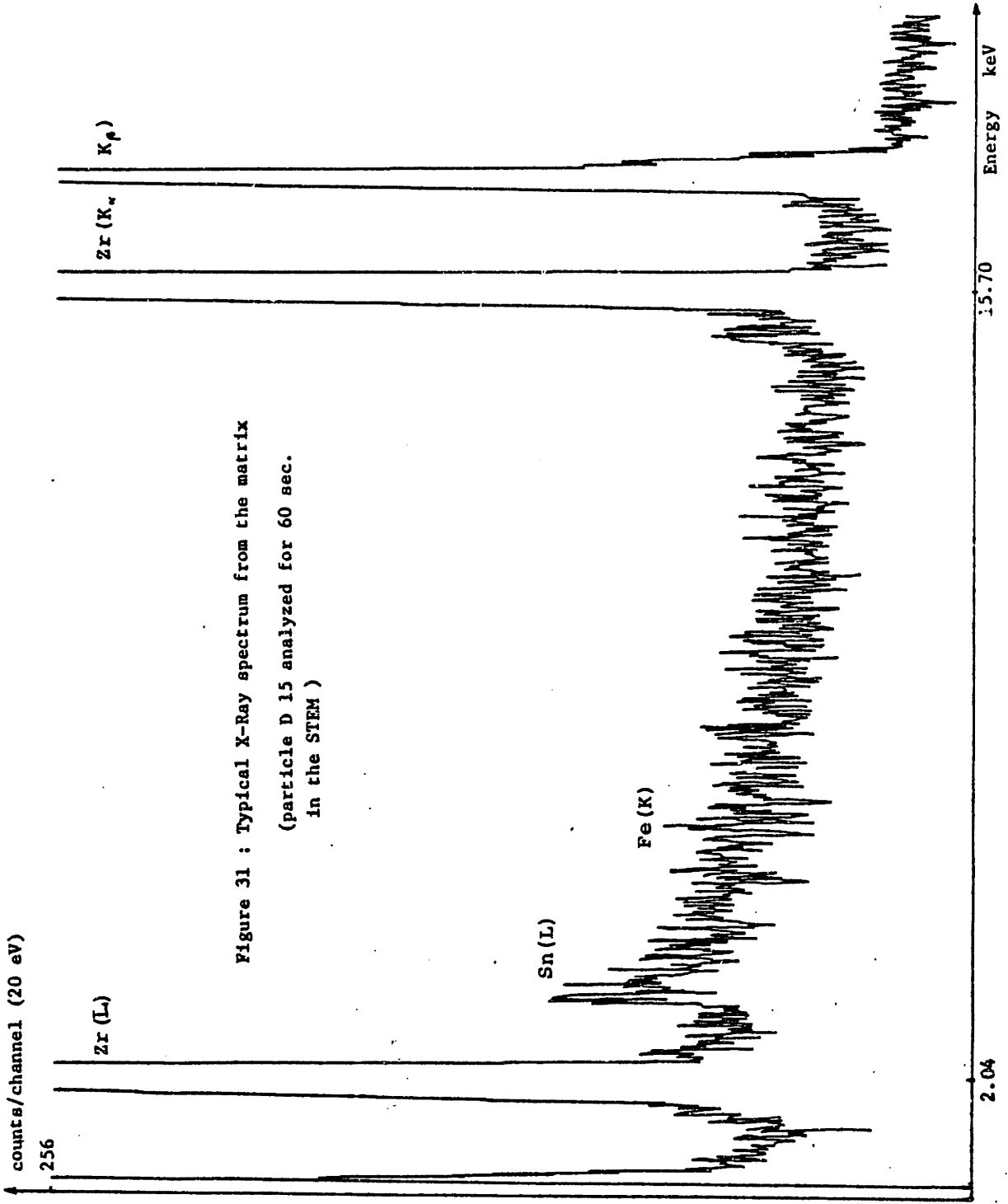


Figure 31 : Typical X-Ray spectrum from the matrix
 (particle D 15 analyzed for 60 sec.
 in the STEM)

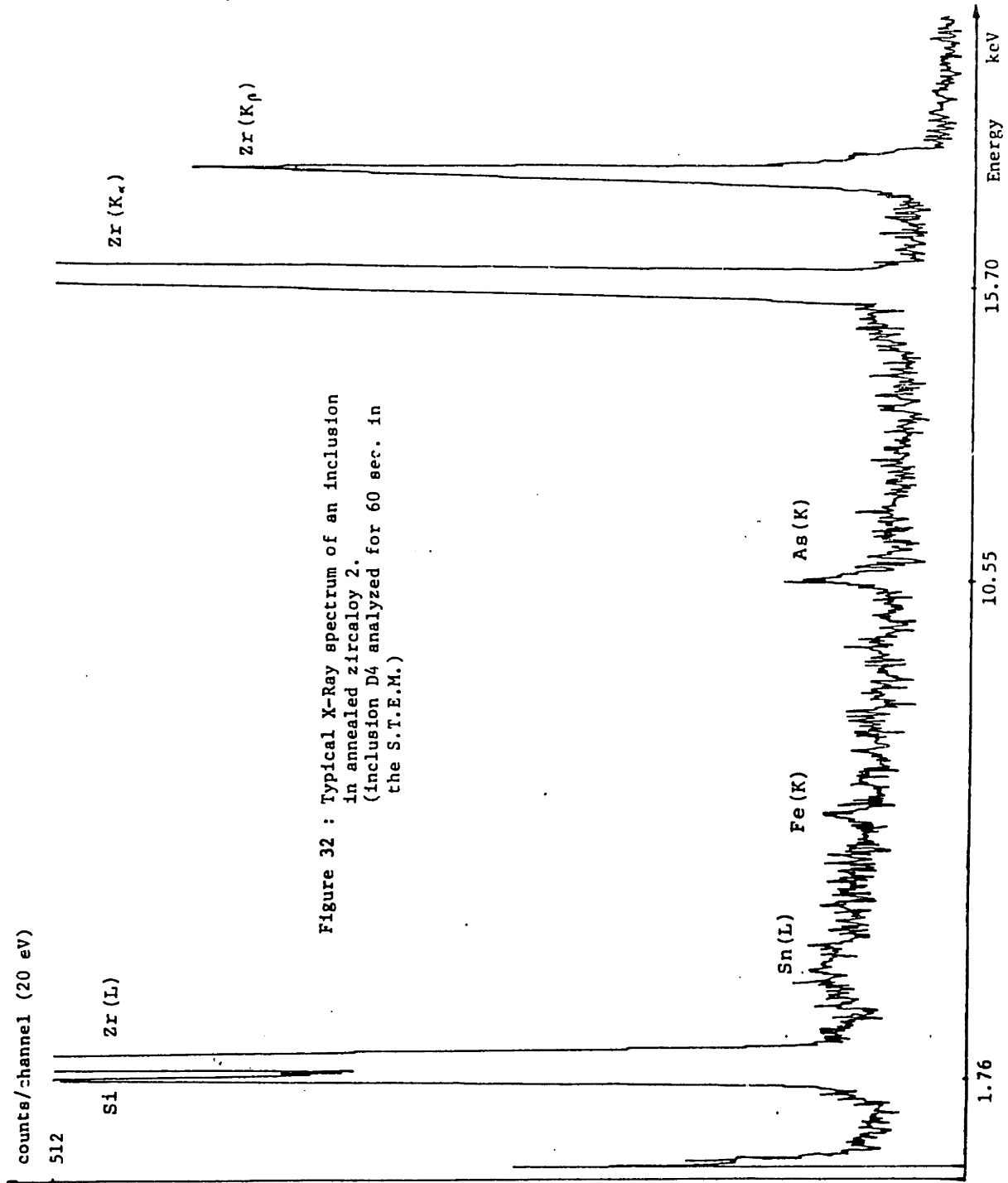


Figure 32 : Typical X-Ray spectrum of an inclusion in annealed zircaloy 2. (inclusion D4 analyzed for 60 sec. in the S.T.E.M.)

analyzed intermetallic particles extracted were of the Zr-Cr-Fe type with a Fe/Cr ratio of 45/55 and a constant Zr index of 0.2 (Figure 30).

Tin was not detectable in any of the particles. However, a low signal was obtained for the energy of tin when the matrix was analyzed. A typical matrix X-Ray spectrum is given in Figure 31. There was no evidence of any segregation of tin in any analyzed compound or boundary. The inclusions described in Part IV.3d. were also analyzed and confirmed the presence of silicon suspected from electron diffraction analysis. In addition to silicon, weak peaks corresponding to tin, iron and arsenic (or lead) were observed. Such a spectrum is given in Figure 32.

V. DISCUSSION

Particle distribution

The mean spacing between particles could not be determined using the TEM because the thickness of the foil was not constant. In addition, many particles were partially or completely etched out. In the SEM, as the X-Ray analysis indicated, only chromium iron rich particles were remaining in relief above the surface of the matrix. The nickel rich particles were etched out. The fraction of pits corresponding to particles (chromium or nickel) cannot be determined and the mean number of particles per unit area could not be determined. It is likely that a particular chemical attack of the surface will etch preferentially the matrix and show the two types of particles allowing a better measurement of the particle density which is related to the volume fraction of second phase.

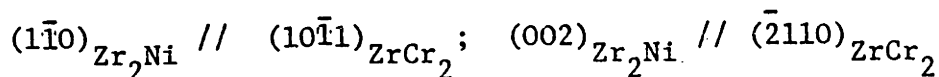
Clusters of Zr_2Ni and $ZrCr_2$ phases

Clusters of particles have not been described in the literature. They are present in annealed zircaloy and always exhibit the same constitution: a central nickel particle with one or two attached particles on opposite sides. Two hypotheses can be considered at first to interpret the formation of these clusters: (a) a compound containing iron, nickel and chromium, stable at higher temperature decomposes during annealing or cooling and transforms to the clusters observed. (b) The chromium iron phase nucleates on the nickel iron phase.

If the first hypothesis is correct, clusters of the unknown "mother" phase should be present in the cold worked, stress relieved material.

If the iron chromium nickel compound has a defined composition, the ratio of the volumes of each type of phase in a cluster should be constant and this has not been observed. The "reordering" of a single compound is more likely to occur on a finer scale than $0.2 \mu\text{m}$.

There are several arguments in favor of the second hypothesis. The germinating chromium phase can grow more easily on a nickel particle (a) because some interfacial energy is available and we know by electron diffraction that the lattices of the two compounds have similarities. A simple crystallographic relationship between the nickel rich and the chromium rich particle is concluded from Figure 20 to be:



(b) because the chromium rich particles contain little nickel and there is a depletion of the nickel content of the matrix near the particle-matrix interface. One should note however that the maximum solubility of nickel in the chromium rich particles and in the matrix are not known and that there is also a depletion of iron near the interface.

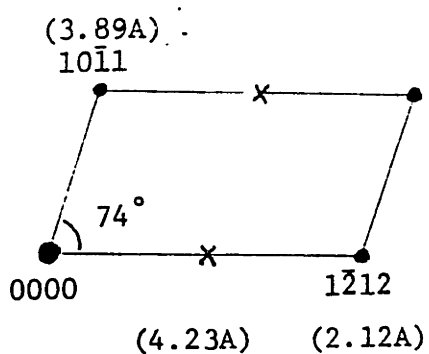
This heterogeneous nucleation would indicate that the nickel rich particles are precipitated first. This cannot be concluded from the binary systems (which give temperatures of 845°C and 835°C for the precipitation of Zr_2Ni and ZrCr_2 respectively), because iron is present in large amount in the identified phases.

Crystallographic structure of the particles

The crystallographic structures of the two types of intermetallics are very close to the structure of Zr_2Ni and ZrCr_2 . Within the accuracy of the measurements (1%) the lattice spacings of Zr_2Ni and ZrCr_2 can be

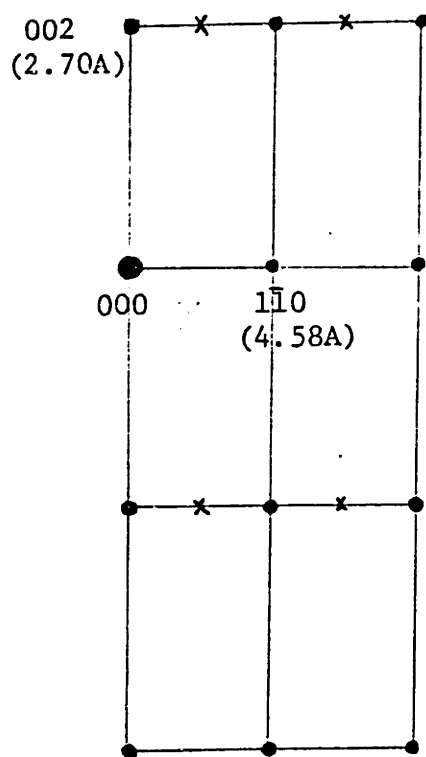
used to index the diffraction patterns. Several electron diffraction images of ZrCr_2 are very close to the patterns of Zr_2Ni . e.g. $(111)_{\text{Zr}_2\text{Ni}}$ and $(1\bar{2}13)_{\text{ZrCr}_2}$ or $(001)_{\text{Zr}_2\text{Ni}}$ and $(1\bar{2}10)_{\text{ZrCr}_2}$. In general several patterns of the same particle are necessary to identify it as chromium rich or nickel rich (unless patterns such as $(0001)_{\text{ZrCr}_2}$ or (001) are obtained). The ZrCr_2 type compound shows a band structure that has been described as a f.c.c.- h.c.p. packing by Versaci and Ipohorski (26) with $[110]_{\text{fcc}}$ parallel to $[1210]_{\text{hcp}}$ and $[111]_{\text{fcc}}$ parallel to $[0001]_{\text{hcp}}$. No diffraction pattern corresponding to the cubic structure has been obtained. The platelet structure of the particle was responsible for streaks in the $[0001]$ direction. As ZrCr_2 has a hexagonal structure, it is likely that the platelets are twins or stacking faults. These were present only on large precipitates and could be produced by deformation on cooling.

A second possible explanation is the formation of hexagonal ZrCr_2 from fcc ZrCr_2 but there is no evidence of presence of fcc ZrCr_2 in zircaloy 2. Some electron diffraction images corresponding to high index poles showed variations in intensity related to variations of structure factor. The structure factor has not been calculated for the different reflections of ZrCr_2 or Zr_2Ni but since Fe and Ni and Cr have close atomic scattering factors, because their atomic mass is similar, while the Zr atom is much heavier, it is likely that such variations in spot intensity are present in ZrCr_2 and Zr_2Ni . For both intermetallic particles, in particular electron diffraction patterns, additional spots were observed, corresponding to ordering of the structure on a larger scale than the ZrCr_2 or Zr_2Ni structure. Vitikainen (23) reports the



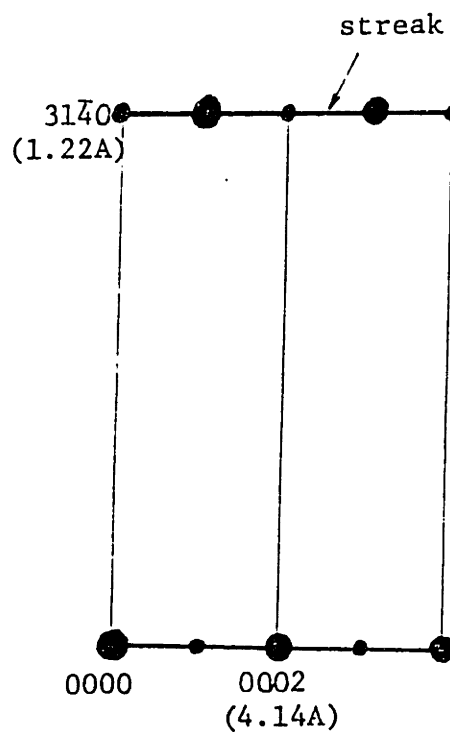
(5416) $ZrCr_2$ type

x: additional spot



(110) Zr_2Ni type

x: additional spot



(7520) $ZrCr_2$ type

● strong spot
● weak spot

Figure 33 : Electron diffraction patterns of the intermetallic particles presenting surstructure reflexions and stucture factor influence.

(101) reflection as missing in the (010) pole but visible in the (111) pole. Examples of these two phenomena are given in Figure 33.

Chemical Composition of the Particles

According to the electron diffraction data, the structure of the two compounds is very close to $ZrCr_2$ and Zr_2Ni so that it is probable that iron is substituting for Cr or Ni, respectively. The sizes of Cr, Ni and Fe atoms are comparable. However, Cr could not be detected in the Zr_2Ni type of particles, neither could Ni be found in the $ZrCr_2$ type. As it was shown by the statistics on the composition of particles (Figures 27, 29 and 30), if there is substitution, the amount of element substituted is constant for each type of particle. It can be dependent on heat treatment. Zircaloy 2 contains 0.05 wt% Ni, 0.1 wt% Cr and 0.15 wt% Fe. The atomic mass of Fe, Ni and Cr are close and the concentrations verify $[Cr] = 2[Ni]$ and $[Fe] = [Cr] + [Ni]$. In the $ZrCr_2$ type of particles $[Cr] = [Fe]$ and in the Zr_2Ni type $[Ni] = [Fe]$ as a first approximation. As the solubility of Ni and Cr is very small in α zirconium, one can expect a precipitation of phases depleting nearly completely the matrix in Fe, Ni and Cr. If the particles are well defined compounds, one can expect other phases containing Fe, Ni or Cr to precipitate after long annealing times in most cases. As it has been shown recently by J.M. Grange (31) in zircaloy 4 the formation of iron rich phases (ζ and Zr_4Fe) can occur with adequate heat treatments.

Previous investigators found it difficult to determine the chemical composition of particles in zircaloy 2 because they are of submicron size and a conventional microprobe with a volume resolution of $1 \mu m^3$ is not accurate enough. Östberg (22) averaged the particles and analyzed only

particles larger than $1\mu\text{m}$. Vitikainen (23) using a Jeol 200 kV, TEM with scanning ability did not obtain accurate results.

A dedicated STEM provides a strong X-Ray signal from very small volumes. To be quantitative, the STEM needs to be calibrated with known compounds and such standards were not available for this work. If the intensity of the X-Ray signal was consistent with the number of atoms of the considered chemical element, a Zr index of 0.33 for the ZrCr_2 type and of 0.67 for the Zr_2Ni type should be expected. The result of the ZrCr_2 type of particles extracted on carbon replica is 0.2. The low values of the Zr index for the Zr_2Ni type are around 0.55. When a particle is analyzed in situ, part of the signal comes from the matrix and the Zr index presents a large scatter band. Experimental and theoretical results of Zr indices are in good agreement. The smaller experimental value of the Zr index results probably from the fluorescence of the K X-Ray energy level of Fe, Cr and Ni by the high energy. X-Rays of zirconium (15.4 keV) and also from a peak shape difference, the window width being 270 eV for all the elements. The Ni and Fe peaks in the Zr_2Ni type and the Cr and Fe peaks in the ZrCr_2 type of particles are of comparable size and of close energy. We will propose a chemical composition of $\text{Zr}_2\text{Ni}_{0.4}\text{Fe}_{0.6}$ for the Zr_2Ni type of particles and $\text{ZrCr}_{1.1}\text{Fe}_{0.9}$ for the ZrCr_2 type of particles. This result is quite different from the analysis of Vander Sande and Bement (15) of the ZrCr_2 type of particles in zircaloy 4 where a $\text{Zr}_x\text{Fe}_5\text{Cr}_2$ composition is suggested.

Tin in Zircaloy 2

According to the phase diagrams, in the binary alloy zirconium 1.5 wt% tin, precipitation occurs below a temperature close to 500°C .

However, at temperatures below 500°C, the kinetics of precipitation can be very slow. In the annealed and in the cold worked stress relieved zircaloy 2 considered here, tin could be detected only in the matrix. There was no concentration of tin in other intermetallic particles or at interfaces. If tin rich particles were present, they were not observed in bright field. If they are small enough to be confused with the graininess of the image due to oxidation, they are probably coherent with the matrix and might give rise to additional spots in electron diffraction. We did not find these features and we will conclude that tin is in solid solution in the as received material.

Inclusions

Only one kind of inclusion was observed in zircaloy 2. The electron diffraction as well as the chemical analysis led to the identification of the Zr_3Si type of silicide. Some diffraction patterns are given in Appendix C. The chemical analysis in the STEM showed the presence of other elements in these inclusions. For example, lead or arsenic. The distinction between lead and arsenic could not be made because the signal is weak and mainly one line is observed. The energy resolution and the accuracy of calibration of the energy dispersive X-Ray analyser were insufficient. The arsenic content of zircaloy 2 is not usually determined. No recorded compound fitted all these data. No carbide or other inclusion than the ones containing silicon were observed. Zirconium carbides of ZrC type can be easily identified in electron diffraction as they are of cubic structure with $a_0 = 4.7\overset{\circ}{\text{Å}}$.

VI. CONCLUSIONS AND SUGGESTIONS FOR FURTHER WORK

Conclusions:

Zircaloy 2 in the annealed and in the cold worked, stress relieved condition was studied by SEM, TEM and STEM. The structures and the chemical composition of the different second phase particles were determined by electron diffraction in the TEM and by energy dispersive X-Ray microanalysis in the STEM. The alloying elements were found to be partitioned as follows:

1. Nickel is present in a tetragonal phase with $a_0 = 6.5 \text{ \AA}$, $c_0 = 5.3 \text{ \AA}$ similar to Zr_2Ni containing iron in partial substitution for nickel. The composition of this phase is $\text{Zr}_2\text{Ni}_{0.4}\text{Fe}_{0.6}$.
2. Chromium is present in a hexagonal phase with $a_0 = 5.1 \text{ \AA}$, $c_0 = 8.3 \text{ \AA}$, similar to ZrCr_2 , containing iron in partial substitution for chromium. The chemical composition of this phase is $\text{ZrCr}_{1.1}\text{Fe}_{0.9}$.
3. Iron is partitioned in the two phases described above and very little remains in solid solution in the matrix.
4. Tin is in solid solution in the textured hexagonal matrix of α zirconium.

These intermetallic phases are uniformly distributed within the matrix with an average size of 0.3 \mu m . In TEM and STEM, individual precipitates as well as heterogeneous clusters of 2 to 5 particles were observed. The second phase particles were also studied with the SEM after chemical etching. The nickel rich particles were etched out. Large inclusions (1 \mu m) having the structure of Zr_3Si were identified.

In the cold worked, stress relieved condition, the material is partially recrystallized with elongated grains and a dense network of dislocations.

Suggestion for further work:

The following topics are suggested for further work:

1. Determination of the volume fraction and mean interparticle spacing in the annealed condition.
2. Quantification of the STEM X-Ray energy dispersive analysis results with CrNi-Fe-Zr standards.
3. Analysis of the size and distribution of second phase particles in the cold worked, stress relieved material.
4. Analysis of the microstructure after β processing.
5. Investigation of further precipitation and cavitation after creep deformation.
6. Correlation between corrosion rate and corrosion initiation sites and second phase particles.
7. Stability of the solid solution of tin.

APPENDIX ACRYSTALLOGRAPHY OF HEXAGONAL MATERIALS

The crystallography of hexagonal close packed metals has been reviewed recently by P.G. Partridge (32). It is not the aim of this appendix to describe the hexagonal lattice but the reader will find here some tables and basic information that were useful for the present study.

The most important directions and planes are given in Figure A1. The four Miller-Bravais index notation has been used. This notation conserves a similarity between equivalent directions or planes and is used in the stereographic projection. The reader not familiar with the stereographic projection is referred to Cullity (33). For hexagonal materials, on a (0001) standard projection, the position of the poles corresponding to pyramidal planes depends on the c/a ratio of the material. For precise work, a stereographic projection corresponding to the specific material of interest is necessary. The angles between the most important planes are given for zirconium in Table A1.

In order to facilitate one's construction of poles in the stereographic projection as well as to find a pole quickly, the following set of coordinates are proposed: As $h+k+i=0$, $(hkil)$ being the Miller-Bravais indices, two integers among $\{h,k,i\}$ are of the same sign. (Zero can be considered as positive or negative indifferently.) In the following, we will consider h and k both positive as an example. We will choose the smaller of h/k and k/h as a first coordinate x . (For instance, $x=h/k$ if $h < k$). This coordinate is always between 0 and 1. The choice of these two indices indicates in which 1/12th of the standard (0001) stereographic projection the pole of indices $(hkil)$ lies. To know how far from (0001)

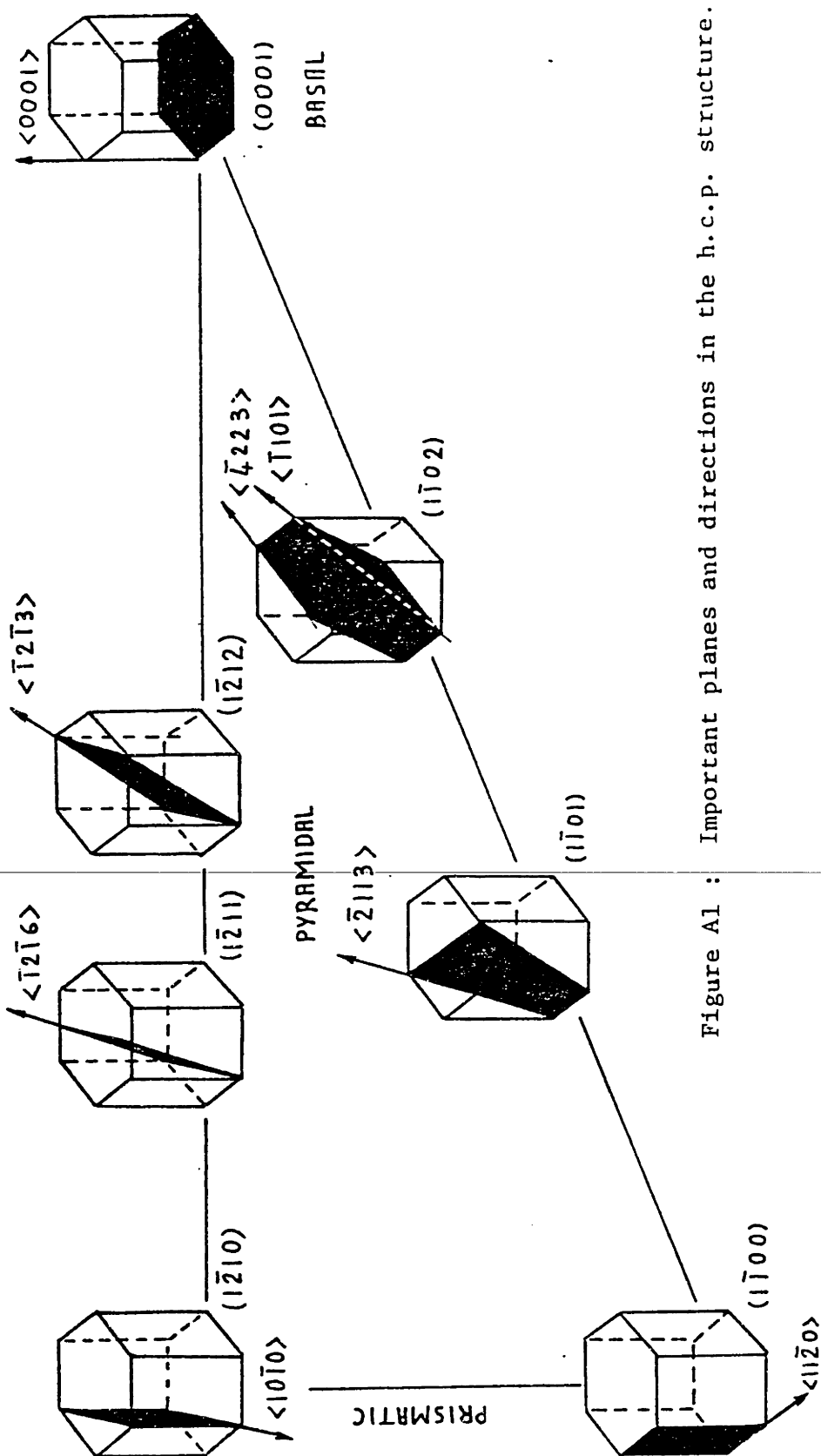


Figure A1 : Important planes and directions in the h.c.p. structure.

$\begin{matrix} hkl \\ h'k'l' \end{matrix}$	$\bar{1}\bar{2}10$	$0\bar{1}10$	0001	$\bar{1}\bar{2}13$	$2\bar{4}23$	$0\bar{1}11$	$\bar{1}\bar{2}16$	$\bar{1}\bar{2}11$	$0\bar{1}12$	$\bar{1}\bar{5}43$	$2\bar{7}53$	$\bar{1}\bar{2}19$
$\bar{1}\bar{2}10$	0	30	90	43.3	25.2	40.5	62.0	17.4	54.1	27.1	20.1	70.5
$0\bar{1}10$		0	90	50.9	38.4	28.5	66.0	34.3	47.4	22.3	21.6	73.2
0001			0	46.7	64.8	61.5	28.0	72.6	42.6	70.4	75.4	19.5
$\bar{1}\bar{2}13$				0	18.1	28.2	18.8	25.9	21.3	28.6	31.0	27.2
$2\bar{4}23$					0	26.9	36.8	7.8	32.4	18.5	16.8	45.3
$0\bar{1}11$						0	38.9	29.7	18.9	13.4	20.4	45.2
$\bar{1}\bar{2}16$							0	44.6	22.3	4.1	48.4	8.5
$\bar{1}\bar{2}11$								0	38.8	18.2	13.6	53.1
$0\bar{1}12$									0	29.2	35.4	27.2
$\bar{1}\bar{5}43$										0	7.0	52.2
$2\bar{7}53$											0	56.5

Table A1 :

Angles between $(hki\ell)$ and $(h'k'i'\ell')$ planes in hexagonal Zr

$$\cos((hki\ell), (h'k'i'\ell')) = \frac{h h' + k k' + \frac{1}{2}(h k' + k h') + \frac{3}{4} \frac{a^2}{c^2} \ell \ell'}{\sqrt{h^2 + k^2 + h k + \frac{3}{4} \frac{a^2}{c^2} \ell^2} \sqrt{h'^2 + k'^2 + h' k' + \frac{3}{4} \frac{a^2}{c^2} \ell'^2}}$$

with $c/a = 1.593$

the (hkil) plane is, one needs a second coordinate and we will choose $y = 1/u$ where u is the third index remaining after the choice of the two others to define x . In our example $y = 1/i$.

Figure A2 shows the standard (0001) stereographic projection for Zr_{α} . The sign of the different indices as well as the net of coordinates (x,y) for zirconium are indicated. The data to construct such a net is given in Figure A3 and Table A2.

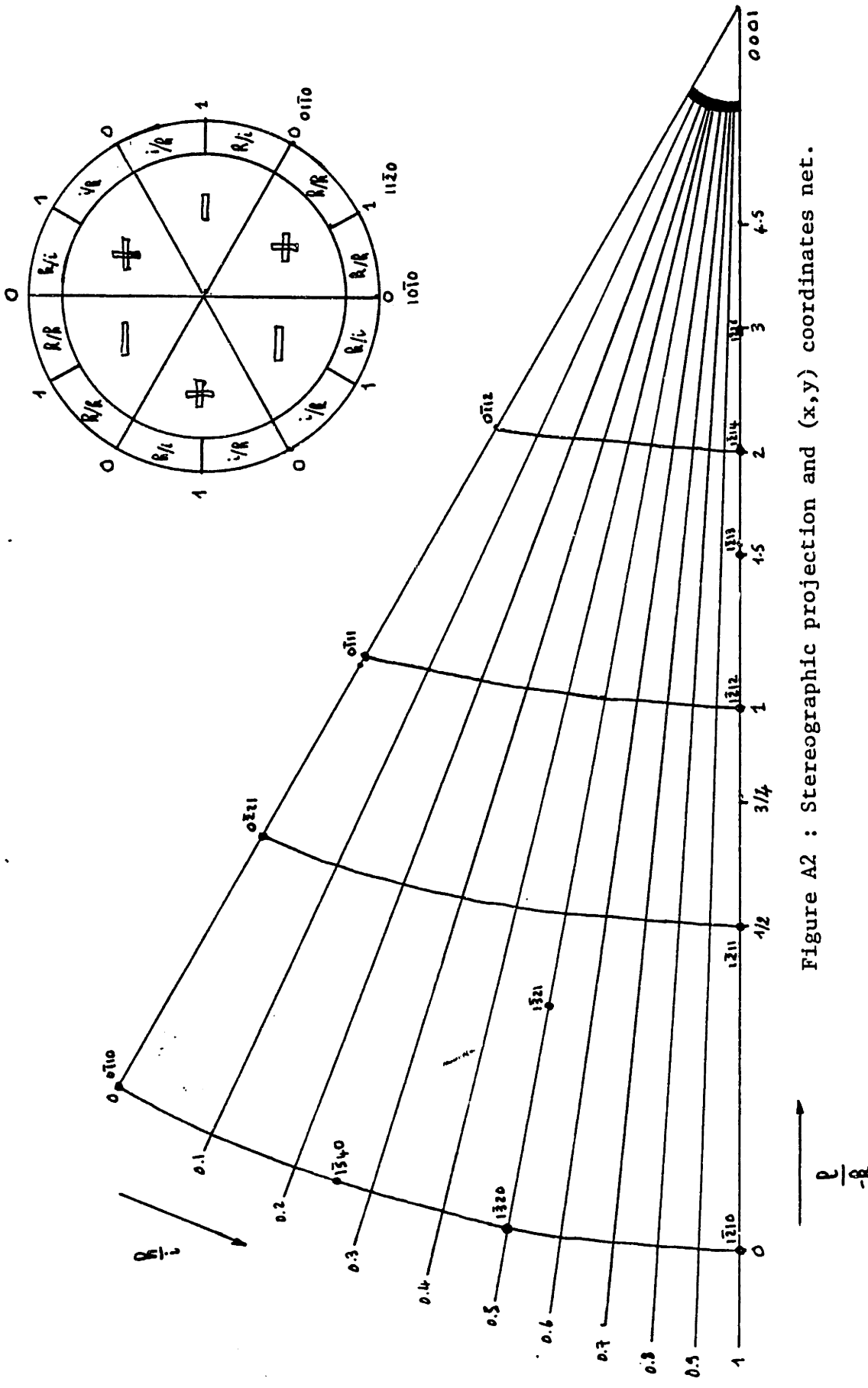
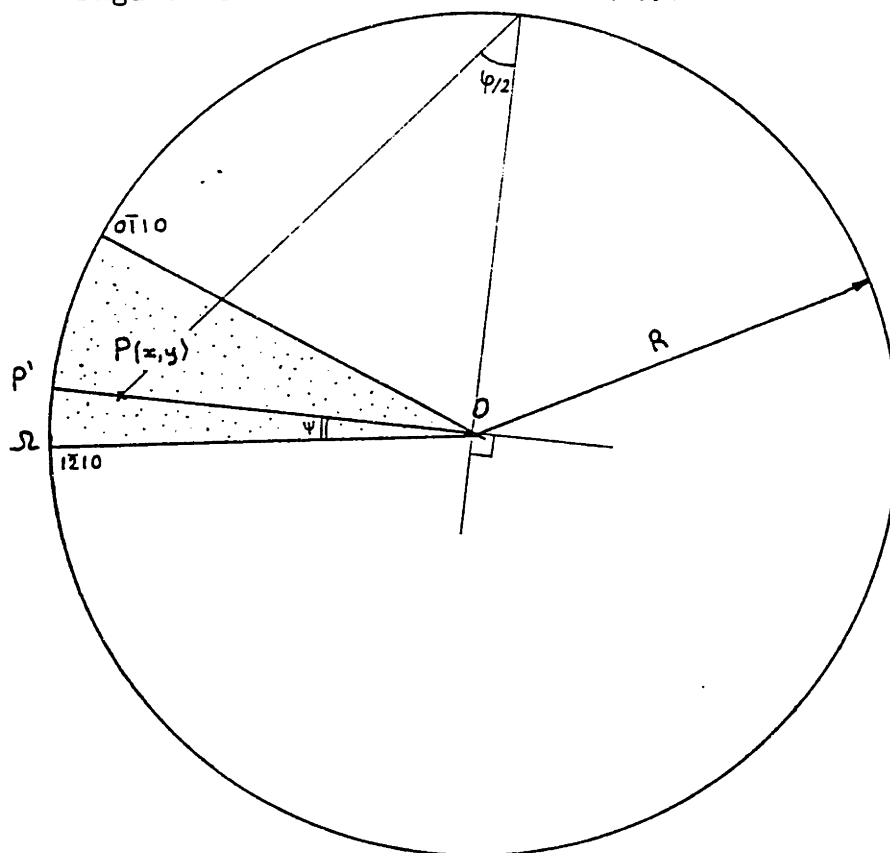


Figure A2 : Stereographic projection and (x,y) coordinates net.

Figure A3 : Definition of the (x,y) coordinates system.



P is defined by the coordinates (x,y) or by the Miller indices $h k i l$

In the case of the drawing $h > 0$ $k < 0$ $i > 0$ $l > 0$
 $h \leq i$

$$x = \frac{h}{i} \quad y = -\frac{l}{k}$$

$\hat{OP} = \varphi$ and the length of OP is $R \operatorname{tg}(\varphi/2)$

$$\cos \varphi = \frac{1}{\beta}$$

$$\operatorname{tg} \varphi = \frac{c}{a} \frac{\beta}{y}$$

with $\beta = \frac{2}{\sqrt{3}} \frac{\sqrt{1+x+x^2}}{1+x}$

and $\frac{c}{a} = 1.593$ for Zr_{α}

Table A2 : Computed parameters for the construction of the (x,y) net
[of coordinates.]

		$t_g [\varphi(x, y) / 2]^*$				
x	$\psi(x)^\circ$	y = .5	y = 1	y = 2	y = 3	y = 4
0	30.	0.764	0.594	0.390	0.282	0.219
.1	25.3	0.756	0.582	0.378	0.272	0.210
.2	21.1	0.749	0.573	0.369	0.265	0.204
.3	17.3	0.744	0.566	0.362	0.259	0.200
.4	13.9	0.741	0.562	0.358	0.256	0.197
.5	10.9	0.738	0.558	0.354	0.253	0.195
.6	8.2	0.736	0.556	0.352	0.251	0.194
.7	5.8	0.735	0.554	0.351	0.250	0.193
.8	3.7	0.735	0.553	0.350	0.249	0.192
.9	1.7	0.734	0.553	0.350	0.249	0.192
1	0	0.734	0.553	0.349	0.249	0.192

* given for $c/a = 1.593$

y	$t_g [\varphi(x, y) / 2]^*$	
	x = 0	x = 1
0.25	0.873	0.855
0.33	0.835	0.812
0.67	0.701	0.665
0.75	0.672	0.634
1.33	0.510	0.467
1.5	0.475	0.432
1.67	0.443	0.401

APPENDIX BELECTRON DIFFRACTION OF ZIRCALOY 2

In electron diffraction, two main features are to be considered: (a) the spot patterns and (b) the Kikuchi lines. For electron diffraction theory, the reader is referred to Hirsh (34) and for Kikuchi lines to G. Thomas (35). One should consider the spot as part of the "reciprocal lattice" (Figure B1). Some reflections are not observed in high order index poles but occur usually by double diffraction in poles such as $(2\bar{1}\bar{1}0)$. Twelve of the most densely populated reciprocal lattice planes are presented in Figure B2. They can be partitioned into three categories as shown in Table B1. The repartition and the angular relationship between these 12 poles is given in Figure B3.

When the crystal is thick enough, sets of lines can often be observed superimposed on the diffraction patterns. These lines are very useful to determine precisely the direction of the electron beam with respect to the foil and the exact diffraction conditions. A band structure relating the spot patterns is often visible and characteristic of the crystal. Maps and composite pictures of this "Kikuchi network" can be found in the literature but they are very incomplete mainly in the spherical quadrangle $[(1\bar{2}13), (1\bar{2}10), (0\bar{1}110), 0\bar{1}12]$.

It has been very useful to consider the simple network of "thin diffuse bands" to quickly identify the position of the beam on the map. The map of Figure B4 is given by Loretto (36). The more detailed partial maps of Figures B5, B6 and B7 have been drawn using the composite maps B8 and B9. They should not be used for measurements of angles since a wide spherical triangle has been developed on a plane resulting in aberrations.

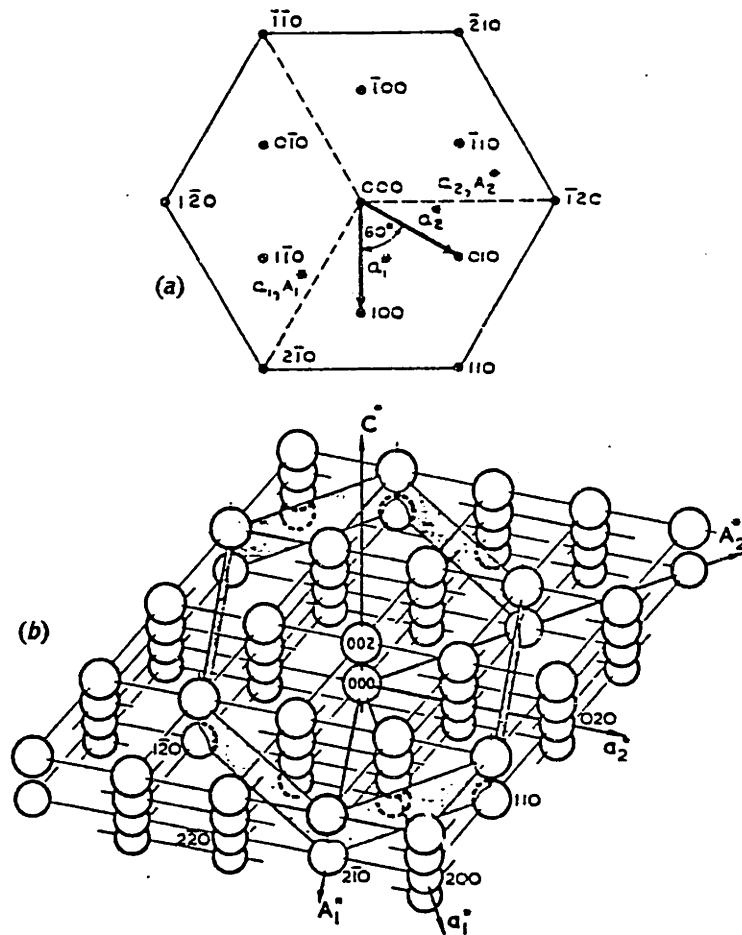
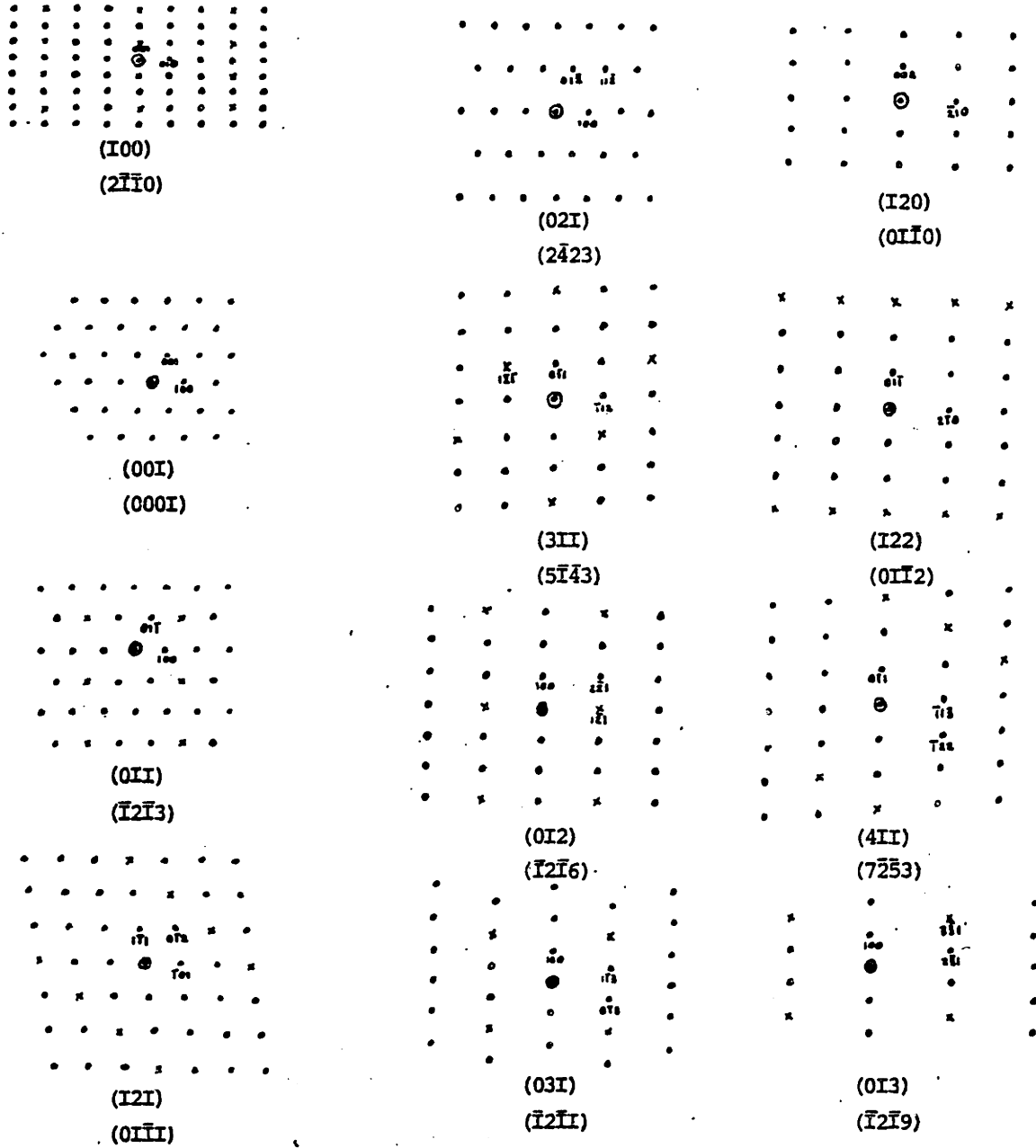


Figure B1 : Reciprocal lattice. *a* Section parallel to (001). *b* In 3 dimensions, with lattice points omitted where $(h + 2k)$ is a multiple of 3 and l is odd. a_1, a_2 direct lattice axes; a_1^*, a_2^* reciprocal lattice axes; A_1^*, A_2^* Miller-Bravais axes in reciprocal space.

Figure B2: Twelve of the most densely populated reciprocal lattice planes for the h.c.p. structure.



⊙ : 000

x: forbidden reflexion that can occur by double diffraction

Table B1: Twelve of the most densely populated reciprocal lattice planes for Zr_{α} .

$$a=3.232\text{\AA} \quad c=5.147\text{\AA} \quad c/a= 1.593$$

3 indices pole	4 indices pole	Type	R_2/R_1	φ°	$h_1k_1l_1$ $d_1 \text{ \AA}$	$h_2k_2l_2$ $d_2 \text{ \AA}$	ρ \AA^{-2}
0 $\bar{1}$ 0	1 $\bar{2}$ 10		1.839	90°	0001° 5.147	1010 2.799	14.4
0 $\bar{1}$ 2	1 $\bar{2}$ 16		1.815	90°	10 $\bar{1}$ 0 2.799	1 $\bar{2}$ 11° 1.542	4.32
1 $\bar{2}$ 0	0 $\bar{1}$ 10		1.593	90°	0002 2.574	2110 1.616	4.16
1 $\bar{2}$ 2	0 $\bar{1}$ 12		1.522	90°	0111 2.459	2110 1.616	3.97
001	0001		1.000	60°	1100 2.799	1010 2.799	9.05
0 $\bar{1}$ 1	1 $\bar{2}$ 13		1.138	64°	1010 2.799	0111 2.459	7.66
0 $\bar{2}$ 1	2 $\bar{4}$ 23		1.477	70°	1010 2.799	0112 1.894	5.64
0 $\bar{3}$ 1	1 $\bar{2}$ 11		1.914	75°	1010 2.799	0113 1.463	4.24
1 $\bar{2}$ 1	0 $\bar{1}$ 11		1.000	81°	1101 2.459	1011 2.459	6.12
1 $\bar{3}$ 1	1 $\bar{5}$ 43		1.298	87°	1011 2.459	1102 1.894	4.67
1 $\bar{4}$ 1	2 $\bar{7}$ 53		1.681	80°	1011 2.459	1103 1.463	3.65
0 $\bar{1}$ 3	1 $\bar{2}$ 19		2.701	79°	1010 2.799	1321 1.036	2.95

• : occurs by double diffraction

$$* : \rho = \frac{d_1 \cdot d_2}{\sin \phi}$$

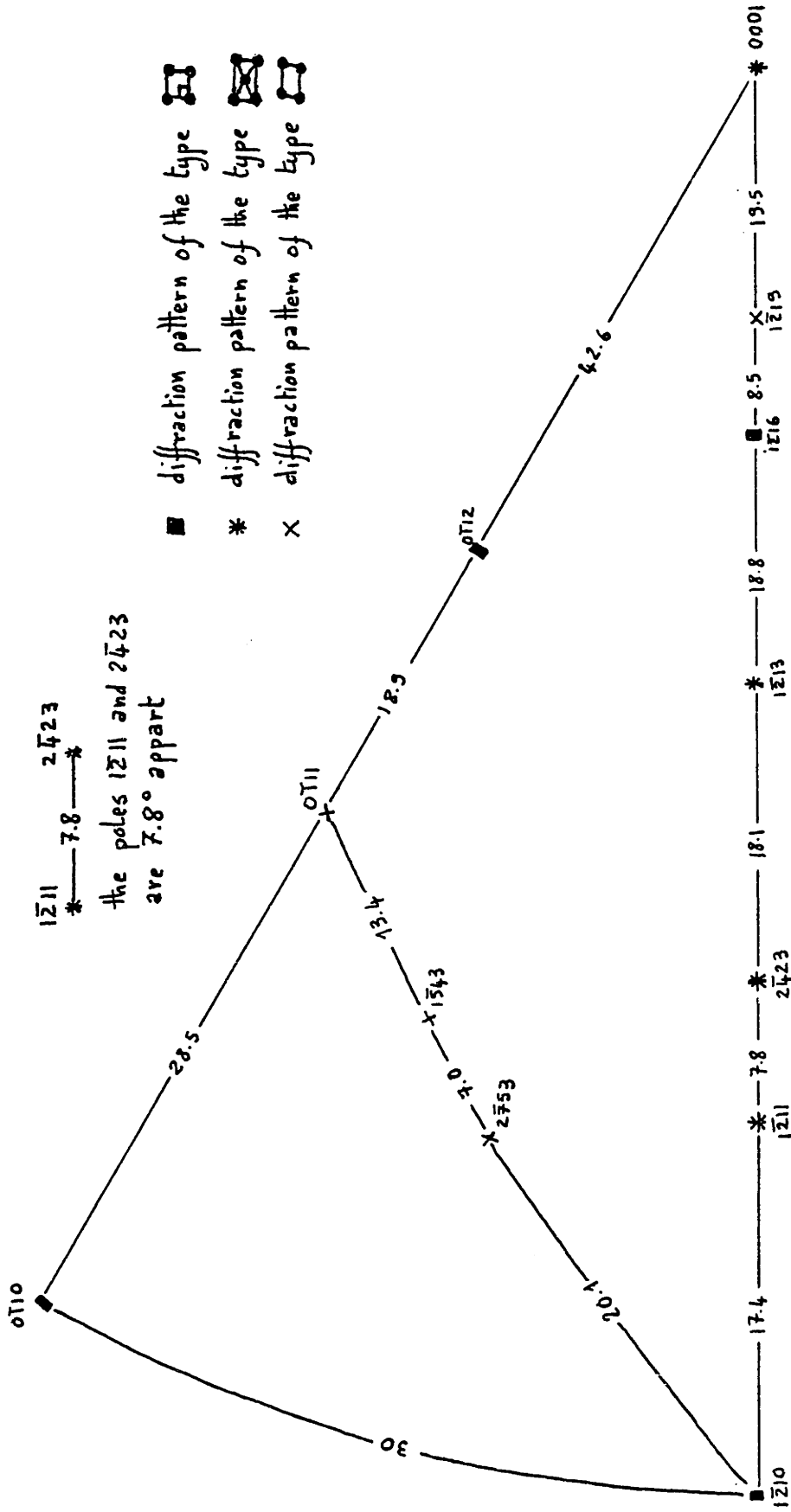
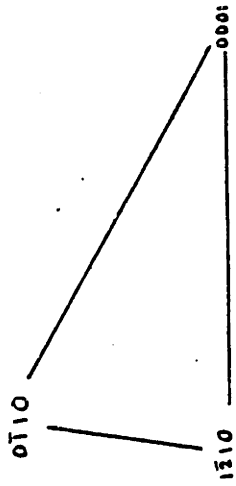


Figure B3 : Relation between electron diffraction patterns and (0001) stereographic projection.



thin diffuse band

Figure B4: General Kikuchi maps for c.p.h. crystals

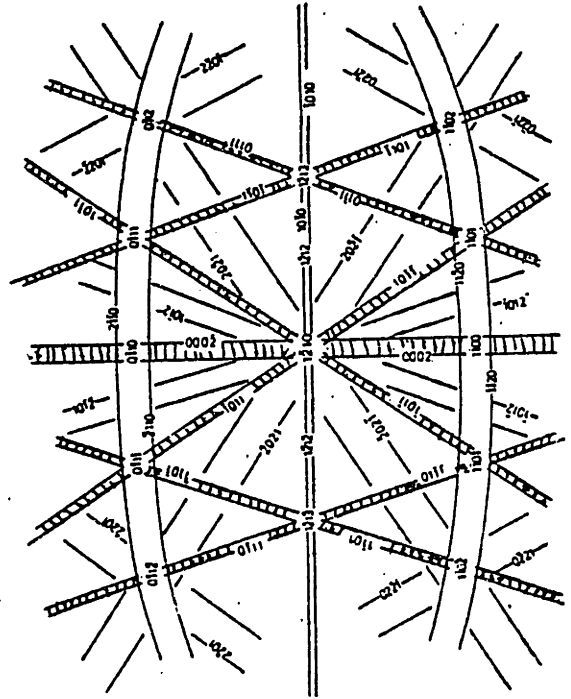
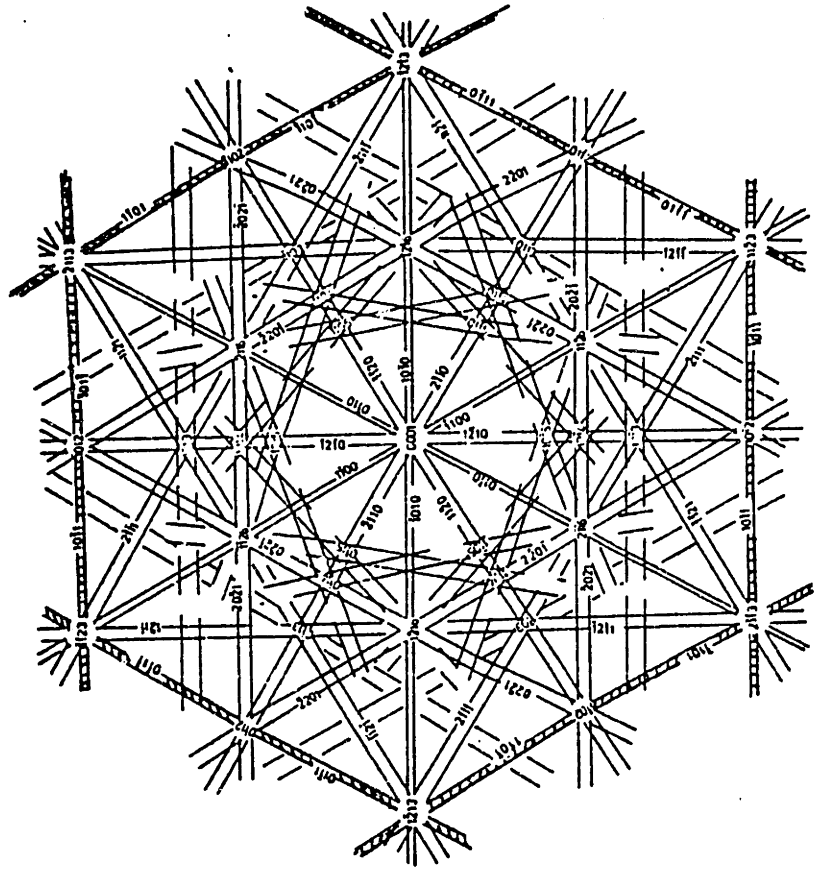
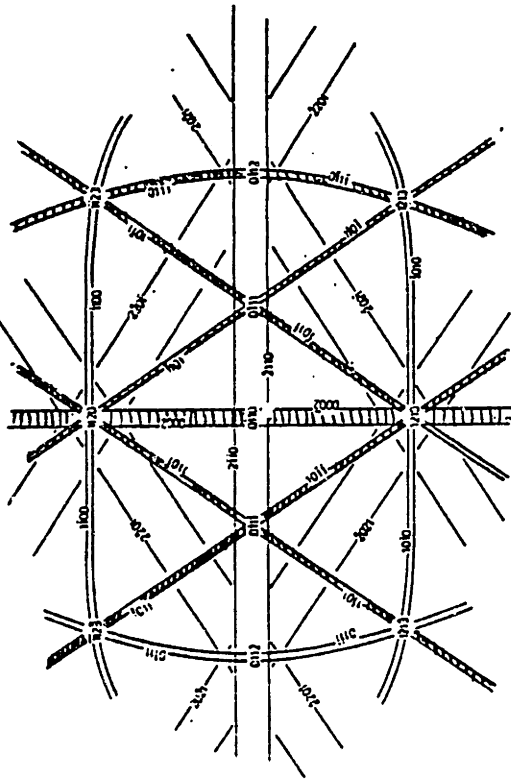


Figure B5 :
RIKUCHI MAP of zircaloy-2
part I

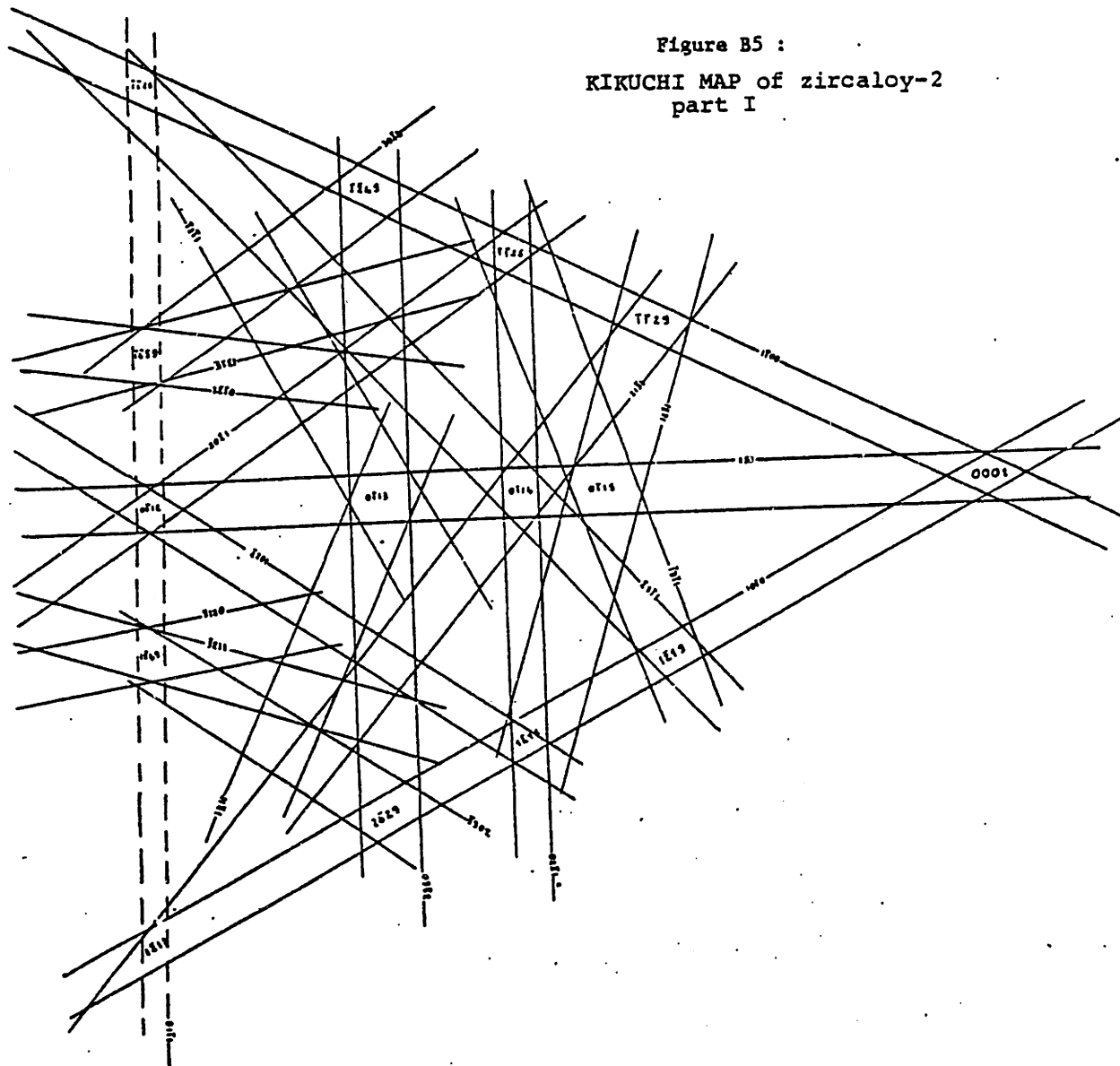
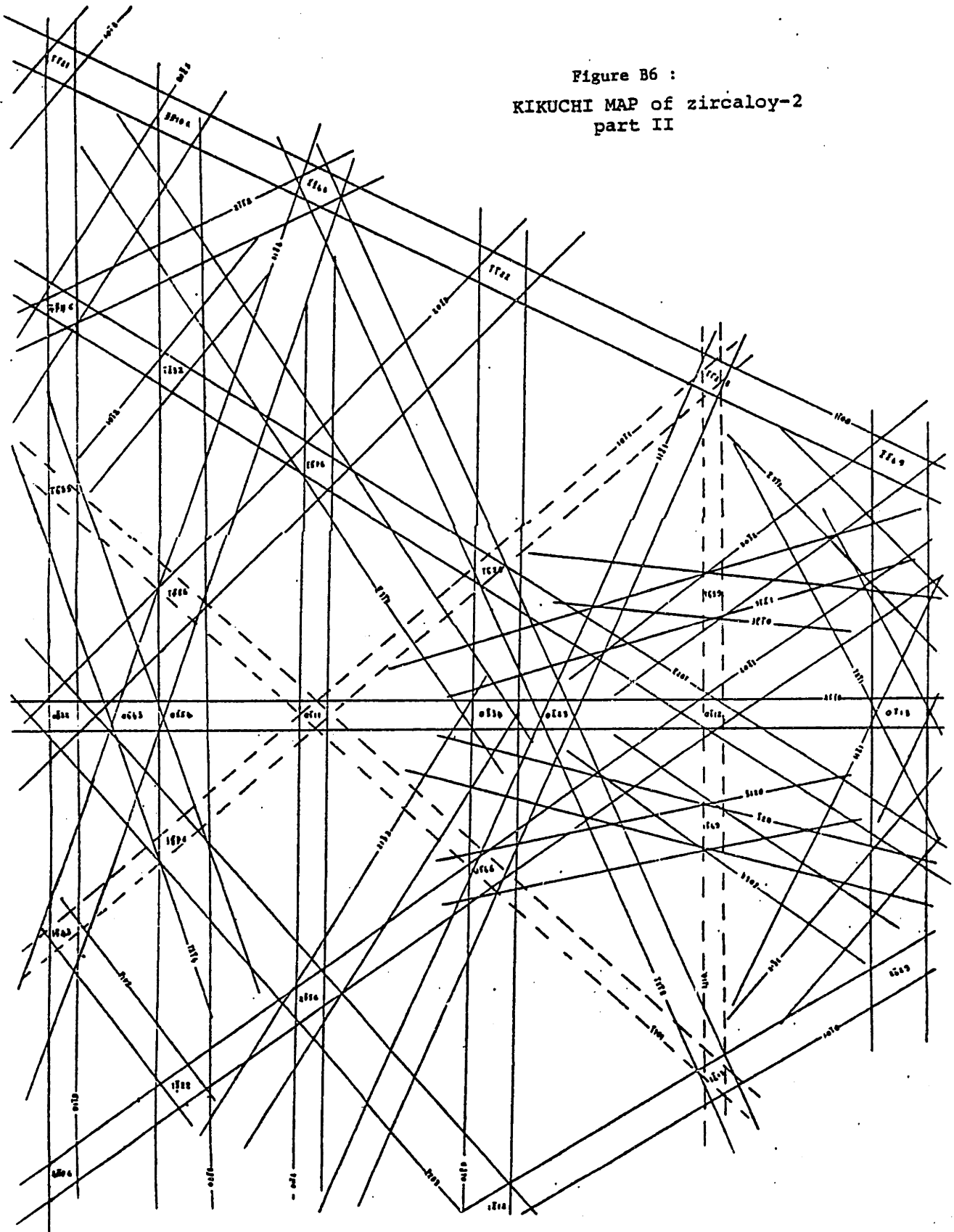


Figure B6 :
KIKUCHI MAP of zircaloy-2
part II



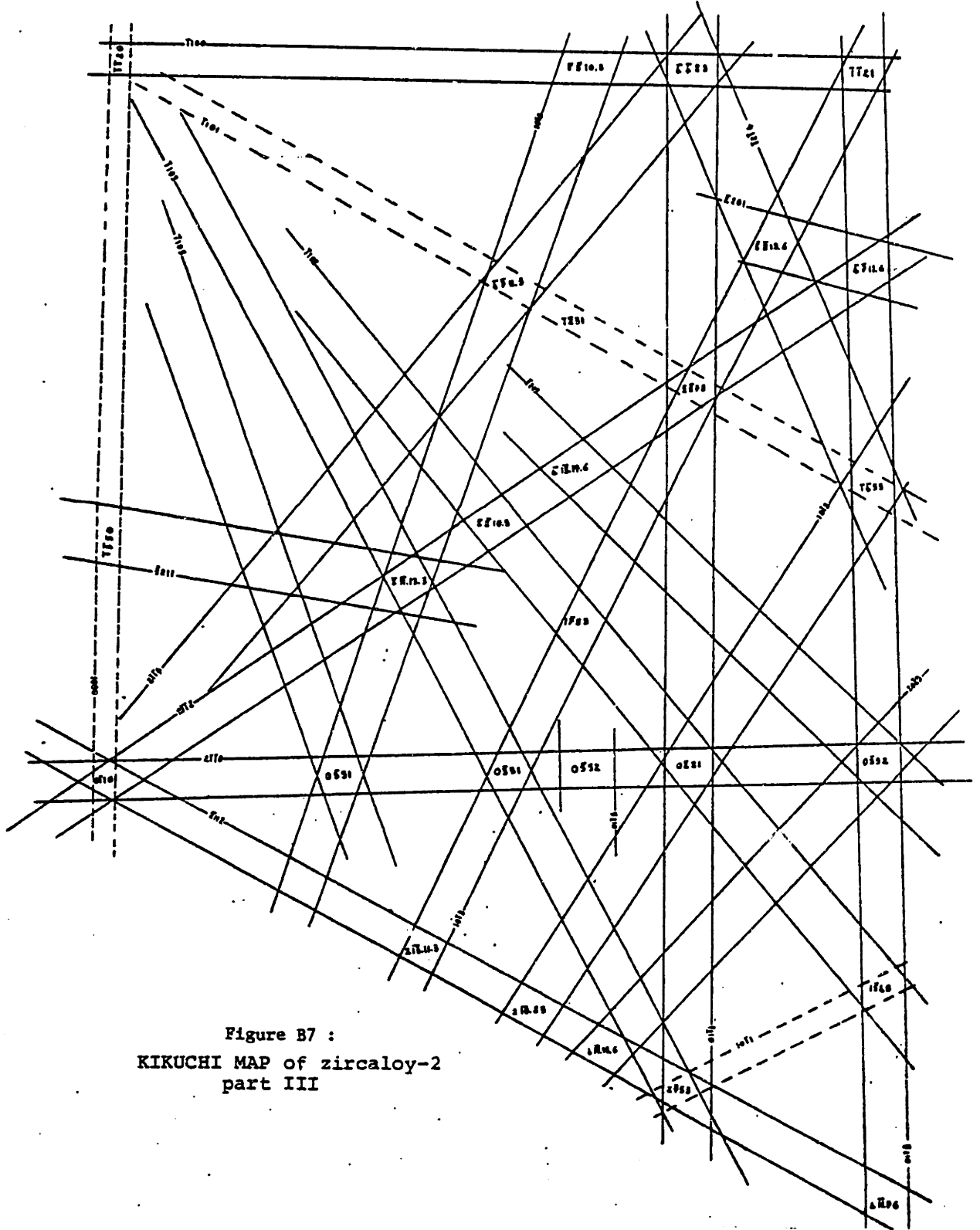


Figure B7 :
KIKUCHI MAP of zircaloy-2
part III



Figure B8 : Composite Kikuchi map for zircaloy 2. Part I.
(Reduction : 4X)

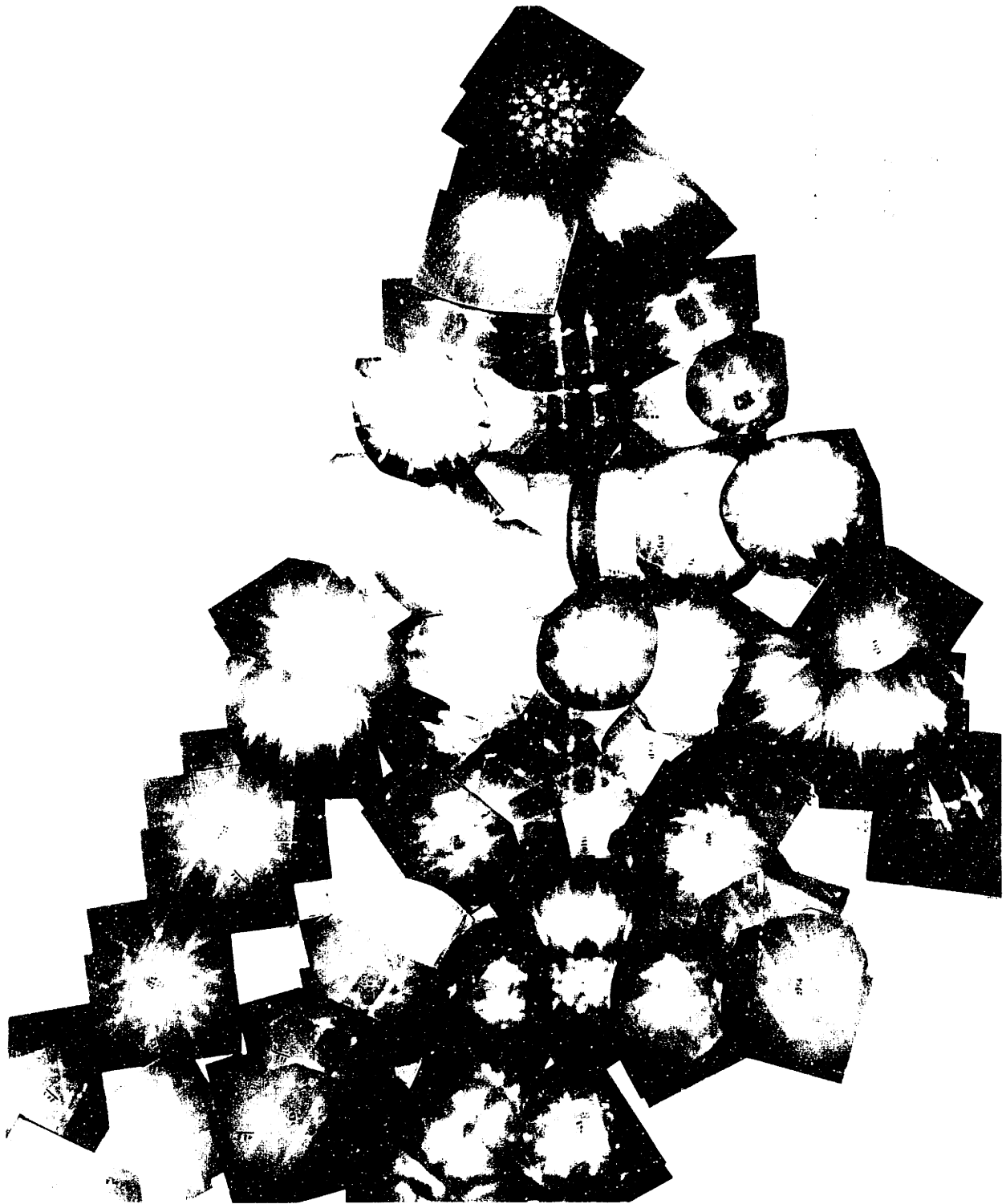


Figure 5: A photograph of a Christmas tree made of cutouts.
(Copyright © 2000)



Figure 9 : [Illegible text]



Figure 9 : A composite image of a photograph of a person's face, showing a high-contrast, black and white, and heavily distorted view. The image is composed of numerous overlapping, tilted rectangular fragments, suggesting a collage or a heavily processed image. The fragments contain faint, illegible markings or numbers, possibly related to the image's source or processing.

APPENDIX CSTRUCTURE OF ZIRCONIUM COMPOUNDS

The compounds of interest in this work are ZrCr_2 , Zr_2Ni and Zr_3Si . Tables useful for indexing diffraction patterns and comparisons between interplanar spacings are given in this appendix.

Table C1 - Calculated spacing of the (hkil) plane for hexagonal Zr and ZrCr_2 .

Table C2 - Twelve of the most densely populated reciprocal lattice plane for ZrCr_2 (Similar to Table B for Zr_α).

Table C3 - Calculated interplanar spacing of the (hkl) plane for tetragonal Zr_2Ni .

Table C4 - Calculated interplanar spacing of the (hkl) plane for tetragonal Zr_3Si .

Figure C1 - Some observed electron diffraction patterns corresponding to Zr_3Si .

Table C5 - Calculated interplanar spacing of the (hkl) plane for f.c.c. ZrCr_2

Table C1: Calculated^o interplanar spacing of the (hkil) planes
 for hexagonal Zr ($c=5.147\text{\AA}$, $a=3.232\text{\AA}$)^{*} and
 ZrCr₂ ($c=8.279\text{\AA}$, $a=5.079\text{\AA}$)^{**}

h k i l	Zr _α Å	ZrCr ₂ Å
10 $\bar{1}$ 0	2.799 x	4.399
0002	2.574 x	4.140 x
10 $\bar{1}$ 1	2.459 x	3.884
10 $\bar{1}$ 2	1.894 x	3.014
0003		2.760 x
11 $\bar{2}$ 0	1.616 x	2.540
10 $\bar{1}$ 3	1.463 x	2.338 x
20 $\bar{2}$ 0	1.399 x	2.199 x
11 $\bar{2}$ 2	1.369 x	2.165 x
20 $\bar{2}$ 1	1.350 x	2.126 x
0004	1.287 x	2.070 x
20 $\bar{2}$ 2	1.2295 x	1.942 x
10 $\bar{1}$ 4	1.1691 x	1.873 x
20 $\bar{2}$ 3	1.084 x	1.720
21 $\bar{3}$ 0	1.058 x	1.662 x
21 $\bar{3}$ 1	1.036 x	1.630
11 $\bar{2}$ 4	1.007 x	1.604
21 $\bar{3}$ 2	0.978 x	1.543 x
10 $\bar{1}$ 5	0.966 x	1.550
20 $\bar{2}$ 4	0.947 x	1.507 x
30 $\bar{3}$ 0	0.933 x	1.466 x
21 $\bar{3}$ 3	0.900 x	1.424 x
30 $\bar{3}$ 2	0.877 x	1.382 x
0006	0.858 x	1.380
20 $\bar{2}$ 5	0.829 x	1.323 x
10 $\bar{1}$ 6	0.820 x	1.317
21 $\bar{3}$ 4		1.296 x
22 $\bar{4}$ 0		1.270 x
11 $\bar{2}$ 6		1.212 x

x: observed in X-Ray diffraction * & **

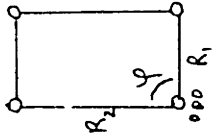
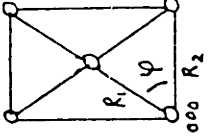
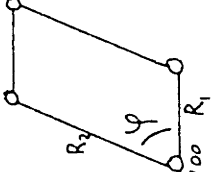
*: ASTM X-Ray card # 5-0665

** : ASTM X-Ray card # 6-0613

$$o: \frac{1}{d^2} = \frac{4}{3a^2} (h^2 + hk + k^2) + \frac{1}{c^2} l^2$$

Table C2 : Twelve of the most densely populated reciprocal lattice planes for ZrCr₂.

a=5.079Å c=8.279Å c/a= 1.630

3 indices pole	4 indices pole	Type	R ₂ /R ₁	φ°	$h_1 k_1 l_1$ d ₁ Å	$h_2 k_2 l_2$ d ₂ Å	ρ [*] Å ⁻²
010	1210		1.882	90°	0001° 8.279	1010 4.399	36.4
012	1216		1.812	90°	1010 4.399	1211° 2.428	10.68
120	0110		1.630	90°	0002 4.140	2110 2.540	10.51
122	0112		1.530	90°	0111 3.884	2110 2.540	9.86
001	0001		1.000	60°	1100 4.399	1010 4.399	22.34
011	1213		1.132	64°	1010 4.399	0111 3.884	19.04
021	2223		1.459	70°	1010 4.399	0112 3.014	14.11
031	1211		1.882	75°	1010 4.399	0113 2.338	10.67
121	0111		1.000	80°	1101 3.884	1011 3.884	15.31
131	1543		1.289	88°	1011 3.884	1102 3.014	11.72
141	2753		1.662	81°	1011 3.884	1103 2.338	9.20
013	1219		2.699	79°	1010 4.399	1321 1.630	7.30

•: occurs by double diffraction

*: $\rho = \frac{1}{\sin^2 \phi} \sum_{h_1 k_1 l_1} \sum_{h_2 k_2 l_2} |F_{h_1 k_1 l_1}|^2 |F_{h_2 k_2 l_2}|^2$

Table C3 : Calculated^o interplanar spacing of the (hkl) planes for tetragonal Zr₂Ni (a=6.499Å c=5.270Å *).

hkl	d _{hkl} Å	hkl	d _{hkl} Å
100	6.499	410	1.576
001	5.270	401	1.553
110	4.595	023	1.545
101	4.093	330	1.532 +
111	3.464	411	1.510 +
200	3.250	123	1.503 +
210	2.906	322	1.488
201	2.766	331	1.471
002	2.635 +	420	1.453 +
211	2.545 +	223	1.396
102	2.442	402	1.383 +
220	2.298 +	033	1.364
112	2.286 +	332	1.324 +
300	2.166	004	1.318
221	2.106	104	1.291
310	2.055 +	114	1.266
202	2.047 +	521	1.176 +
301	2.004	413	1.173 +
212	1.952		
311	1.915		
320	1.802		
003	1.757		
222	1.732		
321	1.705		
013	1.696		
302	1.673		
113	1.641		
400	1.625		
312	1.621		

observed in X-Ray diffraction.*

$$o: \frac{1}{d^2} = \frac{1}{a^2} (h^2 + k^2) + \frac{1}{c^2} l^2$$

*: A.S.T.M. X-Ray card #19-857.

hkl	d_{hkl} Å	hkl	d_{hkl} Å
111	4.163	100	11.01
200	3.605	110	7.785
220	2.549	200	5.505
311	2.174	001	5.450
222	2.081	210	4.924
400	1.803	101	4.884
331	1.654	111	4.465
420	1.612	220	3.893
422	1.472	201	3.873
511 - 333	1.388	300	3.670

Table C5 : $ZrCr_2$ Table C4 : Zr_3Si

Calculated° interplanar spacing of the (hkl) planes for cubic $ZrCr_2$ ($a_0=c_0=7.21\text{Å}$ *) and for tetragonal Zr_3Si ($a_0=11.01\text{Å}$ $c_0=5.45\text{Å}$ (29))

$$^\circ: 1/d^2 = 1/a^2 (h^2+k^2) + 1/c^2 l^2$$

*: A.S.T.M. X-Ray card # 6-0612.

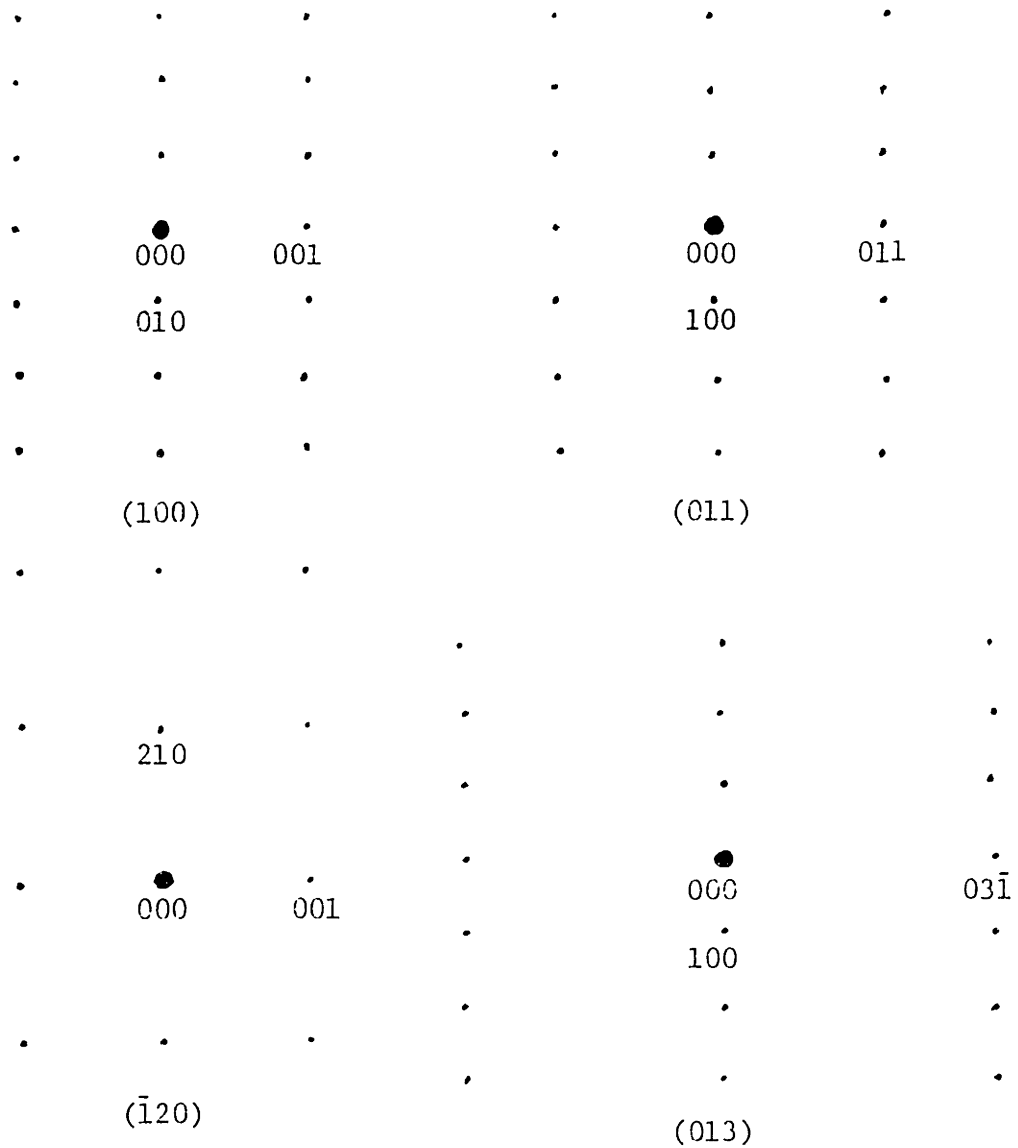


Figure C1 : Some observed electron diffraction patterns corresponding to tetragonal Zr_3Si .

APPENDIX DX-RAY DATA OBTAINED IN THE STEM

The computed characteristic indices described in Part III.2c. of this thesis are recorded in the following tables.

The abbreviations used in the "description" column of the tables are:

- p: particle
- px: particle of type x. x being 1, 2, 3, 4, 5, 6 or 7 as described in Figure 16.
- m: matrix
- u: inclusion
- R: extraction replica
- GB: grain boundary
- CW: cold worked, stress relieved material.

Each letter of the "spectrum number" corresponds to a different STEM session. For example, B4 is the fourth particle analyzed during the second STEM session.

Table D1 : Computed data for X-Ray analysis. (I)

spectrum *	time s	BGN cps/hea	Cr	Fe	Ni	Fe/BGN	L/K	Zr	Sn/BGN	description
A1	120	5.75	2	59	39	6.76	0.77	74	1.83	p 1
A2	120	8.88	2	60	39	3.22	0.90	69	1.29	p 1
A3	60	20.19	53	47	0.3	14.7	1.28	43	1.12	p
A4	60	6.20	54	47	-0.4	11.82	0.85	51	1.12	p 4
A5	80	2.65	55	46	-0.4	5.53	0.45	73	0.98	p
A6	90	2.69	1	56	43	4.29	0.62	83	1.03	p 2
A7	94	6.73	34	99	-33	1.17	1.07	99	1.22	m
A8	120	9.00	40	88	-28	1.23	1.07	99	1.25	m
A9	120	6.10	47	187	-134	1.18	0.97	100	1.14	m
A10	120	5.93	68	49	-17	1.08	0.99	99	1.09	m
A11	80	3.76	53	47	0.3	15.45	0.74	44	1.13	p.
B1	30	8.02	-1	48	52	3.04	0.07	91	1.00	p 7
B2	30	11.9	44	56	0.4	13.04	0.16	62	1.00	p 4
B3	30	13.12	1	53	46	7.36	0.14	80	1.03	p 7
B4	30	15.60	-1	56	46	5.02	0.13	85	1.11	p 7
B5	30	23.64	13	80	7	1.37	0.50	99	1.31	G.B.
B6	30	38.70	0.1	61	38	7.01	0.92	72	1.13	p 2
B7	30	34.69	28	89	-17	1.29	1.03	99	1.32	m
B8	30	39.27	36	84	-20	1.27	0.97	99	1.35	m
B9	30	47.77	1	60	40	6.03	0.75	77	1.25	p 1
B10	30	45.69	0.4	58	40	7.02	0.72	76	1.33	p 1
B11	15	43.20	0.3	59	38	5.39	0.56	84	1.38	p 2
B12	15	45.74	48	51	1	7.71	0.87	69	1.38	p 7
B13	15	44.47	14	57	30	5.75	0.87	78	1.34	p 7
B14	15	43.74	47	52	1	9.08	0.89	64	1.48	p 7

Table D1 : cont'd (II)

spectrum #	time s	BGN cts/sec	Cr	Fe	Ni	Fe/BGN	L/K	Zr	Sn/BGN	description
B15	15	37.44	14	56	30	5.97	0.89	78	1.30	p7
B16	15	40.00	4	58	38	4.78	0.89	83	1.44	P
B17	15	38.50	4	58	38	6.68	0.87	76	1.39	P
B18	15	17.24	2	59	39	8.88	0.80	68	1.21	p3
B19	15	13.20	5	61	34	3.76	0.68	88	1.35	p2
B20	15	22.84	55	45	2	8.88	1.29	59	1.17	p5
B21	50	7.73	4	59	37	8.85	0.93	71	1.03	p2
B22	20	19.12	48	144	-92	1.25	1.33	99	1.29	m (area)
B23	20	19.93	46	53	0.1	4.62	0.70	83	1.16	P
B24	20	19.30	5	59	36	2.89	0.66	92	1.29	P
B25	20	22.68	3	58	39	5.57	0.68	82	1.22	P (same as B24)
B26	20	23.50	47	53	0.4	12.08	0.66	59	1.20	P
B27	20	17.70	2	55	43	5.79	0.43	80	1.09	P
B28	20	20.83	1	57	42	9.12	0.43	72	1.25	P (small)
B29	20	33.83	29	58	12	1.39	0.99	98	1.23	m
C1	100	10.44	28	98	-25	1.28	1.00	99	1.00	u
C2	50	7.36	2	56	42	4.02	0.54	86	0.96	p2
C3	50	8.66	2	58	40	6.36	0.77	77	0.96	P
C4	50	7.06	55	44	0.2	11.01	0.55	58	0.91	p5
C5	50	5.45	3	55	42	4.63	0.53	85	0.92	P
C6	50	6.39	3	57	39	5.49	0.60	81	0.96	P (edge)
C7	50	4.28	44	60	-0.3	1.35	0.47	98	1.25	m
C8	50	3.84	7	73	19	1.36	0.20	99	1.11	hole count
C9	50	8.1	53	46	1	10.87	0.51	59	0.87	p2
C10	50	35.54	53	70	-23	1.25	1.13	99	1.40	m

Table D1 : cont'd (III)

spectrum #	time s	BGN cts/sec	Cr	Fe	Ni	Fe/BGN	L/K	Zr	Sn/BGN	description
C11	50	15.07	69	81	-50	1.17	1.15	99	1.27	M
C12	50	7.23	2	57	41	6.62	0.73	77	0.98	P2
C13	50	7.96	31	78	-9	1.30	0.91	99	1.26	
C14	50	8.11	1	61	39	8.18	0.92	71	1.00	P2
C15	50	4.97	57	43	-0.2	10.89	0.52	56	0.96	P4
C16	50	6.56	55	45	-0.2	13.95	0.74	46	0.93	P
C17	50	4.88	2	58	40	6.22	0.76	78	0.95	P1
C18	50	9.02	56	44	-0.2	12.60	0.65	51	0.89	P5
C19	50	8.20	2	57	41	6.23	0.78	78	1.01	P
C20	50	7.78	3	56	41	2.40	0.80	93	1.16	P (etched)
C21	50	6.06	56	43	1	8.88	0.45	63	1.00	P4.
C22	50	5.48	56	44	-0.3	11.46	0.51	58	0.97	P
C23	50	7.93	1	59	40	6.69	0.83	75	0.97	P1 on G.B.
C24	500	8.71	41	82	-22	1.27	0.97	99	1.04	(same as C1)
D1	60	8.43	52	48	1	17.88	0.86	42	1.13	P4
D2	60	7.89	1	60	39	8.93	0.92	69	1.01	P7
D3	60	8.49	52	47	1	17.47	0.79	42	1.08	P7
D4	60	12.78	45	76	-21	1.21	1.11	99	1.26	U
D5	60	13.09	73	56	-29	1.13	1.03	99	1.26	U
D6	60	10.31	2	60	38	4.02	0.84	87	1.41	P1
D7	60	2.59	55	45	0.1	7.21	0.37	75	1.21	P5
D8	60	4.95	55	45	-0.2	16.04	0.70	47	1.07	P5
D9	60	4.33	54	46	-0.4	5.67	0.79	77	1.17	P
D10	60	4.16	53	46	1	6.80	0.80	73	1.13	P
D11	60	5.81	52	48	0.3	17.38	0.78	43	1.11	P7

Table D1 : cont'd (IV)

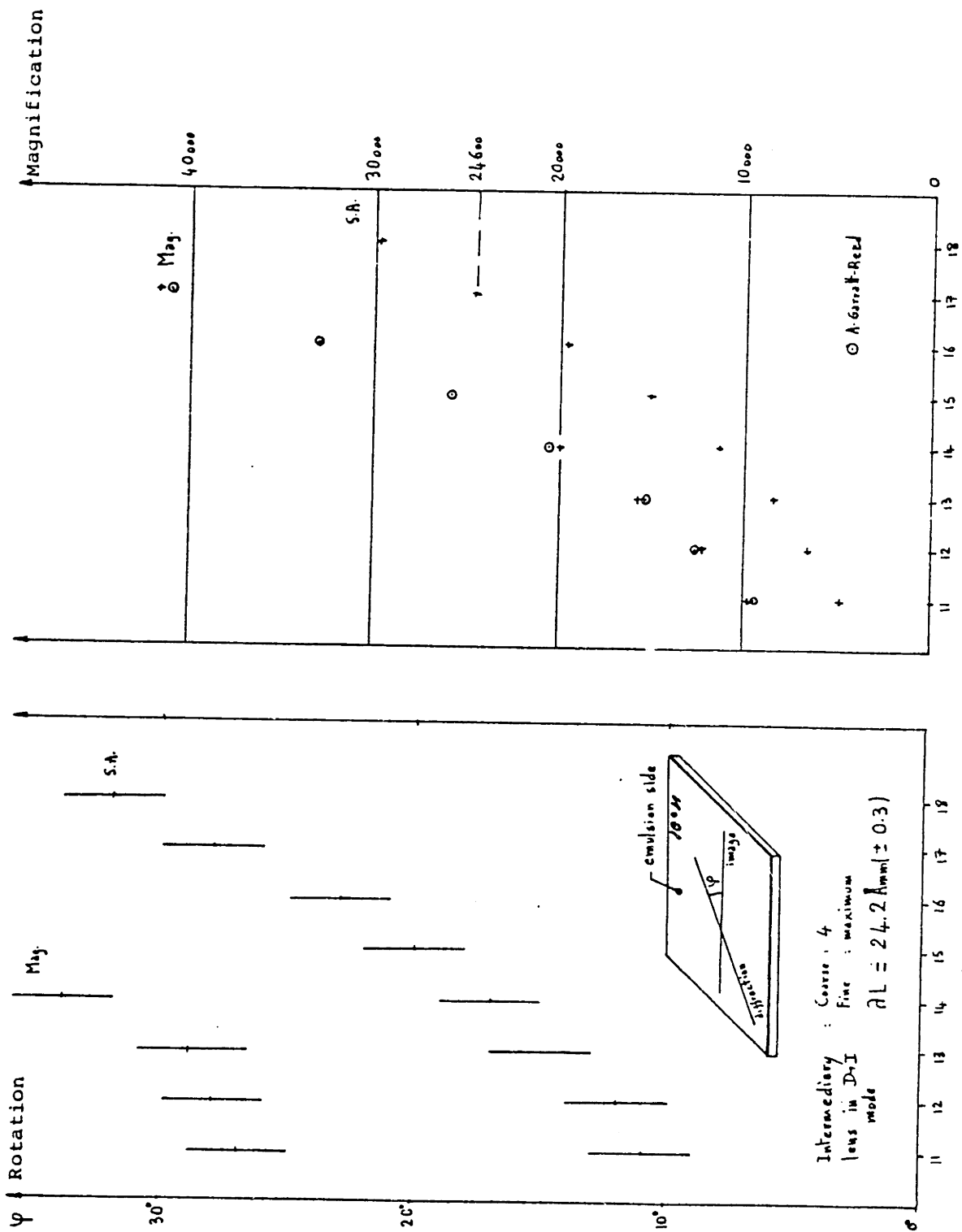
spectrum #	time s	BGN cts/sec	Cr	Fe	Ni	Fe/BGN	L/K	Zr	Sn/BGN	description
D12	60	5.45	3	58	39	9.94	0.87	69	1.07	P7
D13	60	4.07	52	47	1	18.19	0.65	46	1.07	P7
D14	60	4.70	1	58	40	7.65	0.82	76	1.06	P1 on G.B.
D15	60	14.24	75	40	-16	1.05	1.83	100	1.46	M
E1	60	3.61	55	45	1	10.73	0.83	60	1.01	P7
E2	60	2.70	2	57	41	6.13	0.64	81	0.85	P7
E3	60	4.46	35	70	-5	1.10	1.06	100	1.37	M
F1	60	6.71	55	45	0.2	24.12	2.00	20	0.91	R
F2	60	7.48	54	46	1	24.08	1.89	20	1.03	R
F3	30	13.22	56	43	0.2	21.37	1.82	21	0.90	R
F4	20	23.98	58	44	0.4	23.03	1.76	20	1.05	R
F5	20	8.63	54	45	0.2	20.60	1.97	21	0.95	R
F6	20	8.03	55	44	1	25.12	1.71	21	1.11	R
F7	20	11.50	54	45	1	25.65	1.86	20	0.97	R
F8	20	9.23	54	45	0.4	26.56	1.88	20	1.12	R
F9	20	10.90	55	44	1	23.90	1.87	21	1.01	R
F10	20	4.40	56	44	0.2	21.15	1.82	20	0.90	R
F11	20	4.03	54	45	0.5	26.75	1.87	20	0.99	R
F12	20	7.48	55	44	0.2	25.83	1.87	20	1.02	R
G1	50	31.80	53	47	-0.4	23.83	1.16	25	1.15	P6
G2	50	2.56	2	56	42	13.04	1.83	54	1.00	P3
G3	50	4.12	55	45	-0.1	24.10	1.86	22	0.91	P
G4	50	0.68	57	42	1	30.68	1.90	23	0.87	P5
G5	50	5.02	2	59	39	12.13	1.43	57	1.25	P7
G6	50	5.75	54	46	0.3	13.21	1.71	45	1.21	P7

Table D1 : cont'd (Σ)

spectrum #	time s	BGN	Cr	Fe	Ni	Fe/BGN	L/W	Zr	Sn/BGN	description
G7	50	174	57	44	-0.2	25.06	1.63	23	0.75	P7
G8	50	446	55	44	0.4	27.36	1.63	23	1.02	P7
G9	50	4.42	2	59	38	10.57	1.70	59	1.05	P7
G10	50	3.41	56	44	0.3	24.98	1.69	23	1.00	P7
G11	50	5.97	2	58	39	12.21	1.55	57	0.98	P2
G12	50	4.46	2	58	40	12.82	1.91	53	1.05	P
G13	50	4.46	2	58	40	11.54	1.48	56	1.07	P7
G14	50	3.06	54	45	0.2	25.97	1.48	24	1.25	P7
G15	20	8.83	56	44	-0.1	9.63	1.41	56	1.33	P7
G16	20	3.28	57	44	-0.1	23.18	1.69	24	0.95	P7
G17	20	3.45	54	46	-0.2	20.87	1.78	29	0.89	P
G18	20	6.15	54	46	-0.3	11.01	1.40	51	1.53	P7
G19	20	6.50	56	44	-0.2	10.84	1.38	51	1.51	P
G20	50	3.55	3	52	46	11.06	1.80	53	0.94	CW p3
G21	25	7.59	2	53	45	11.53	1.35	55	1.10	CW p3
G22	50	4.14	57	43	0.2	22.90	1.77	25	1.12	CW P
G23	25	5.66	61	39	0.2	19.46	1.79	27	1.25	CW P
G24	25	8.10	55	44	1	20.13	1.71	27	1.09	CW P
G25	25	6.78	52	46	2	22.54	1.75	27	1.03	CW P
G26	25	3.46	60	40	-0.2	8.00	1.77	56	1.06	CW P
G27	25	3.26	58	42	-0.2	6.99	1.84	63	1.19	CW P
G28	50	4.01	45	36	19	1.12	1.26	99	1.38	CW m
G29	25	42.18	47	47	6	1.27	1.03	98	1.51	CW m (thicker)
G30	25	25.56	31	50	19	1.33	1.09	98	1.20	CW u
G31	25	16.18	53	48	-1	1.22	1.71	98	1.07	CW u

APPENDIX ECHARACTERISTICS OF THE TEM PHILIPS EM300

The camera constant was determined with a gold sputtered film and with MoO_3 single crystals. The rotation between image and electron diffraction pattern was measured using the edge of MoO_3 single crystals. Pictures of the same area of a specimen at different knob settings were used to measure the magnification. The determination of the magnification by A. Garratt-Reed was supposed correct at the 15 Mag. knobs setting. These characteristics of the microscope are given Figure E1.



Magnification knob setting (intermediary lens in Mag. & S.A. mode)
 Figure E1 : Characteristic parameters of the TEM Philips EM300

REFERENCES

1. J.H. Schemel, A.S.T.M. Manual on Zirconium and Hafnium, ASTM-STP 639 (1977) 20.
2. M. Armand, D. Charquet, R. Syre and R. Tricot, aciers spéciaux, monographies techniques 50 (1978).
3. S. Kass, Corrosion of Zirconium alloys, ASTM Special Technical Publication No. 368, Chambre syndicale des producteurs d'aciers (1963).
4. D.L. Douglass, The metallurgy of zirconium, International Atomic Energy Agency, Vienna (1971) 155.
5. O. Kubaschewski von Goldbeck, Zirconium: physico-chemical properties of its compounds and alloys, International Atomic Energy Agency, Vienna (1976) 67.
6. M. Armand, Zirconium alloys and their transformation, 9e colloque de métallurgie, Commissariat à l'énergie atomique, Presses Universitaires de France (1966).
7. M. Hansen, K. Anderko (1958), Constitution of binary alloys, McGraw Hill.
8. R.P. Elliott (1965), Constitution of binary alloys, 1st supplement, McGraw Hill.
9. F. Shunk (1969), Constitution of binary alloys, 2nd supplement, McGraw Hill.
10. ASTM Power Diffraction File #5-0665.
11. K. Schubert, et al., Naturwissenschaften 47 (1960) 512.
12. W.E. Sweeney, A.P. Batt, J. Nucl. Mater. 13 (1964) 87.

13. O.S. Ivanov, V.K. Grigorovich, Int. Conf. peaceful uses atom. Energy (Proc. Conf. Geneva, 1958) 5, UN, Geneva (1958), 34.
14. L.E. Tanner, D.W. Levinson, Trans. Am. Soc. Metals 52 (1959) 1115.
15. J.B. Vander Sande and A.L. Bement, J. Nucl. Mat., 52 (1974) 117.
16. D.O. Northwood and R.W. Gilbert, J. Australian Inst. Metals, 18 (1973) 158.
17. A.J. Bedford and D.R. Miller, J. Aust. Int. Metals, 17 (1972) 120.
18. P. Rao, J.L. Walker and E.F. Koch, General Electric TIS Report 76-CRD-183 (1977).
19. J.E. Bailey, Acta Met., 11 (1963) 267.
20. G. Östberg, Jerukontorets Am. 145 (1961) 119.
21. G. Östberg, R. Attermo, J. Nucl. Mat. 5 (1962) 120.
22. G. Östberg, J. Nucl. Mat. 7 (1962) 103.
23. E. Vitikainen, P. Nenonen, Nucl. Materials 78 (1968) 362.
24. W. Rostoker, J. Metals (February 1953) 304.
25. W.B. Pearson, A handbook of lattice spacings and structures of metals and alloys (Pergamon Press, London 1958).
26. R.A. Versaci and M. Ipohorski, J. Nuclear Mat. 80 (1979) 180.
27. D.G. Westlake, J. Nucl. Mat. 26 (1968) 208.
28. J. DeBuigne, J.P. Guerlet, P. Lehr, Zirconium alloys and their transformation, 9e colloque de metallurgie, Commissariat at l'energie atomique, Presses Universitaires de France (1966).
29. K. Schubert, Naturwissenschaften 51 (1964) 506.
30. D. Armand, Private communication (August 1980).
31. J.M. Grange, D. Charquet, L. Moulin, 5th International conference on zirconium in the nuclear industry sponsored by ASTM and ANS, Boston, Mass, 4-7 August, 1980.

32. P.G. Partridge, Metallurgical Reviews, Review 118 (1967).
33. B.D. Cullity, Elements of X-Ray diffraction, 2nd edition, Addison Wesley Publ. Comp. (1978), 63.
34. P.B. Hirsh, A. Howie, R.B. Nicholson, D.W. Pashley and M.J. Whelan, Electron microscopy of thin crystals (Plenum Press, New York, 1965).
35. G. Thomas and M.J. Goringe, Transmission electron microscopy of materials (John Wiley and Sons, 1979) 112.
36. M.H. Loretto, R.E. Smallman, Defect analysis in electron microscopy (John Wiley and Sons, New York, 1975).